A Study of Low Frequency Vibration Isolation System for Large Scale Gravitational Wave Detectors

Department of Physics, Graduate School of Science
University of Tokyo

Takanori Sekiguchi

January 2016

Abstract

Gravitational waves are distortions of spacetime which propagate through space at the speed of light. Several large-scale interferometric gravitational wave detectors have been constructed for their direct detection. So-called first generation detectors (TAMA, GEO, LIGO, Virgo) have performed scientific observations. However, they had a detection probability of only a few percent per year at best and gravitational waves have not been detected by them yet. More sensitive detectors which are capable of detecting many events per year are necessary. Based on the experience gathered with the first generation detectors, second generation detectors have been designed with thousands of times higher probability of gravitational wave detection. The Japanese second generation detector, KAGRA was funded recently and is now being constructed.

Seismic motion is an inevitable noise source for ground-based interferometric gravitational wave detectors. The continuous and random motion of the ground can excite the motions of the optical components of an interferometer, resulting in a displacement noise (*seismic noise*). In order to reduce the noise, vibration isolation systems are installed to isolate the optics in the interferometer from ground. The vibration isolation systems for LCGT will be based on the Seismic Attenuation System (SAS), which has been developed for TAMA and advanced LIGO. The objective of the system is to achieve seismic attenuation starting from sufficiently low frequencies ($\lesssim 0.1 Hz$) and to reduce the Root Mean Square (RMS) displacement and velocity of the optics below the level of ~ 0.1 μm and 0.1 μm/s, for stable operation and fast lock acquisition of the interferometer.

Table of Contents

Introduction

Chapter 1

This chapter describes theoretical background on gravitational wave detection and motivation of detecting low frequency gravitational waves. Section 1.1 gives theoretical explanation on gravitational waves and section 1.2 introduces possible astrophysical sources of them. Section 1.3 explains the detection schemes using interferometers and possible upgrades for improving the detection sensitivities. Section 1.4 introduce gravitational wave detector projects with large-scale terrestrial interferometers, which have been constructed or are currently proposed around the world. The section also explain contribution of seismic noise to the detector sensitivities and its impact. Section 1.5 describes motivation of expanding the sensitivities of large-scale interferometric detectors toward a low frequency region.

1.1 Gravitational waves in general relativity

1.1.1 Formulation of gravitational waves

Existence of the gravitational waves was predicted by A. Einstein in 1916 along his theory of general relativity [1]. The theory of general relativity describes gravity as consequence of the curvature of spacetime caused by the presence of mass, whereas gravity was assumed to be force involved between any two objects with mass in Newton's theory. The curvature of spacetime is expressed mathematically by the metric tensor $g_{\mu\nu}$, which derives the spacetime interval ds between two neighboring points with the following equation:

$$ds^2 = g_{\mu\nu} dx^\mu dx^\nu. \tag{1.1}$$

The symbol with a Greek index dx^μ ($\mu = 0, 1, 2, 3$) describe differential spacetime coordinates of the two neighboring points. A flat spacetime without any gravity is described with the Minkovskii metric tensor noted as $\eta_{\mu\nu}$. Relationship between the spacetime and mass or energy distribution is represented by a formula called the Einstein's equations:

$$G_{\mu\nu} = \frac{8\pi G}{c^4} T_{\mu\nu}. \tag{1.2}$$

Here $G_{\mu\nu}$ is called the Einstein's tensor and is a function of the mertic tensor $g_{\mu\nu}$. $T_{\mu\nu}$ is called the stress-energy tensor, describing the energy density distribution in the field. G and c are the gravitational constnant and the speed of light in vacuum, respectively.

A basic concept of gravitatinal waves is derived by a week-field approximation of the above-mentioned formulization. In the weak-field limit, the metric tensor of the spacetime can be described as small perturbation from the Minkovskii tensor:

$$g_{\mu\nu} = \eta_{\mu\nu} + h_{\mu\nu}, \quad \text{where} \quad |h_{\mu\nu}| \ll 1. \tag{1.3}$$

Considering a vacuum condition with $T_{\mu\nu} = 0$, a linear approximation of the Einstein's equation and an adept coordinate transform can derive the following wave equations of the spacetime perturbation [2]:

$$\left(\nabla^2 - \frac{1}{c^2} \frac{d^2}{dt^2} \right) h_{\mu\nu} = 0. \tag{1.4}$$

This equation indicates that small distortions of spacetime can propagate at the speed of light c in a field with no energy distribution. These distortions are called gravitational waves.

1.1.2 Measurable effect of gravitational waves

When one chooses a spatial coordinate such that a gravitational wave travels in the z direction, the plane wave solution of the equations (1.4) can be written in the following expression [2]:

$$h_{\mu\nu}(z,t) = \begin{pmatrix} 0 & 0 & 0 & 0 \\ 0 & -a_+ & a_\times & 0 \\ 0 & a_\times & a_+ & 0 \\ 0 & 0 & 0 & 0 \end{pmatrix} \exp\left[i\omega \left(t - \frac{z}{c} \right) \right]. \tag{1.5}$$

Here ω is the wave frequency, and a_+ and $a_\times$ represent the amplitudes of two independent wave polarizations. Measurable effects of the gravitational wave can be described with assuming test particles placed at spacially separated locations in the xy plane. When a particle is placed at the origine of a coordinate system and another is placed at $x^i = (L\cos\theta, L\sin\theta, 0)$, the proper distance between the two particles L' is altered by the gravitational wave and expressed as

$$L' \equiv \int \sqrt{ds^2} \approx L \left(1 + \frac{1}{2} a_+ e^{i\omega t} \cos 2\theta + \frac{1}{2} a_\times e^{i\omega t} \sin 2\theta \right). \tag{1.6}$$

Figure 1.1 shows an illustration of the tidal effects of the two polarization of the gravitational wave to circularly arranged particles. A passing gravitational wave stretches spacetime in one direction while compressing it by an equal amount in the perpendicular direction. The two polarizations of the gravitational wave are identical but 45 deg apart. They are conveniently called the plus (+) mode and the cross (×) mode of the gravitational wave. The length shift is proportional to the original distance between the particles

$$\frac{\Delta L}{L} = \frac{1}{2}h, \tag{1.7}$$

where h is the spacetime distorsion in the direction of measurement. Therefore the further the measurement targets separate, the larger measurable effect the observer obtains. This becomes a big motivation to construct as large detectors as possible for gravitational wave observatories.

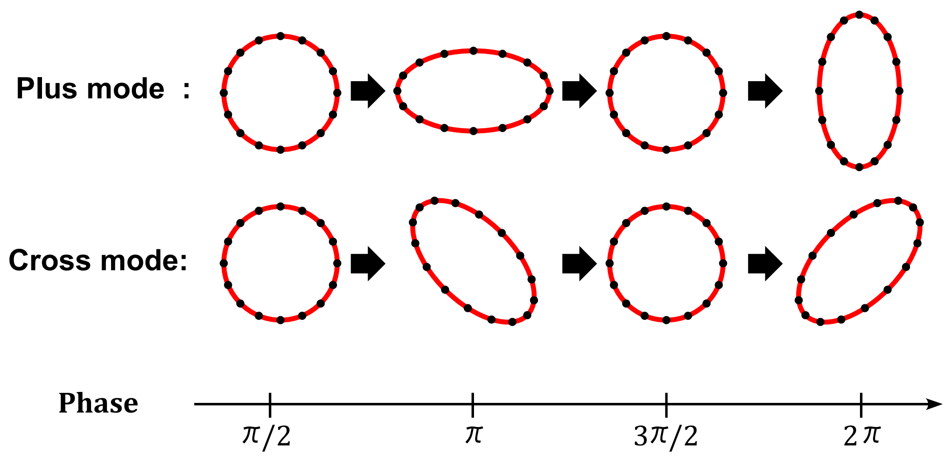

Figure 1.1: An illustration of the tidal effect of gravitational waves.

1.1.3 Gravitational wave emittion

Gravitational waves can be emitted when objects with mass move around in spacetime. However, the conservation of energy and linear momentum forbid monopole and dipole radiation of gravitational waves and thus systems having spherical or axial symmetry cannot emit gravitational waves. Quadruple radiation is the possible lowest order emission of gravitational waves. In the quadruple approximation, the amplitude of gravitational waves is calculated as [2]

$$h_{ij} = \frac{2G}{c^4 r}\ddot{Q}_{ij}. \tag{1.8}$$

Here Q_{ij} is the quadrupole moment of the mass distribution and r is the distance between the gravitational wave source and the observer. The amplitude of the gravitational wave expected from the formula (1.8) is extremely small. For example, two 100 kg masses connected with 2 m beam, rotating in 100 cycles per second will emit 200 Hz gravitational wave of amplitude only $h \sim 10^{-43}$ at a distance of 1500 km [3]. It is extremely difficult to detect such a tiny distortion of spacetime. Detectable gravitational waves only come from violent astronomical events, involving large acceleration of massive and compact objects.

1.2 Astrophysical gravitaitonal wave sources

This section breifly describes several types of possible astrophysical graivtational wave sources, and their predicted strengths and frequencies. More extensive studies of gravitational wave sources can be found in reference [4].

1.2.1 Compact binary star coalescence

A binary system formed by two compact stars such as black holes, neutron starts and white dwarfs is an extensively studied gravitational wave source. The waveforms of the inspiral graivtational waves are well predicted and therefore it is considered to provide promising gravitational wave signals.

As the orbit of binary starts progresses in time, the orbital period and radius decrease due to energy loss by gravitational wave emittion. Accordingly the amplitude and frequency of the emitted gravitational wave increase with time, which creates distinctive gravitational waveforms known as chirp signals [2]. The amplitude and frequency revolution of a chirp signal are approximately calculated as

$$f_{\rm GW}(\tau) \approx 135\ [\mathrm{Hz}] \left(\frac{M_{\rm c}}{1.2M_\odot}\right)^{5/8} \left(\frac{1\ \mathrm{sec}}{\tau}\right)^{-3/8}, \tag{1.9}$$

$$h(\tau) \approx 2.1 \times 10^{-23} \left(\frac{M_{\rm c}}{1.2M_\odot}\right)^{5/3} \left(\frac{\tau}{1\ \mathrm{sec}}\right)^{-1/4} \left(\frac{r}{200\ \mathrm{Mpc}}\right)^{-1}. \tag{1.10}$$

Here τ is the time to coalescence of the binary stars, r is the distance between the source and observer and $M_{\rm c}$ is the chirp mass defined by the masses of two stars as $M_{\rm c} = (m_1 m_2)^{3/5}(m_1 + m_2)^{-1/5}$.

When the orbital radius falls down below the Innermost Stable Circular Orbit (ISCO), stable circular orbits are no longer allowed and the binary stars eventually plunge with each other and merge. A binary system of two neutron stars for an example is expected to reach a frequency of about 800 Hz when the radius reaches ISCO. Computation of merging neustron stars or black holes is quite challenging in terms of computation costs and thus numerous efforts have been made to calculate these dynamics and associated gravitational radiation waveform with supercomputers [5]. The merger of the binary stars results in a highly deformed single black hole which rids its deformity by emitting gravitational waves providing ring down signals.

1.2.2 Spin of compact stars

A spinning compact star such as a radio pulsar becomes a possible gravitational wave source when it has asymmetry around its rotation axis. It is expected to provide a long continuous wave at a single frequency. Detection of monochromatic gravitational waves has an advantage that signal to noise ratio can be improved by integrating the signals over a long period of time. The gravitational wave amplitude from an axisymmetric spinning object is calculated by

$$h \approx 1.1 \times 10^{-25} \left(\frac{\epsilon}{10^{-6}}\right) \left(\frac{I}{10^{38}\ \text{kg m}^2}\right) \left(\frac{10\ \text{kpc}}{r}\right) \left(\frac{f_{\text{GW}}}{1\ \text{kHz}}\right)^2. \tag{1.11}$$

Here f_{GW} represents the frequency of gravitational wave and is twice of the spin frequency. I is the moment of inertia around the spin axis and ϵ is the equatorial ellipticity.

1.2.3 Supernovae

A supernova caused by gravitational collapse of a heavy star core is expected to emit gravitational waves in a large amplitude since it accelerates an enourmous amount of mass dramatically in a short term. Although prediction of the exact waveforms from supernovae is challenging, recent progress in the field of numerical relativity provides estimation on the magnitude of the emitted gravitational waves [6]. A rough estimate of the gravitational wave amplitude from a superonva occuring in the nearby galaxies is in the order of 10^{-21}-10^{-22} in spacetime strain. The explosion models suggest that the frequency of the emitted gravitational waves widely spread around 1 kHz. Therefore a supernova in nearby galaxies can be a reasonable target for terretrial interferometric graivtational wave detectors, whose target frequency is 10-10^4 Hz.

1.2.4 Stochastic background

A stochastic background of gravitational waves can be provided from numerous unresolved astrophysical sources such as white dwarf binaries, and cosmological origins such as inflation, phase transition in the early universe and cosmic strings [7]. The magnitude and the frequency of the gravitational waves with cosmological origins vary from theory to theory.

Detection of a stochastic background generally invloves cross correlation between observations of several detectors. Analyses of a stochastic background have been performed using terrestrial interferometric gravitational wave detectors and the measurements provide restriction and upper limits to several theories on cosmological gravitational wave sources [8].

1.3 Interferometric gravitational wave detection

The first attempt to detect gravitational waves was performed in 1960's by J.Weber [9]. He invented so-called resonant bar detector, which measures resonant vibrations of massive metal bars excited by passing gravitational waves. Following Weber's pioneering work, various resonant bar detectors with improved sensitivities were constructed around the world and coincident observations with a number of detectors were performed [10]. However, evident signals from passing gravitational waves were not found by resonant bar detectors.

Gravitational wave detectors mainly developed nowadays are based on laser interferometric techniques. This section describes brief introductions of the detection schemes and possible imporvement of detector sensitivities.

1.3.1 Basic detection scheme

The basic configuration of an interferometric gravitational wave detector is a Michelson interferometer composed with suspended mirrors. Its optical configuration is shown in Figure 1.2. An incoming beam from a coherent light source is split by the beam splitter into two orthogonal paths. The two beams are reflected by the end mirrors and recombined at the beam splitter. They interfere with each other, and a fraction of beam goes to the photo detector and the rest goes back to the light source. The beam intensity at the photo detector depends on the phase difference accumulated in the two optical paths and is calculated as

$$P_{\mathrm{PD}} = 2P_0(r_{\mathrm{BS}}t_{\mathrm{BS}})^2(1-\cos\delta\phi). \tag{1.12}$$

Here P_0 is the beam intensity injected from the light source and $\delta\phi$ is the phase difference between the two optical paths. t_{BS} and r_{BS} denote respectively the amplitude reflectivity and transmissivity of the beam splitter. The beam intensity on the photo detector is converted to photo current and then to readable formats to the observers.

Suppose that a gravitational wave comes from the z direction with $+$ polarization and amplitude of $h(t)$. The tidal effect of the gravitational wave changes the optical lengths of the two orthogonal arms and results in differential phase shift. The phase difference of the two optical paths caused by the gravitational wave is calculated as [11]

$$\delta\phi_{\mathrm{GW}}(t) = \frac{2\pi c}{\lambda}\int_{t-2L/c}^{t} h(t')dt', \tag{1.13}$$

where λ is the wavelength of the laser beam and L is the length of the arms ($L_x \approx L_y \approx L$). The frequency response of the Michelson interferometer to gravitational waves is derived from the Fourier transform of this equation as

$$H_{\mathrm{MI}}(\omega) \equiv \frac{\tilde{\phi}_{\mathrm{GW}}(\omega)}{\tilde{h}(\omega)} = \frac{4\pi L}{\lambda}\exp(-i\omega L/c)\frac{\sin(\omega L/c)}{\omega L/c}. \tag{1.14}$$

Figure 1.3 shows the amplitude plots of $H_{\rm MI}$ as a function of frequency with various arm lengths. When the arm length is much shorter than the wavelength of the gravitational wave ($L \ll \lambda_{\rm GW}$), the frequency response is approximated as $H_{\rm MI} \sim 4\pi L/\lambda$. It indicates that a detector with longer arms is more sensitive to gravitational waves. However, when the arm length gets longer than the wavelength of the gravitational wave ($L \gtrsim \lambda_{\rm GW}$), canceling of the gravitational wave signals occurs. $|H_{\rm MI}|$ is maximized at

$$L = \frac{\pi c}{2\omega} = \frac{\lambda_{\rm GW}}{4}. \tag{1.15}$$

For a gravitational wave of 100 Hz, the optimum arm length is about 750 km. It is unrealistic to construct such a large interferometer on the Earth and thus some techniques to expand effective arm lengths are demanded to improve the sensitivties.

1.3.2 Delay-line and Fabry-Perot cavity

One instinctive way of expanding the effective optical path lenghs is to introduce delay-lines to the interferometer arms, in which the light is multiply reflected at the different points on the mirror surface. Another way is to introduce Fabry-Perot cavities, in which the light is reflected multiple times as in the delay-lines but the optical paths are alined. A Michelson interferometer with folded arms is called a delay-line Michelson interferometer, while the detector is called a Fabry-Perot Michelson interferometer when Fabry-Perot cavities are used. The optical configurations of the two types are shown in figure 1.4.

A delay-line expands the effective arm length by a factor of $N/2$ when the beam is reflected on the mirror surfaces by $N-1$ times. The expression for the frequency response of

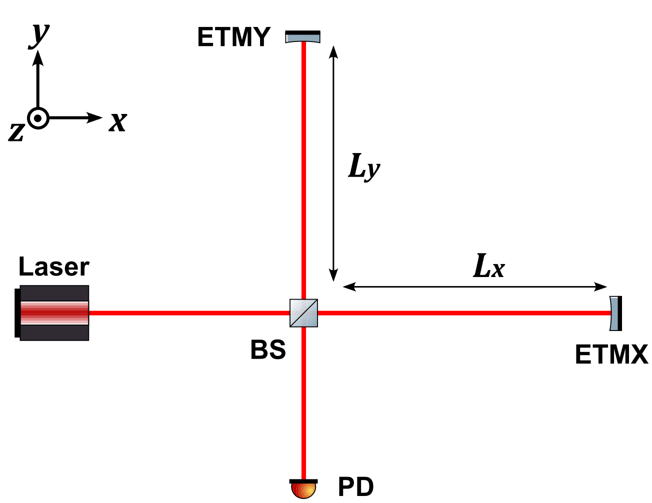

Figure 1.2: Optical configuration of a Michelson interferometer (BS: beam splitter, PD: photo detector, ETMX(Y): end test masses).

a delay-line-Michelson interferometer to gravitational waves is simply obtained by replacing L of $H_{\mathrm{MI}}(\omega)$ in formula (1.6) by $NL/2$:

$$H_{\mathrm{DLMI}}(\omega) = \frac{2\pi NL}{\lambda} \exp(-i\omega NL/2c) \frac{\sin(\omega NL/2c)}{\omega NL/2c}. \tag{1.16}$$

On the other hand, a Fabry-Perot cavity extends the effective arm length by multiple interference of the incident beam. A Fabry-Perot cavity is composed of two mirrors and one of them is partially reflective. The light entered into the cavity is reflected back and forth many times between the mirrors. A fraction of the stored light inside the cavity is leaked out and goes back to the incident direction. The frequency response of a Fabry-Perot-Michelson interferometer to gravitational waves $H_{\mathrm{FPMI}}(\omega)$ is written as

$$H_{\mathrm{FPMI}}(\omega) = \frac{4\pi\alpha_{\mathrm{cav}}L}{\lambda} \frac{\exp(-i\omega L/c)}{1 - r_{\mathrm{F}} r_{\mathrm{E}} \exp(-2i\omega L/c)} \frac{\sin(\omega L/c)}{\omega L/c}, \tag{1.17}$$

when two Fabry-Perot cavities are in resonance [11]. α_{cav} is calculated as

$$\alpha_{\mathrm{cav}} = \frac{t_{\mathrm{F}}^2 r_{\mathrm{E}}}{1 - r_{\mathrm{F}} r_{\mathrm{E}}}, \tag{1.18}$$

where r_{F} and $r_{\mathrm{E}} \sim 1$ are the amplitude reflectivity of the front and end mirrors, and t_{F} is the transmissivity of the front mirror. L is the length of the Fabry-Perot cavity. The average bounce number in a Fabry-Perot cavity is written as

$$N_{\mathrm{FP}} = \frac{2\sqrt{r_{\mathrm{F}} r_{\mathrm{E}}}}{1 - r_{\mathrm{F}} r_{\mathrm{E}}} = \frac{2\mathcal{F}}{\pi}. \tag{1.19}$$

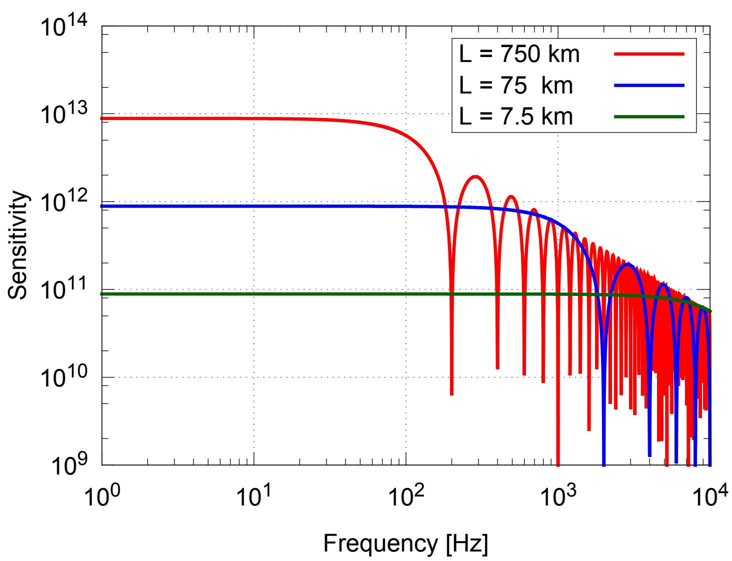

Figure 1.3: Frequency response of the Michelson interfoerometer to gravitational wave with various arm lengths.

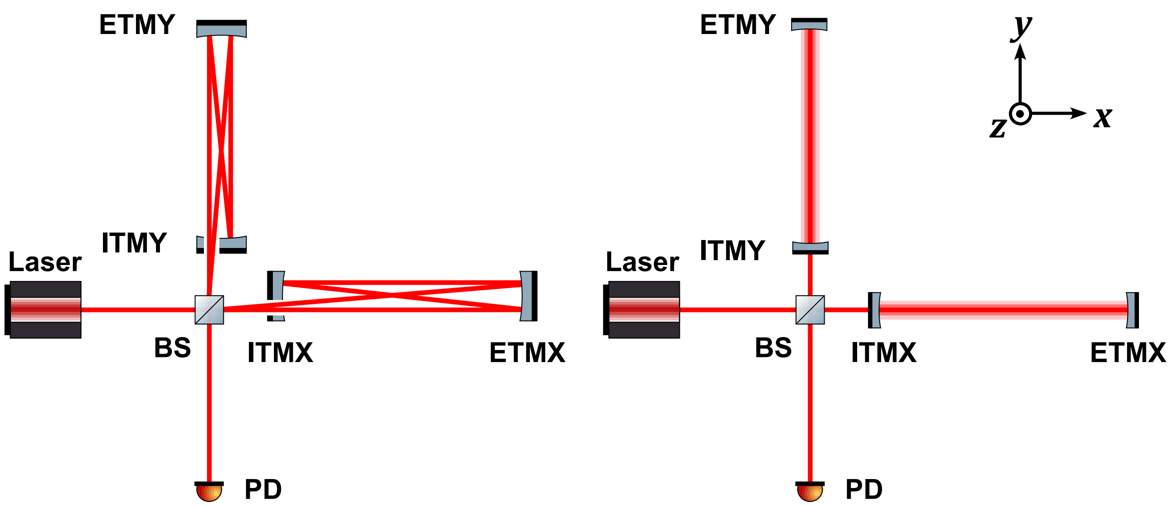

Figure 1.4: Optical configurations of a delay-line Michelson interferometer (left) and a Fabry-Perot Michelson interferometer (right). ITMX and ITMY (input test masses) are introduced to achieve multiple reflections.

$\mathcal{F}$ is called a finesse, which represents the sharpness of the resonance of the Fabry-Perot cavity.

Figure 1.5 shows comparison of frequency responses of different types of interferometers. The arm lengths are set 3 km in all the cases and the frequency responses of the delay-line Michelson and Fabry-Perot Michelson interferometers are optimized for a gravitational wave with a frequency of 100 Hz. The Fabry-Perot Michelson interferometer shows a smoother frequency response than that of the delay-line Michelson interferometer, which becomes a big advantage in detecting wide-band gravitational waves. In addition to the differeces in the frequency response, implementation of delay-lines with large number of reflection has several practical problems in terms of largeness of mirror size and thermal noise issues. Therefore large-scale interferometric gravitational wave detectors developed nowadays adopt Fabry-Perot cavities, or delay-lines but with small number of reflection.

1.3.3 Recycling cavities

Besides the devices for arm lengths expansion, recent interferometric gravitational wave detectors employ so-called recycling cavities to further improve the sensitivity and optimize the observational bandwith. The scheme introduces additional partial-reflection mirrors just behind or after the Michelson interferometer to compose optical cavities with interference. The mirror placed behind and after the Michelson part is called the power recycling mirror and the signal recycling mirror respectively. Figure 1.6 shows optical configuration of a Michelson interferometer with the two recycling mirrors introduced (so-called the dual-recycling interferometer). A brief introduction about the recycling schemes is

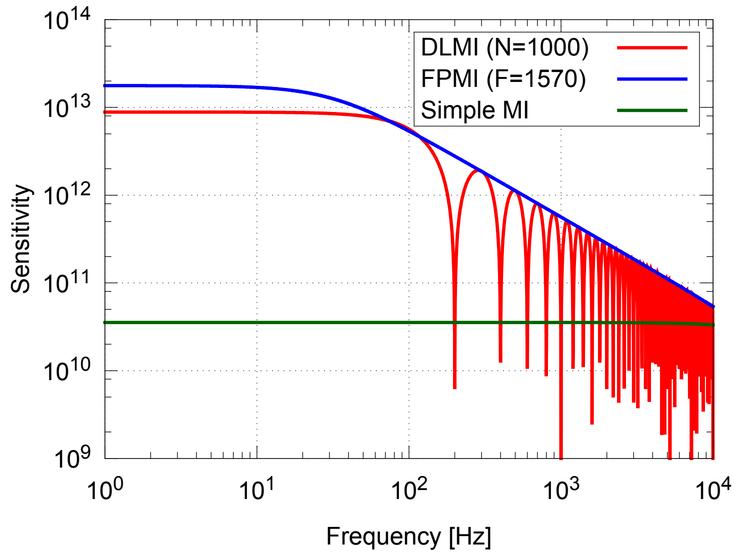

Figure 1.5: The frequency response of the delay-line Michelson, Fabry-Perot Michelson and simple Michelson interferometer with 3 km arm length. The frequency responses of the delay-line-Michelson and Fabry-Perot-Michelson interferometers are optimized for a gravitational wave of 100 Hz.

described here. Detailed studies of the detection scheme and resulting sensitivities can be found in references [12, 13].

Power Recycling

The power recycling mirror reflects the light coming back from the Michelson interferometer and recycle the laser power which would be otherwise discarded [14]. The primary intention of the power recycling is to increase the amount of the laser power illuminating the beam splitter and to reduce the shot noise (see the next subsection) at the detection port monitoring gravitational wave signals. The power recycling scheme has been adopted to the first-generation large-scale terrestrial interfeormeters.

Signal Recycling

The signal recycling mirror reflect the signal fields induced by gravitational waves and leads them back to the interferometer. It increases or decreases the effective finesse for gravitational wave signals, depending on the interference condition of the optical cavity composed with the signal recycling mirror. The increase of effective finesse results in higher sensitivities to gravitational waves at low frequencies, while leading to a narrower observation bandwith [15]. The decrease of effective finesse results in the opposite effects and the scheme is called the resonant sideband extraction [16].

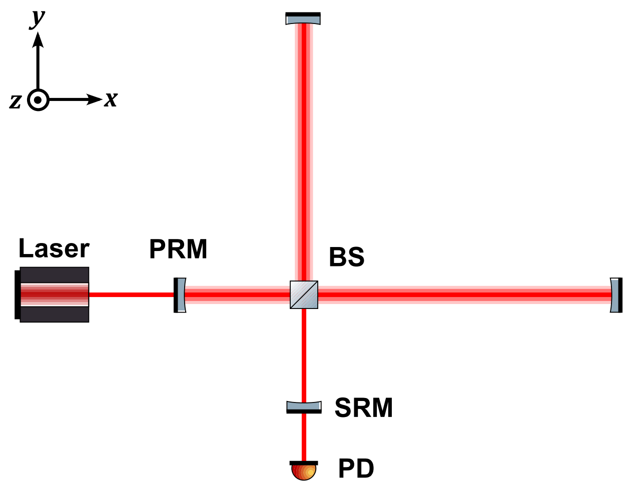

Figure 1.6: Optical configurations of a dual-recycling Michelson interferometer. PRM (power recycling mirror) and SRM (signal recycling mirror) are added to the simple Michelson interferometer.

1.3.4 Noises in interferometers

There are various kinds of noise sources which disturb the gravitational wave detection with the interferometric detectors. The phase-shifts of the optical paths in the interferometers are induced not only by spacetime distrsions but also vibrations of the optics excited by environmental noises and fluctuations of reflactive indeces in the optical paths. The readouts of the photo detectors can be contaminated by noises in electronics and beam amplitude fluctuation inherent in the light source. This section briefly explains noise sources which fundamentally or possibly degradate the detection probability of gravitational waves.

Seismic noise

The sensitivity of a ground-based detector at low frequnecies is maily limited by vibrations of the optics induced by seismic motions. This is called the seismic noise. The seismic noise can be reduced by isolating the optics from the seismic vibration with vibration isolation systems composed with springs and suspensions. General discussions on seismic vibrations and vibration isolation systems are given in the next chapter.

Newtonian noise

Although the mechanical influence of seismic vibrations can be mitigated by suspending the optics through suitable number of attenuation stages, the direct coupling of the seismic motions through Newtonian gravitational attraction cannot be shielded. This noise, called the Newtonian noise or gravity gradient noise, is the eventual limit of gravitational wave detection on the Earth. It can be reduced by moving the interferometer underground, where the optics are less under the effects of the gravity gradient field of surrounding rocks. The Newtonian noise can also be calculated and subtracted if the seismic noise of the rock is detected by an array of seismometers. More detailed studies on Newtonian noise are found in reference [17].

Thermal noise

The mirrors and their suspension systems are in thermal baths and receive energy from the surrouding field. Random energy flow from the thermal baths causes the fluctuations of the surface and center of mirrors, which induces fluctuation of the optical paths in the interferometer. This noise is called the thermal noise. The thermal noise induced in the mirror substrates is sometimes called the mirror thermal noise, while the noise caused in the suspension systems is distinctively called the suspension thermal noise.

The amount of the thermal fluctuation is related to the loss of the system and the noise spectrum can be estimated by fluctuation-dissipation theorem [18]. In order to mitigate the impact from the thermal noise, one needs to use high quality materal for the mirrors and the suspension components. Since fused silica has a high mechanical Q factor ($\sim 10^7$) at room temperature [19] and good optical property, it is used for the mirror substrates in many interferometric gravitational wave detectors, and also for their suspension fibers in some advanced detectors [20]. The thermal noise can be also reduced by lowering the temperature. Since fused silica has a low quality factor at low temperature, it becomes unusable in cryogenic systems. On the other hand, sapphire and silicon have high quality factors ($\sim 10^8$) and large thermal conductivity at cryogenic temperature [21, 22], and are good candidates for the mirror substrates for cryogenic detectors.

Shot noise

The shot noise is a fundamental disturbance of optical power sensing associated with the quantum nature of light. A photo detector counts the number of photons in a certain measurement time and produces photo current proportional to the incident power. In the process, the counted number of photons, i.e. electrons produced and contributing to the photo current, has the Poisson distribution, which results in fluctuation of photon number. The noise induced by this fluctuation is called the shot noise.

The fluctuation of length sensing due to the probability distribution is proportional to the square-root of the incident power on the mirrors $\sqrt{P_{\rm in}}$. On the other hand, the signal amplitude of the gravitational wave is proportional to $P_{\rm in}$, therefore the signal to noise ratio is proportional to $1/\sqrt{P_{\rm in}}$. Consequently, the shot noise can be reduced by increasing the power of the laser. This motivates one to introduce high laser power and the power recycling scheme.

Radiation pressure noise

When a photon is reflected by a mirror, a back action force is exerted onto it. Owing to the quantum nature of light, the number of the photons hitting on the mirror fluctuates, and thus the back action force fluctuates resulting in displacement noise of the mirror. The noise caused by this fluctuation is called the radiation pressure noise.

The fluctuation force is proportional to the square-root of the laser power $\sqrt{P_{\rm in}}$. Since the shot noise is proportional to $1/\sqrt{P_{\rm in}}$, there is a trade-off between the shot noise and the radiation pressure noise. There is a limit on the sensitivity of an interferometer called the standard quantum limit (SQL), which corresponds to the quantum mechanical limit of the measurement from the Heisenberg uncertainty principle. Currently various methods to beat this limit are proposed [23].

Laser noise

As a laser interferometric gravitational wave detector measures the length between the mirrors using the wavelength of the laser as a reference, the noises in the laser contaminates its sensitivity. The frequency fluctuation of the laser is in principle cancelled at the interference, if the two arms of the interferometer are identical. However, it is not completely cancelled in a real system because of a small asymmetry of the two arms. Therefore the frequency noise has to be suppressed with active controls in the interferometer.

The intensity fluctuation of the laser also introduces a noise to the output signal of the interferometer. The effect of the intensity fluctuation is minimized when the interferometer is operated at a dark fringe, i.e. in the condition that no light is injected to the photo detector in absence of gravitational wave signals. However, in practice, there remains a light intensity by residual motions of the mirrors. The fluctuation of the intensity contaminates the output of the detector and the residual motion around the fringe couples with the intensity noise of the laser. Therefore the intensity of the laser has to be stabilized and the control gain has to be large enough to suppress the residual mirror motions.

Residual gas noise

The random motions of molecules cause fluctuation of the refraction index in the optical paths of an interferometer. This causes the fluctuation of the effective arm lengths and the noise is called the residual gas noise. Terrestrial interferometric gravitational wave detectors nowadays are operated in an ultrahigh vacuum condition (10^{-6}-10^{-7} Pa) to mitigate the impact from the residual gas noise. Therefore the optics and suspension systems are designed to have small outgassing rates and the components materials are restricted.

Control noise

During the operation of an interferometer, the optical components of the interferometer are controlled to keep the Fabry-Perot arms and recycling cavity in resonance and the detection port at a dark fringe. Several auxiliary beam monitoring signals are used for these feedback loops. Detection and digitization noise of these auxiliary detectors, as well as the noise of the electric circuits for the control may contaminate the sensitivity of the interferometer. Although this is not a fundamental noise, careful consideration and design are required to minimize the noise.

The noise in the active controls of the suspension systems can also contaminate the detector sensitivity. The noises in local sensors and actautors introduce vibration to the suspension system components through active controls and cause fluctuation of mirror displacements. The motivation and strategies of the active suspension controls will be discussed in chapter **??**.

Scattered light noise

Although the reflection surfaces and substrates of the mirrors are carefully designed and manufactured, part of the laser beam injected to the mirrors disperses in various directions due to inperfection or inhomogeneity. Scattered light from the mirrors interacts with the surfaces of surrounding mechanical components, which are vibrating with seismic motions, and then is recombined to the main laser beam resulting in the phase noise of the interferometer. Therefore in interferometeric gravitational wave detectors, scattered light has to be damped by placing black-coated optical baffles in appropriate positions to avoid introducing the scattered light noise.

1.4 Large-scale terrestrial laser interferometers

A number of large-scale laser interferometers have been constructed around the world in purpose for capturing first gravitational wave signals and opening new era of astronomy with gravitational waves. The studies on gravitational waves require coincident observations with several detectors in order to improve detection reliability and locate source positions in the sky. This section describes world-wide networks of gravitational wave observatories with large-scale interferometers, which have been constructed or are proposed.

1.4.1 Overview of detector projects

Large-scale terrestrial interferometers operated or planned are summarized in table 1.1. The first generation detectors (TAMA [24], GEO [25], LIGO [26], Virgo [27]) have performed scientific observations since 1999. The first generation detectors had detection probabilities of gravitational wave events about a few percent per year. Although gravitational waves have not been detected by their observations, they demonstrated the effectiveness of the working principle and set upper limits to several gravitational wave sources [28].

Based on the experience gathered with the first generation detectors, second generation detectors have been designed, with approximately thousands of times higher probability of

Generation	Project	Baseline	Observation	Place
1st	TAMA	300 m	1999∼	Mitaka, Japan
	GEO	600 m	2000∼	Hannover, Germany
	LIGO	4 km/2 km	2001∼	Livingston/Hanford, USA
	Virgo	3 km	2002∼	Pisa, Italy
2nd	Adv. LIGO	4 km	2016∼	Livingston/Hanford, USA
	Adv. Virgo	3 km	2016∼	Pisa, Italy
	KAGRA	3 km	2018∼	Kamioka Japan
3rd	ET	10 km	2025∼	under discussion

Table 1.1: Large-scale terrestrial interferometric gravitational wave detector projects.

gravitational wave detection. Several first generation detectors were upgraded (enhanced LIGO, Virgo+) with the sensitivities improved by introducing higher power lasers and advanced techniques such as monolithic suspensions [27]. They have been further upgraded to the second generation detectors (advanced LIGO, advanced Virgo) and are scheduled to start scientific observation in 2016. A Japanese second generation detector KAGRA [29] was funded in 2010 and is being constructed to follow up the observations. In addition to the same improvements of the advanced interferometers, it features the use of cryogenic mirrors and underground environment, which are unique characteristics in the first and second generation detectors. KAGRA scheduls to start scientific observation in 2018.

To go beyond the sensitivities of these detectors, there is a plan to construct a third generation detector, ET (Einstein Telescope) [30], which has been designed by European research institutes. It aims to reach a sensitivity about a factor of 10 better than the second generation detectors. The detector is planned to be constructed underground in order to suppress the eventual sensitivity limit by Newtonian noise and expand the detection band toward lower frequencies.

1.4.2 Optical configuration

The first generation detectors mainly employed power-recycled Fabry-Perot Michelson interferometers. In purpose for improving the sensitivity and optimizing the detection bandwith, they are upgraded to dual-recycled Fabry-Perot Michelson interferometers in the second generation detectors. Fiugre **??** shows a typical optical configuration of the second generation interferometers.

Seed laser from a Nd:YAG non-planar ring oscillator (NPRO), which has significant low intensity noise, is introduced to fiber/solid-state amplifiers, resulting in the power amplified up to the level of ∼200 W. The laser is then sent to prestabilization system, where the phase of the laser is stabilized using solid cavities and phase/amplitude modulation is applied for interferometer sensing and controls. The input mode cleaner, noted as MC, filters the spatial modes and polarization of the laser beam with a triangular optical cavity consisting of suspended mirrors. It also provides frequency reference for the laser at high

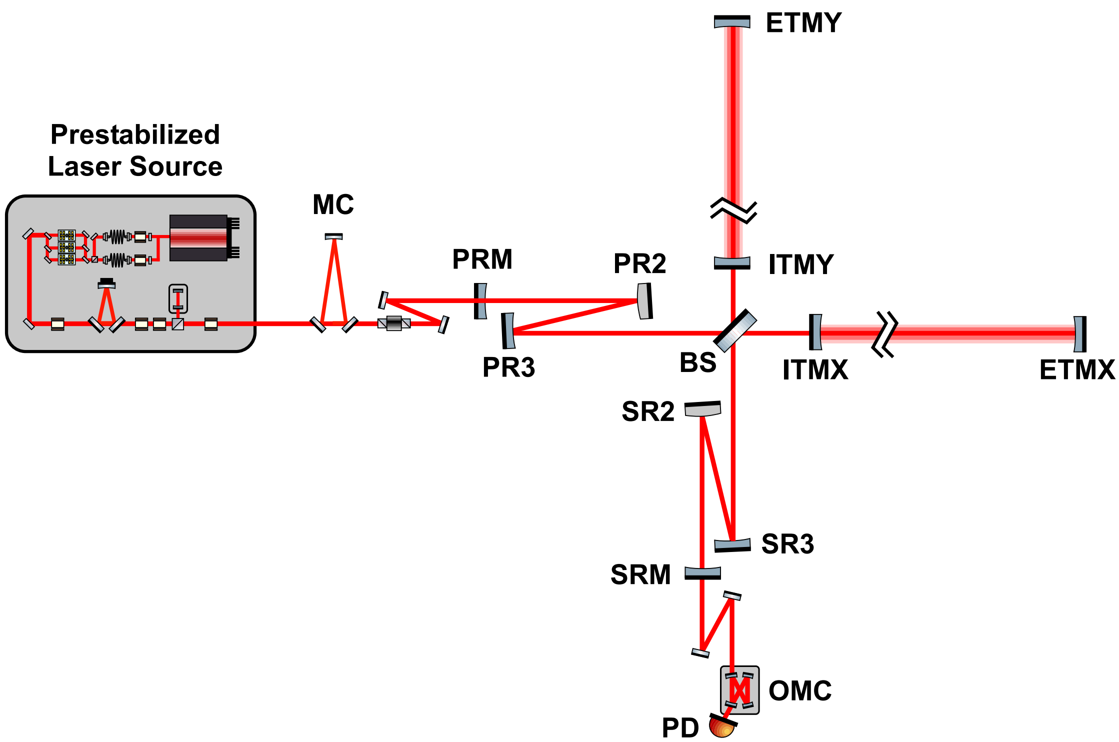

Figure 1.7: Optical configuration of the second generation gravitational wave detector (in the case of KAGRA). MC and OMC denote the input mode cleaner and the output mode cleaner, respectively.

frequencies.

The main interferometer part configures a dual-recycled Fabry-Perot interferometer with km-scale arm lengths. The beam between recycling mirrors and the beam splitter is folded in Z-shapes for improving the spatial mode stability of the recycling cavities. At the downstream of the signal recycling mirror, there is an output mode cleaner (OMC) used to remove unwanted higher-order spatial modes from the output beam. Optical design and reasoning behind design choices in the KAGRA interferometer are decsribed more in details in reference [31].

1.4.3 Detector sensitivities

Fiugre 1.8 shows estimated noise curves of 1st-3rd generation gravitational wave detectors in stran sensitivties. The LIGO detector reaches its design sensitivities in 2007 and achieve the noise level in the strain sensitivity of $3 \times 10^{-23}[1/\sqrt{\mathrm{Hz}}]$ at 100 Hz. The detector is sensitive enough to capture the gravitational wave signals from binary neutron stars of 1.4 solar masses at a distance of 15 Mpc, with a signal to ratio of 8 (averaged over sky directions and source orientations). This distance is one of standard measures of

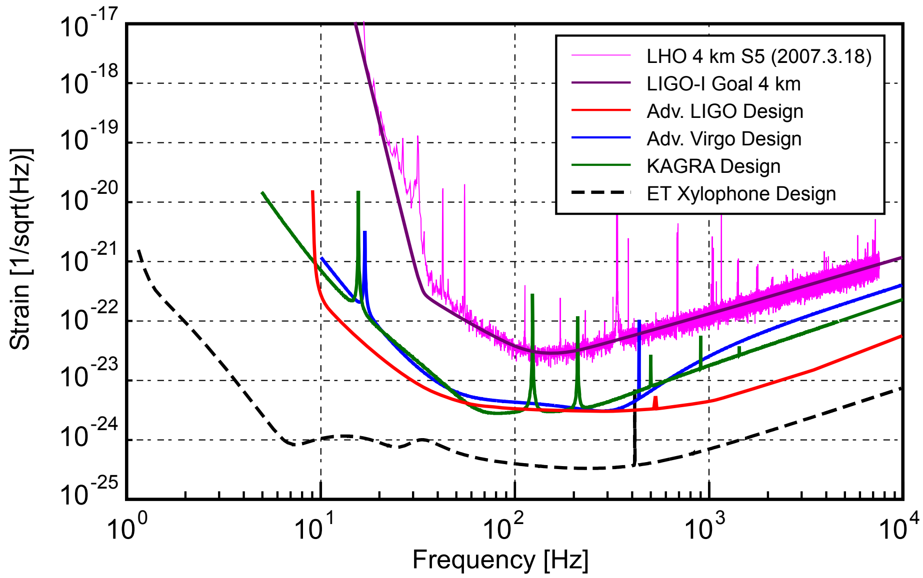

Figure 1.8: Predicted noise spectra of 1st-3rd generation gravitational wave detectors in spacetime strain equivalent. The measured noise spectrum of the LIGO Hanford 4 km interferometer in the 5th science run is also shown for comparison.

gravitational wave detectors' sensitivities and is called the (binary neutron star) inspiral range. The noise curve has a steep cutoff around 40 Hz, which limits the detection band in the low frequency side and is mainly caused by seismic disturbances.

The second generation detectors are designed to expand the detection band to as low frequencies as 10 Hz, and also lower the noise level at high frequencies by about one order of magnitude. This results in pushing insprial ranges as far as 200 Mpc. Once the detectors reach their design sesitivities, they are expected to detect the gravitational wave signals from neutron star binaries multiple times per year.

Contribution of various noises to the detector sensitivities is shown in figure 1.9 in the cases of KAGRA and advanced LIGO. The sensitivities of the second generation detectors are limited by quantum noise (combination of shot noise and radiation pressure noise) and thermal noise in the detection frequency band. The sensitivities at low frequencies are limited by seismic noise which forms steep "walls" in the noise curves below 10 Hz.

1.5 Motivation of improving low frequency sensitivity

As seen in the previous section, sensitivities of terrestrial gravitational wave detectors at low frequencies are limited by seismic noise and thus the performance of vibration isolation systems affects the detectability and measurability of low frequency gravitaitonal wave signals. This section briefly explains possible rewards for expanding the detection band of gravitational waves toward low frequencies.

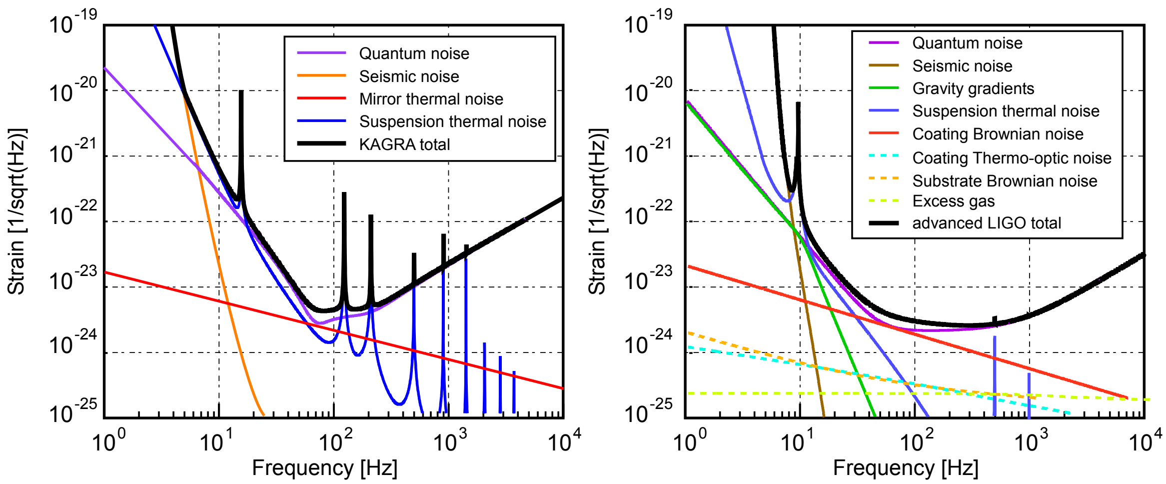

Figure 1.9: Noise budgets of KAGRA (*left*) and advanced LIGO (*right*) [32, 33].

1.5.1 Binary neutron stars

Detectability of gravitational waves from a binary neutron star coalescence is not strongly affected by the detector sensitiviy around 10-40 Hz, since the system emits large amplitude of gravitational waves just before the coalescence, where gravitational waves have frequency components of 100-1000 Hz. However, the low frequency sensitivity can affect efficiency and accuracy in estimating astrophysical parameters of the binary system from the observed gravitational wave signals. For instance, a study on paremeter estimation algorythm shows that computation of paremeters on non-spinning binary neutron star inspirals can be sped up by a factor ∼150 when the low frequency limit of the sensitivity decreases from 40 Hz to 10 Hz [34].

1.5.2 Binary black holes

Although the existence of intermediate-mass black holes (IMBHs), with mass ranging between $10^2 - 10^4 M_\odot$, has not been confirmed by optical observations, they are of high interested for astrophysics and gravitational waves from IMBH binary systems have been intensively studied [35]. An IMBH binary with a total mass of $\sim 800 M_\odot$ for instance emits gravitational waves of 10-40 Hz in the merger and ringdown phases. Thus the detectability of gravitational waves from IMBH binaries is strongly affected by the low frequency sensitivity.

1.5.3 Supernovae

Detection of burst gravitational waves will not be affected by the detector sensitivity at 10-40 Hz, but the extraction of physics may be affected once the gravitational wave signals are obtained. Several explosion models of supernovae, such as magnetohydrodynamic

(MHD) explosion [36] and neutrino-driven conevtion with Standing Accretion Shock Instability (SASI) [37], provide gravitational waves with low frequency components (below 100 Hz). Thence improved sensitivity at low freqencies can contribute in distinguishing explosion mechanisms of supernovae.

1.5.4 Pulsars

Bunch of known pulsers from radio astronomy have possibility of emitting gravtational waves in the frequency band between 10-40 Hz. The Vela pulsar, which rotates at 11.19 Hz and is expected to emit 22.39 Hz gravitational waves, is one of the candidates which can possibly emit gravitational waves in detectable amplitude. A number of known pulsars, with rotation frequencies higher than 10 Hz, have been investigated by coincident searches in first generation gravitational wave detectors and set upper limits on the emitted gravitational wave amplitude [38]. Having better sensitivities at low frequencies would provide better upper limits on the gravitational wave amplitude and possibility of detecting them.

Vibration Isolation

Chapter 2

Stationary seismic vibration is one of the fundamental and inevitable noise sources in terrestrial gravitational wave detectors. Seismic noise limits the detector sensitivities at low frequencies and restricts the detection band. This chapter addresses characteristics of seismic vibration and mechanisms to reduce its contribution to the detector sensitivity. Integrated vibration isolation systems for gravitational wave detectors are then introduced in the last section of this chapter (section 2.5).

2.1 Seismic motion

The continuous and random motion of the ground is induced by natural phenomena like oceanic and atmospheric activities, as well as by human activities. The amplitude of the seismic motion varies by a few orders of magnitude from site to site and from time to time, depending on the surrounding environment such as weather and traffic condition in nearby cities.

J. Peterson set out characterization of seismic background noise by cataloguing data from a worldwide network of seismometer stations [39]. He derived the New High/Low Noise Model (NHNM/NLNM) from the upper and lower bounds of measured power spectral densities, which provide standard measures for comparison of stationary seismic spactra. Figure 2.1 shows the data and the upper/lower bounds set from Peterson's study.

The power spectrum densities increase rapidly at low frequencies below 1 mHz, where the Earth is subjected to tidal deformation due to gravitational attraction from the sun and the moon. This seismic motion at the very low frequencies displaces the test masses in the gravitational wave detectors coherently and thus doest not affect the interferometer operation or the detectability of gravitational waves. The remarkable peak observed around the periods of 2-10 s is known as the microseismic peak. It is caused by oceanic wave activities and therefore the peak is observed strongly along the coast and weakly in the middle of continents [40]. In the large-scale gravitational wave detectors, the seismic motion around the frequencies is not coherent in the places where the test masses locate, and thus can cause differential displacements between them. Therefore it is mandatory to

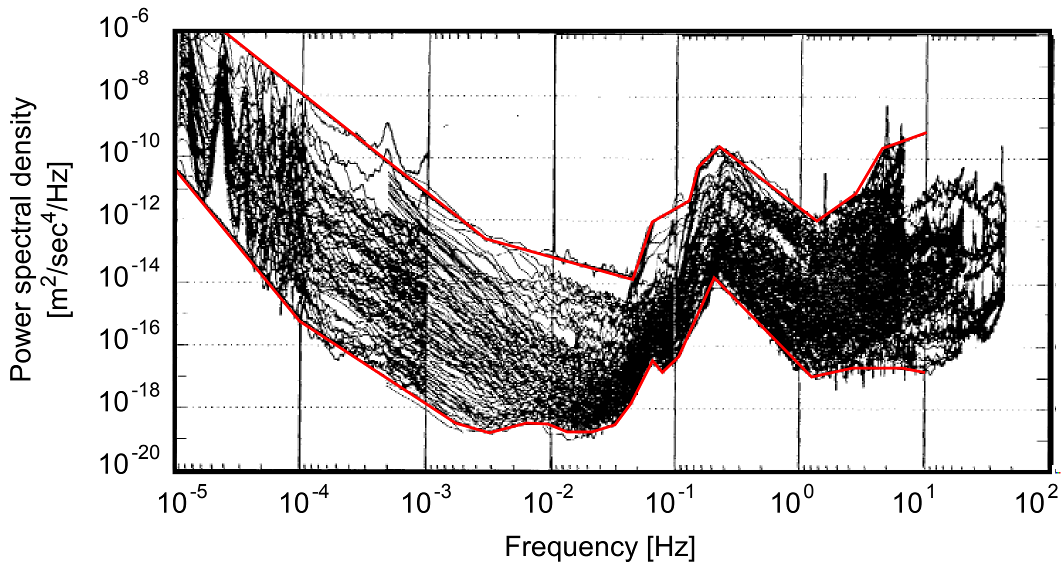

Figure 2.1: An overlay of seismic vibration spectra in Peterson's study together with the New High and Low Noise Model [39].

suppress the impact from microseismisms for stable operation of the interferometers.

The seismic motions at high frequencies above 1 Hz are studied in the field of gravitational wave detection, since they can contaminate the detector sensitivities through its mechanical transmission to the optical components. Figure 2.2 shows typical power spectrum densities of the seismic vibration measured at the sites of gravitational wave detectors. Seismic vibration has almost the same somplitude in all three arthogonal directions, and the power spectrum densities of high frequency components (> 1 Hz) are typically written in the form of

$$\tilde{x}_{\mathrm{seism}}(f) = A \times \left(\frac{f}{1\ [\mathrm{Hz}]}\right)^{-2}\ [\mathrm{m}/\sqrt{\mathrm{Hz}}]. \tag{2.1}$$

The amplitude factor A varies from site to site and typically ranges in 10^{-6}-10^{-9}.

The amplitude of the seismic motion in the KAGRA site (inside the Kamioka mine) is smaller than that in other places by 2-3 orders of magnitude. It is known that the seismic vibration decreases significantly in underground environment, since the surrounding rocks isolate the vibration from atmospheric and human activities on ground surface [?]. This becomes a big motivation to build gravitational wave detectors underground regardless of practical difficulties such as construction costs and safety issues. The isolation especially works at high frequencies above 1 Hz, where the vibration originates in acitivities on the ground surface. On the other hand, the microseismisms at 0.1-1 Hz are not attenuated much since the vibration propagates through the continents.

The typical amplitude of the seismic motion is around 10^{-12}-10^{-10} m/$\sqrt{\mathrm{Hz}}$ at 100 Hz. On the other hand, the expected amplitude of the arm length variation due to a

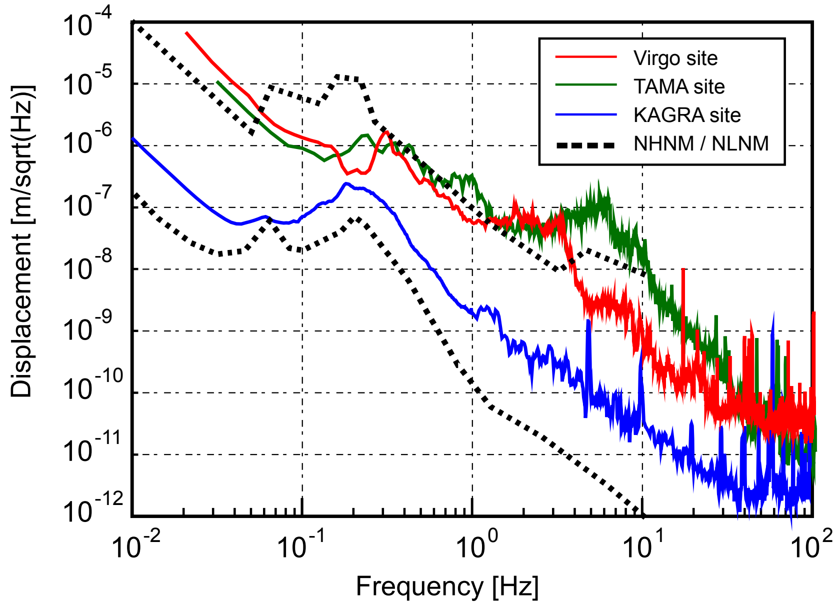

Figure 2.2: Typical power spectrum density of seismic vibration displacements at several sites of gravitational wave detectors [41].

gravitational wave is typically in the order of 10^{-20} m/$\sqrt{\text{Hz}}$ at that frequency. This means that an attenuation factor of 10^8-10^{10} is required for detection of gravitational waves.

2.2 Passive mechanical filter

2.2.1 Dynamics of harmonic oscillator

Isolation from seismic motion can be realized by the use of mechanical filters with elastic components, such as springs and suspension wires. As the simplest example, consider a one-dimensional harmonic oscillator shown in figure 2.3. The oscillator consists of a spring with a spring constant of k and a suspended payload with mass of M. The displacements of the suspension point and the payload are denoted as x_0 and x respectively. The equation of motion of this system is written as

$$M\ddot{x} = -k(x - x_0). \tag{2.2}$$

This equation can be solved in the frequency domain by taking Fourier transform as

$$H(\omega) \equiv \frac{\tilde{x}(\omega)}{\tilde{x}_0(\omega)} = \frac{1}{1 - (\omega/\omega_0)^2}, \tag{2.3}$$

where $\omega_0 = 2\pi f_0 = (k/M)^{1/2}$ is the resonant angular frequency of the system. $H(\omega)$ is called the transfer function from the motion of the suspension point to the payload motion.

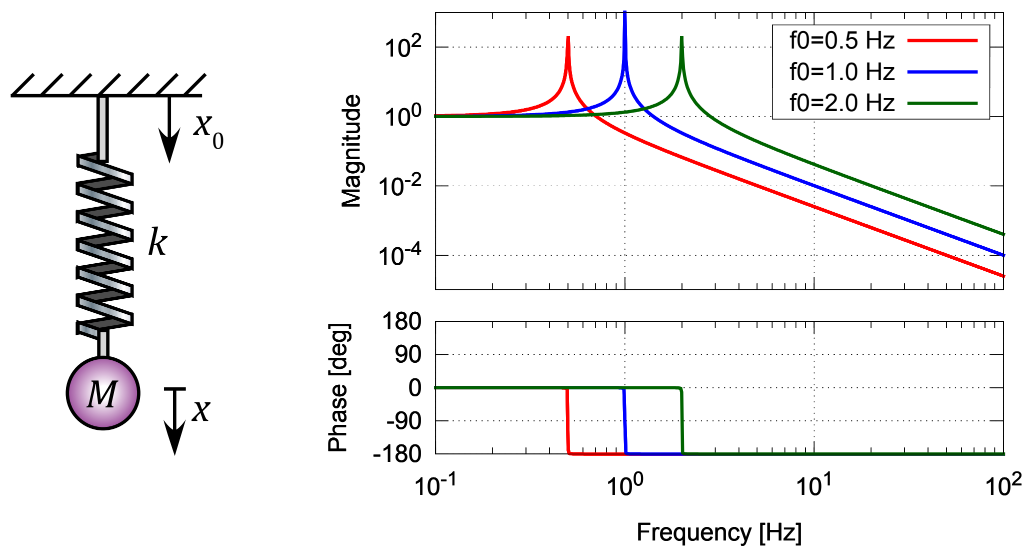

Figure 2.3: A spring-mass system as a mechanical filter (*left*) and its transfer function ($\tilde{x}/\tilde{x}_0$) with various resonant frequencies (*right*).

The amplitude and phase of $H(\omega)$ are plotted as a function of frequency in figure 2.3 with various resonant frequencies.

At low frequencies ($f \ll f_0$) the transfer function is close to one, which means that the motion of the payload follows that of the suspension point. Around the resonant frequency, the amplitude of the transfer function increases and, in absence of dissipation, goes to infinity at the resonant frequency. In the high frequency region ($f \gg f_0$) the amplitude of the transfer function rolls off in proportion to f^{-2}, resulting in isolation of the suspended mass from the vibration of the suspension point. The vibration isolation ratio is approximately written as $(f/f_0)^{-2}$ at any given frequency above the resonance, which indicates that the suspended mass is isolated more by a mechanical filter with lower resonant frequency.

In actual system, the transfer function does not diverge at the resonance due to the existence of dissipation. There are several dissipation mechanisms such as residual gas damping and thermoelastic damping. The dissipation caused by anelasticity in the elastic components is often called the structural damping and is expressed by adding imaginary part to the spring constant as $k \to k(1+i\phi)$, in the frequency domain. Here ϕ is called the loss angle and is defined as the phase angle by which the displacement response x would lag behind a sinusoidal driving force applied to the payload. Typically $\phi \ll 1$ and the loss angle is related to the oscillator's quality factor as $Q = 1/\phi$. A number of measurements show that the intrinsic loss angles of elastic materials are independent to the frequency [?]. The resulting transfer function (2.3) has a peak amplitude of $1/\phi$ at the resonant frequency.

2.2.2 Multi-stage suspension

In an interferometric gravitational wave detector, every test mass is suspended as a pendulum so that it behaves as a free particle in the sensitive plane of the interferometer. This suspension also works as a mechanical isolator from the ground vibration. The resonant frequency of the pendulum is around 1 Hz with a reasonable length (a few tens of cm), therefore the vibration isolation ratio is about 10^{-4} at 100 Hz. Since the required attenuation is around $10^{-10} \sim 10^{-8}$, seismic attenuation by a simple pendulum is not sufficient for the detection of gravitational waves.

The required seismic attenuation is obtained by cascading mechanical filters, whose resonant frequencies are sufficiently lower than the frequency region of interest ($\gtrsim$ 10 Hz in second generation detectors). In an N-stage chain of mechanical filters, the ground motion transmits to the suspended mass with an attenuation factor proportional to f^{-2N}, at a frequency higher than the resonant frequencies of the chain. Figure 2.4 shows the attenuation performance of a multi-stage pendulum with various stage numbers. By employing sufficient numbers of isolation stages, strong attenuation of the seismic noise can be achieved in the high frequency region.

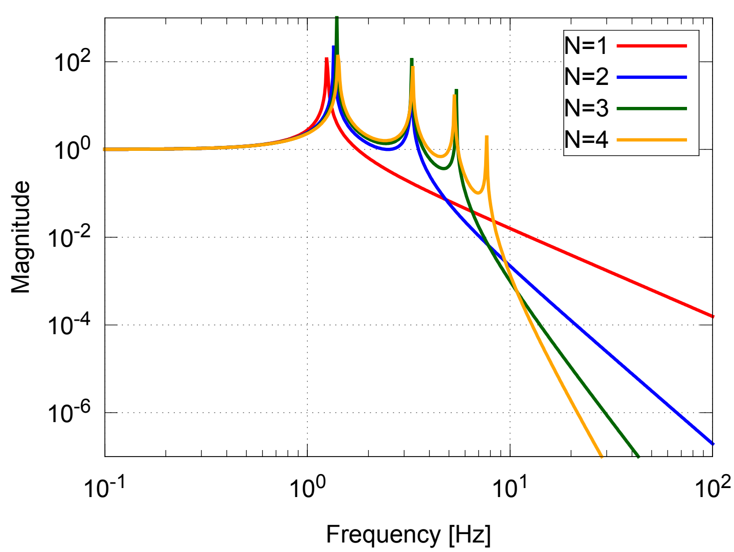

Figure 2.4: The amplitudes of the transfer functions of an N-stage multi-pendulum with $N = 1 \sim 4$, from the suspension point displacement to the bottom mass displacement. The total length of the pendulum is set 1 m in all cases.

2.2.3 Couplings from vertical and rotational motions

Since the horizontal ground motion transmits directly to the horizontal motions of the mirrors and contributes to the changes in the optical path lengths of the interferometer, isolation from the horizontal ground vibration is the most critical issue in gravitational wave detectors. However, isolation from the vertical ground vibration is also indispensable in practice. This is because 0.1-1% of the vertical motion is transferred to the horizontal direction by mechanical imperfections in each attenuation stage and ultimately by the non-parallelism of the verticality at kilometers apart locations in the interferometer. As shown in figure 2.5, the front and end mirrors of the Fabry-Perot cavities form an angle of $\alpha = L/2R_\oplus$ with the interferometer's global vertical direction. Here L is the cavity length and $R_\oplus$ is the radius of the Earth. Thence a vertical displacement δz has an effect along the beam direction, producing a variation $\alpha\delta z$ of the cavity length. In the case of 3-km length interferometer, the minimum coupling due to the Earth curvature is calculated as $\alpha \sim 2 \times 10^{-4}$.

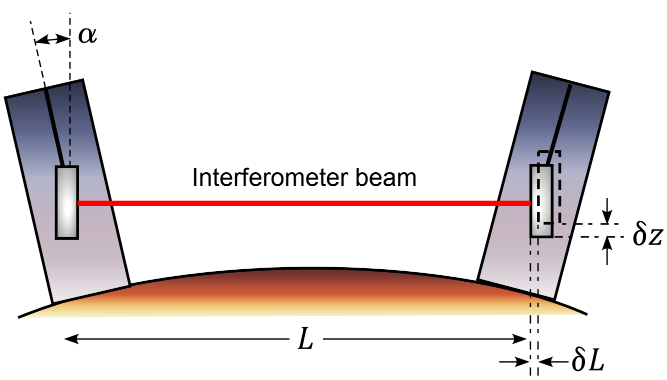

Figure 2.5: Effect of the Earth curvature.

Not only the vertical motions but the rotational motions of the mirror may affect the sensitivity of the interferometer. The rotational motion of a mirror does not change the optical path length ideally if the laser beam illuminates the center of the mirror. However, the beam spot is off-centered to some extent in reality, and an angular displacement causes a variation of the optical path length as shown in figure 2.6. When the beam spot is misaligned by a distance of d from the center, the rotation angle of the mirror $\delta\theta$ couples with the length variation along the beam axis by $d\delta\theta$.

2.3 Damping of suspension system

2.3.1 Stable Operation of interferometers

Seismic motion affects not only the sensitivity of the interferometer, but also its stability. Although the chains of mechanical filters isolate the optics from seismic motion in a high frequency region, the mirror motions can be largely excited at low frequencies, especially at the resonant frequencies of the mechanical components. As the Mechelson

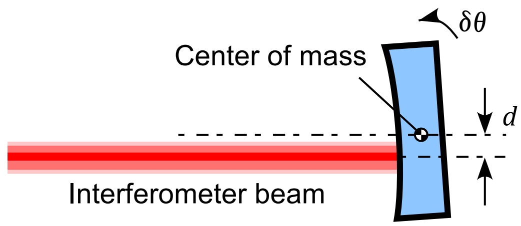

Figure 2.6: Coupling from the rotational motion of the mirror due to misalignment.

interferometer and the Fabry-Perot cavities must be kept in the dark fringe / the resonant condition by feedback controls, the RMS (Root Mean Square) amplitude of the mirror displacement and velocity have to be suppressed within the limited range of the controls.

The RMS amplitude of the ground motion displacement (integrated down to $\lesssim 0.1$ Hz) is typically in the order of microns at the surface and submicrons for underground. As the main contribution to the RMS amplitude is concentrated in the low frequency band ($\lesssim 1$ Hz), the resonant peaks of the mechanical system in this frequency region must be suppressed. The microseismic peak around 0.2-0.5 Hz contributes to most of the seismic RMS amplitude, therefore one tries to place the mechanical resonances away from this region. In underground locations, the microseismic motion itself is largely coherent across the entire interferometer, therefore it would be of little ill effect on the interferometer stability. The actual problem is that the resonances of the seismic isolation system can be excited with different and varying phases, thus resulting in large relative motions of the interferometer mirrors. Therefore the resonances of the seismic attenuation chains must be damped strongly.

Another reason for introducing damping mechanisms is to enhance robustness to unwanted acceleration disturbances such as earthquakes and miscontrol actuation forces. Such disturbances excite the mechanical resonances and the oscillation at the resonant frequencies remains for a long period unless they are appropriately damped. The interferometer cannot be operated while the mirrors are swinging in large amplitudes and thus the time for observation is reduced. It is essential to suppress the decay time of mechanical resonances which are possibly excited by external disturbances and affect the operationability of the interferometer.

2.3.2 Passive damping

There are fundamentally two ways of damping the mechanical resonances: passive and active damping. Passive damping can be achieved by adding a viscous damper which outputs a braking force proportional to the relative velocity between the damper and the object to be damped. Figure 2.7 shows a conceptual design of a viscously damped

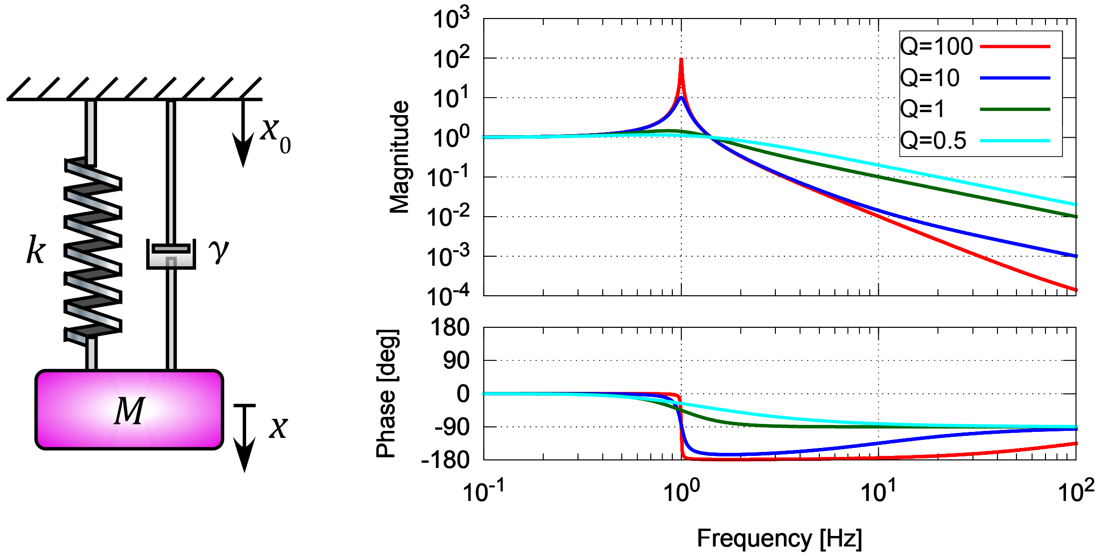

Figure 2.7: (*Left*)A mechanical oscillator with a viscous damping mechanism represented by a dashpod. (*Right*) Bode plots of the transfer function with various quality factors.

mechanical oscillator. The equation of motion of the system is written as

$$M\ddot{x} = -k(x - x_0) - \gamma(\dot{x} - \dot{x}_0), \tag{2.4}$$

where γ is the damping coefficient of the damper. The damping force provides dissipation to the system in addition to structural damping caused by the spring's internal friction. The structural damping contribution is typically much smaller than that from an implemented damper. From the Fourier transform of this equation, the frequency response of the suspended mass displaecment to the ground vibration is calculated as

$$H(\omega) = \frac{1 + 2i\eta(\omega/\omega_0)}{1 + 2i\eta(\omega/\omega_0) - (\omega/\omega_0)^2}, \tag{2.5}$$

where the damping ratio η is given by $\eta = \gamma/2M\omega_0$. A system with dissipation is often characterized by a quality factor of the resonance, which is given by $Q = \frac{1}{2\eta}$.

The amplitude and the phase of the transfer function $H(\omega)$ with various quality factors is plotted in figure 2.7. There are two important characteristics in the transfer function of the viscously damped system. First, the height of the peak at the resonance ($f = f_0$) gets smaller when the damping gets stronger, and is roughly equal to Q in case of $Q \ll 1$. Second, the amplitude of the transfer function rolls off in proportion to only f^{-1} above the frequency Qf_0, instead of f^{-2} observed in the system with no dissipation. Thence the performance of the mechanical filter is degraded at high frequencies in viscously damped system.

The robustness of the mechanical filter to acceleration disturbances can be seen in an impulse response to a driving force on the suspended mass. Figure 2.8 shows the impulse response of a viscously damped mechanical oscillator with various damping factors. When the system has small dissipation, the displacement of the suspended mass decays with sinusoidal oscillation. The oscillation amplitude decays faster as the damping factor increases and the typical decay time, in which the oscillation amplitude decreases by a factor of $1/e$, becomes $\tau = \frac{1}{\eta\omega_0} = \frac{Q}{4\pi f_0}$. In the critical damping condition where the damping factor η reaches 1 (or $Q = 0.5$), the suspended mass no longer oscillates and the displacement decays by decay time of $\tau = \frac{1}{\omega_0}$. When the damping becomes even stronger ($\eta > 1$, in the over-damped condition), the suspended mass gets harder to be displaced but on the other hand the decay time gets longer than that of the critically damped oscillator, since the damper resists the suspended mass from recovering to its original condition.

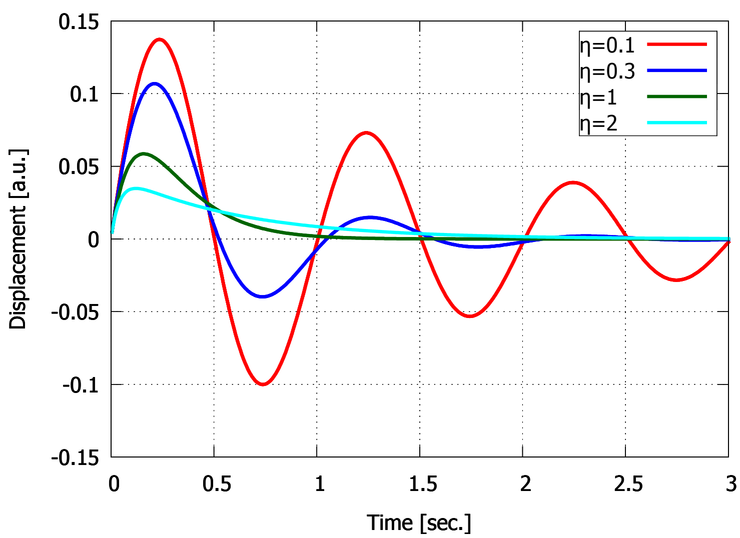

Figure 2.8: Response of a viscously damped mechanical oscillator with various damping factors to an impulsive force exerted to the suspended mass.

The degradation of vibration isolation perfromance due to a damper can be avoided by isolating the damper from the ground vibration by means of another mechanical filter as shown in figure 2.9. This technique is called flexible damping. Although the additional spring introduces another resonance to the system, the amplitude of the transfer function falls in proportion to f^{-2} at high frequencies like in the case with no dissipation (see the plots in figure 2.9).

2.3.3 Actual implementation of viscous dampers

One simple way to implement viscous damping in the suspension system is the use of an eddy current damper [42], which is composed of permanent magnets on the damper acting

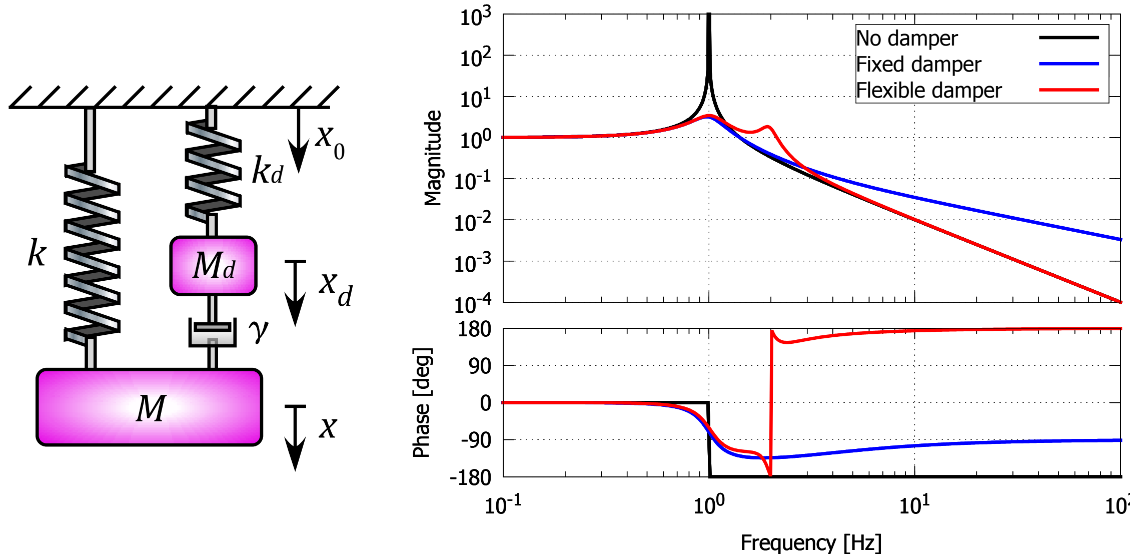

Figure 2.9: (*Left*)A mechanical oscillator with a flexible damping mechanism. (*Right*) Comparison of the transfer functions of the mechanical filter with no damper, a fixed damper, and a flexibly supported damper.

on and conductive objects placed on the oscillator to be damped. When a conductive material experiences a time-varying magnetic field, eddy currents are generated in the conductor. These currents generate a magnetic field with opposite polarity of the applied field and a delay due to the induced field decay, causing a resistive force. Figure 2.10 illustrates the working mechanism of an eddy current damper. The damping coefficient caused by an eddy current damper can be described as

$$\gamma_x = A\sigma B \frac{\partial B}{\partial x}, \tag{2.6}$$

where B is the magnetic field from a permanent magnet, σ is electrical conductivity of the conductor and A is a factor determined from the geometry of the conductor. In general large damping strength is obtained by the use of a permanent magnet with strong magnetic field and a conductive object with large electric conductivity.

A chief advantage of using eddy current dampers is that it is non-contact system between the damper and the damped objects and thus carries no risk of hystheretic noise caused by mechanical frictions. A possible drawback of using eddy current dampers is direct transmission of the damper motions to the mirror motions through the magnetic field couplings, since most mirrors in the interferometer possess permanet magnets for actuators. Suspension systems with eddy current dampers have been developed for TAMA [43] and the effectiveness has been demonstrated.

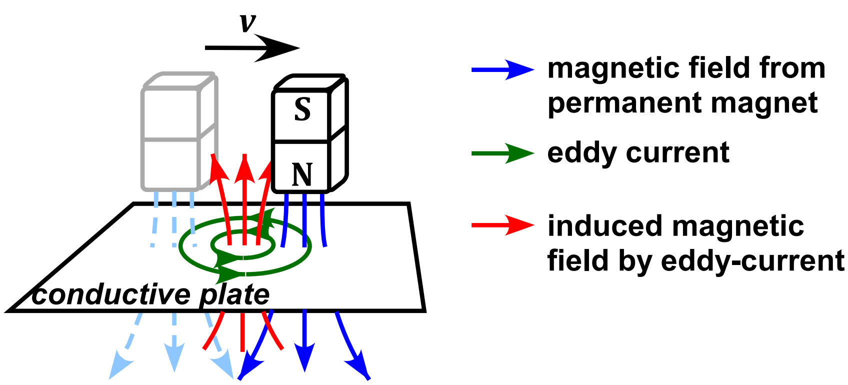

Figure 2.10: An illustration of the working mechanism of an eddy current damper.

2.3.4 Suspension thermal noise

Although viscous damping contributes in suppression of RMS displacement or velocity of the suspended optics and stable operation of the interferometer, it can degradate the detector sensitivity by inducing thermal fluctuation of the suspended mirrors in the detection band of gravitational waves. The fluctuation and dissipation theorem provides a general relation between the frequency response of equilibrium systems to external perturbation forces ($H_{\mathrm{f}}(\omega)$) and the power spectrum density of their spontaneous fluctuations ($S_{\mathrm{th}}(\omega)$) with the following formula:

$$S_{\mathrm{th}}(\omega) = -\frac{4k_BT}{\omega}\mathrm{Im}[H_{\mathrm{f}}(\omega)]. \tag{2.7}$$

Here k_B is the Boltzmann constant and T represents the temperature of the equilibrium system. In a viscously damped system, the power spectrum density of harmonic oscillator's thermal fluctuation can be calculated as

$$S_{\mathrm{th}}(\omega) = \frac{4k_BT}{M}\frac{2\eta\omega_0}{(\omega_0^2-\omega_0)^2+4\eta^2\omega_0^2\omega^2}. \tag{2.8}$$

Figure 2.11 shows sprctra calculated from the equation. The amplitude spectrum density gets in proportion to f^{-2} in the detection band and reaches 10^{-17}-10^{-16} [m/$\sqrt{\mathrm{Hz}}$] at 100 Hz. This is not applicable in gravitational wave detectors since expected gravitational wave signals are in the order of 10^{-20} [m/$\sqrt{\mathrm{Hz}}$].

In a multi-stage suspension, the impact from thermal fluctuation induced by viscous dampers can be mitigated by placing the dampers on upper stages, since as well as seismic vibration, the thermal vibration is filtered out by mechanical filters. Passive dampers should be set well apart from the optics so that thermal fluctuation due to their dissipation does not limit the detector sensitivities.

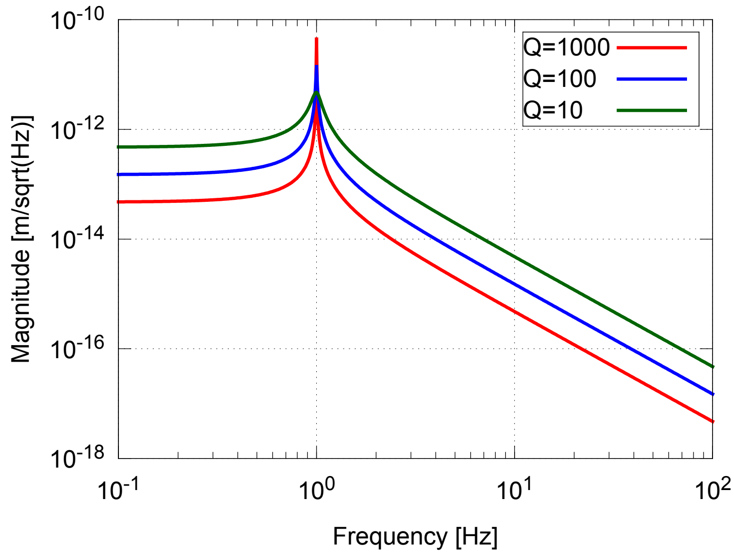

Figure 2.11: Predicted amplitude spectrum densities of thermal displacement fluctuation of viscously damped harmonic oscillators, assuming $T = 300$ [K], $M = 30$ kg and $f_0 = 1$ Hz.

2.3.5 Active damping

The use of passive damping has advantages such as low cost, robustness, low complexity and ease of implementation. However, magnetic field from permanent magnets diverges in all directions and an eddy current damper implemented for one degree of freedom (DoF) also affects the damping strengths in other DoFs. Therefore it is difficult to design the passive dampers so that the resonances of all the translational/rotational motions of the suspended mass are damped sufficiently. In addition, suspension systems with eddy current dampers suffer from severe suspension thermal noise at high frequencies as described above, therefore one needs to avoid using them near the optics of the interferometer.

In actively damped systems, the vibration of the suspended mass is suppressed by feedback controls with vibration sensors and actuators. The active damping strength can be tuned flexibly and the frequency response can be controlled by designing the servo filters. If one places sensors and actuators with sufficient numbers and proper configuration, the motion of the suspended mass can be controlled in all traslational/rotational DoFs individually. The servo filters of the feedback controls have to be designed carefully so that they do not inject the sensor, actuator and electric circuit noise in the form of random motion of the suspended mass. An advantage of active damping is that, after damping the unwanted oscillations it can be switched off, thus eliminating the control noise.

2.4 Active vibration isolation

Passive isolation systems rely on natural characteristics of mechanical oscillators for vibration reduction of suspended objects. Since a mechanical oscillator can filter out vibration components only above its natural resonant frequency, reduction of low frequency vibration such as motion induced by microseismism (around 0.2-0.5 Hz) is not easily achieved by passive systems. Acitve isolation systems, which implement vibration sensors, actuators and controllers (servos), isolate the target objects from seismic virabtion actively with feedback and feedforward controls. Active systems in principle can reduce the targets' vibration in any frequency band, if vibration sensors with sufficient sensitivities and low noise levels are used.

Figure 2.12 shows a typical control topology of an active isolation system. The isolation platform is supported by suspension springs so that the motion can be controlled with actuators. Vibration of the platform is measured by inertial sensors (seismometers), which sense the platform accelerations in an inertial frame, and the signals are sent to the feedback controller. Since inertial sensors have poor sensitivties at low frequencies, the platform is positioned at DC with respect to the support structure by using relative position sensors. In the feedback controller, signals from inertial sensors and position sensors are blended to compromise the two control loops. Additional isolation performance is obtained by using feedforward inertial sensors measuring the ground vibration. Detailed discussion on the active isolation system can be found in reference [44].

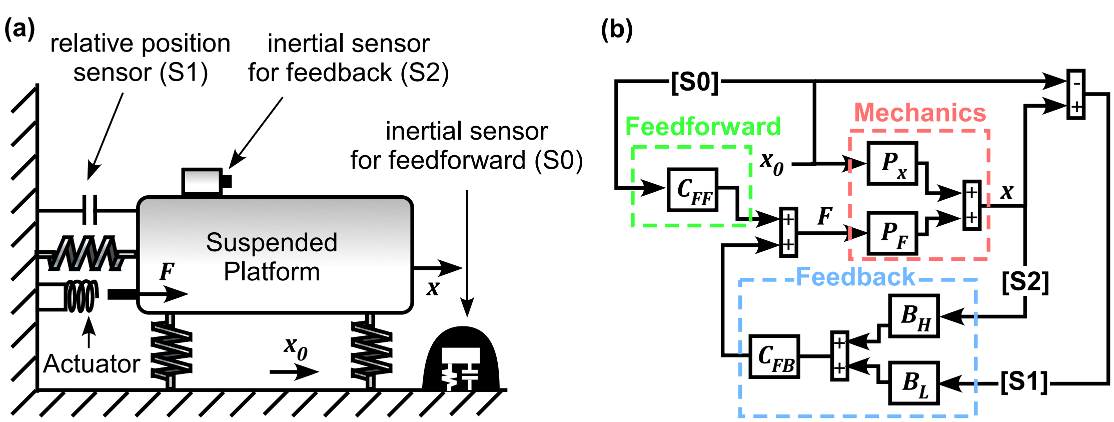

Figure 2.12: (a) A schematic drawing of an active isolation system . (b) A block diagram of the active control scheme.

2.5 Implemented vibration isolation systems

This section briefly introduces various vibration isolation systems implemented for large-scale terrestrial gravitational wave detectors.

2.5.1 Vibration isolation stack

LIGO, GEO and initial configuration of TAMA employ a multiple-stage vibration isolation system called a stack, which consist of alternating layers of metalic masses and elastomer springs, for core optics of the interferometers [45, 46]. Its visual impression is shown in figure 2.13. Elastomers have internal viscoelastic damping, which reduces the quality factors of the mechanical resonances in the order of 1-10. The resonant frequencies typically locates at 2-10 Hz for horizontal modes and 5-20 Hz for vertical modes. It can attenuate seismic vibration above several tens of Hz and provide attenuation factors of 10^{-3}-10^{-6} at 100 Hz. The stack supports a breadboard from which a core optic of the interferometer is suspended through a single or multiple-stage suspension.

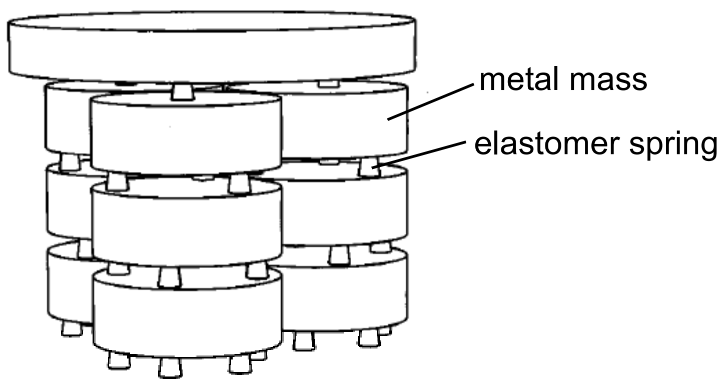

Figure 2.13: Perspective drawing of a vibration isolation stack [45].

The vibration isolation stack is a fully passive and simple system and thus has an advantage in easy implementation. However, the resonant frequencies are relatively high and vibration isolation performance at low frequencies (10-50 Hz) is not sufficient for allowing gravitational wave detection in the frequency band. Additionally, elastromer springs suffer from large creep, which requires the user to adjust the height and tilt of the structure periodically.

2.5.2 Superattenuator

Virgo pioneers in developing low-frequency vibration isolation systems aiming for extending the detection band of gravitational waves to lower frequencies. The core optic of the interferometer is suspended from a vibration isolation system called the Superattenuator [47], which consists of a preisolation stage with inverted pendulums and a chain of mechanical filters (see figure 2.14). A mechanical filter attenuates vertical vibration by the use of metal cantilever springs with a resonant frequecy lowered by magnetic antispring technology [48]. The penultimate stage of the suspension chain is called the marionette, which supports the mirror by four wires and can be steered by coil-magnet actuators from the stage above.

The performance of the superattenuator has been tested in the facility with the interferometer, by actuating the top stage vibration with sinusoidal excitation and measuring the resulting output signals from the interferometer. The experiment demonstrates that the superattenuator achieves in attenuating the vibration by more than 10 order of magnitudes in the detection band of gravitational waves ($>$ 10 Hz) [49]. Virgo reached the design sensitivity in the second science run (VSR2 in 2009) and achieved a significantly low noise level of 10^{-20} $[1/\sqrt{\text{Hz}}]$ at 10 Hz in spacetime strain equivalent.

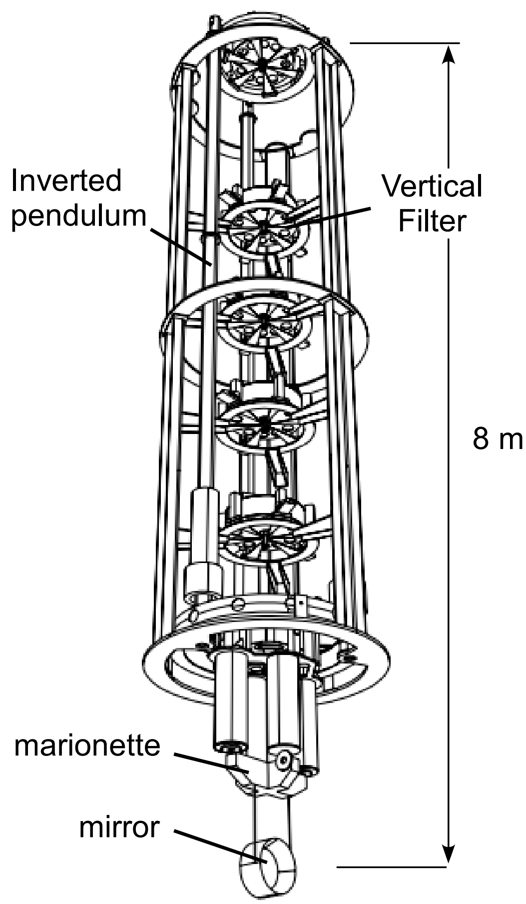

Figure 2.14: An illustration of the Virgo Superattenuator [49].

2.5.3 Seismic attuation system

TAMA replaced its vibration isolation systems for the core optics in 2005-2006 from conventional vibration isolation stacks to low-frequency vibration isolation system called the TAMA-Seismic Attenuation System (SAS) [50]. SAS features in employing mechanical filters with low natural frequencies, i.e. inverted pendulums (IPs) and Geometric Anti-Spring (GAS) filters. The low frequency oscillators contribute in cutting off the seismic noise from a frequency as low as few Hz and extending the detection band of gravitational waves to low frequencies. The second generation detector KAGRA also plans to implement SASs for core optics of the interferometer. More details on SAS will be discussed in the following chapter.

2.5.4 Active isolation platform

Vibration isolation systems in advanced LIGO feature in having active isolated platforms by the use of various vibration sensors and actuators implemented for feedback and feedforward controls. Figure 2.15 shows schematic and CAD drawings of the vibration isolation systems for the core optics, which are placed inside and around vacuum envelops called the Basic Symmetric Chambers (BSC). Three systems are cascaded to provide up to seven stages of seismic isolation to the core optics; the Hydraulic External PreIsolator

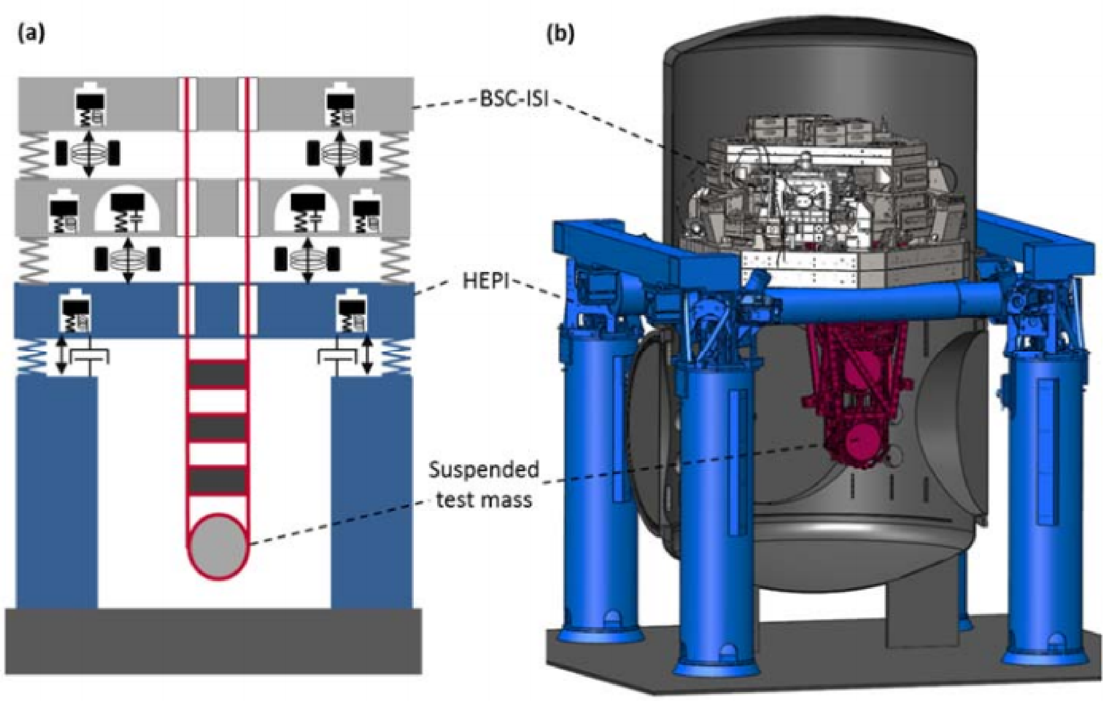

Figure 2.15: (a) Schematic and (b) CAD drawings of the vibration isolation systems supporting the core optics of the advanced LIGO interferometer [44].

(HEPI), the Internal Seismic Isolation platform (ISI) and the quadruple pendulum suspension. HEPI and ISI provide precise positioining and active isolation of a suspension platform, from which the core optic is suspended. The platform is isolated from the seismic vibration from a low frequency ($\lesssim 0.1$ Hz) and into the level of $\sim 10^{-12}$ m/$\sqrt{\text{Hz}}$ at 10 Hz. The seismic isolation systems were installed to the detectors and their robustness and effectiveness have been proved through years of comissioning on the interferometers. The detailed control strategy and measured performance of active isolation system can be found in reference [44].

Seismic Attenuation System

Chapter 3

Vibration isolation systems invented for various gravitational wave detectors were introduced in the previous chapter. This chapter focuses on low-frequency vibration isolation system called the Seismic Attenuation System (SAS). Its general concept and working principles of key mechanical components are briefly introduced.

3.1 General concept

As explained in chapter 2, a mechanical oscillator can provide vibration isolation at frequencies higher than its natural resonant frequency, and thus one of the simplest way to improve the attenuation performance is reducing the natural frequency of the mechanical filter. The Seismic Attenuation System (SAS) aims for improving its seismic attenuation performance at low frequencies by pushing down the natural frequencies of mechanical resonators with the aid of anti-spring technologies.

SAS contains two key mechanical components called the Inverted Pendulum (IP) and the Geometric Anti-Spring (GAS) filter, which provide horizontal and vertical vibration isolation respectively. The resonant frequency of the IP can be lowered to ∼30 mHz and thus it can passively attenuate the ground motion at the microseismic peak (0.2-0.5 Hz), which contributes the RMS amplitude of the mirror displacement/velocity in a large extent. The resonant frequency of the GAS filter can be lowered to ∼200 mHz and it enable us to achive vertical attenuation performance comparable to that obtained by pendulums in the horizontal direction. Note that the lowest natural frequencies of the IP and GAS filters are limited by hystheretic behaviors of elastic components and thus can be potentially improved by investigating better elastic material in the future.

SAS is basically a passive system and thus has advantages in robustness and ease of maintainance once it is installed. Nevertheless the system cannot be completely passive and active controls are required for compensating thermal drift and damping the mechanical resonances.

3.2 Inverted pendulum

3.2.1 Basic working principle

An Inverted Pendulum (IP) is a horizontal mechanical oscillator whose resonant frequency is tunable and can be reduced lower than 0.1 Hz. It provides seismic attenuation at the microseismic peak frequency (0.2-0.5 Hz) by one order of magnitude and horizontal mobility of the suspended platform in soft manners. A simple model of the IP is shown in figure 3.1. The IP consists of a flexure fixed to the ground, a rigid cylindrical leg connected onto it and a mass on the top of the leg. When the mass is displaced horizontally from the vertical point, a restoring force acts on it with an effective spring constant of

$$k_{\text{eff}} = \frac{k_\theta}{L^2} - \frac{Mg}{L}. \tag{3.1}$$

k_θ is the bending spring constant of the flexure (the torque induced by unit bending angle), M is the mass of the payload and L is the length of the leg. Here the mass of the leg m is assumed to be negligibly small, i.e. $m \ll M$. The first term of k_{eff} corresponds to the elastic restoring force of the flexure and the rest represents a repulsive force with gravitational anti-spring effect. The effective stiffness of the IP decreases as the mass of the payload increases and it bunishes when the mass reaches $M_{\text{c}} = k_\theta/gL$. This mass is called the critical mass. Within the stable region ($M < M_{\text{c}}$) the resonant frequency of the IP is expressed as

$$\omega_{\text{IP}} = \sqrt{\frac{g}{L}\left(\frac{M_{\text{c}} - M}{M}\right)}. \tag{3.2}$$

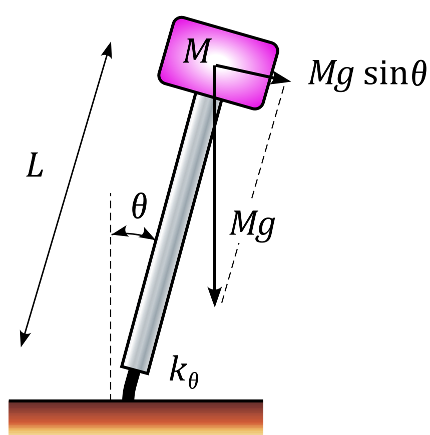

Figure 3.1: An illustration of the IP.

3.2.2 Anelasticity and quality factors

In the case of real IPs, inelastic damping effect due to the internal friction of the flexure must be taken into account. Introducing an imaginary part with an intrinsic loss angle ϕ to the flexure spring constant, the effective spring constant becomes

$$k'_{\text{eff}} = \frac{k_\theta}{L^2} \times (1 + i\phi) - \frac{Mg}{L}. \tag{3.3}$$

One can define the effective loss angle of the system as

$$\phi_{\text{eff}} = \frac{k_\theta}{L^2 k_{\text{eff}}}\phi. \tag{3.4}$$

The quality factor of the IP resonance decreases as the effective spring constant is reduced by gravitational anti-spring effect. This is an important and useful property of the IP, because an IP tuned at sufficiently low frequency needs no external damping. Figure 3.2 shows the measured quality factor with the resonant frequnecy of the IP which has been developed for LIGO [51]. The downside of this loss mechanism is that when the IP is tuned at extremely low frequency and the quality factor approaches to $Q \sim 1$, the IP shows hysteretic behaviors and instablity. Therefore in most cases the IP is tuned at not lower than 30 mHz when it is used as a seismic isolator in gravitational wave detectors. This practically limits the seismic attenuation at very low frequencies with IPs.

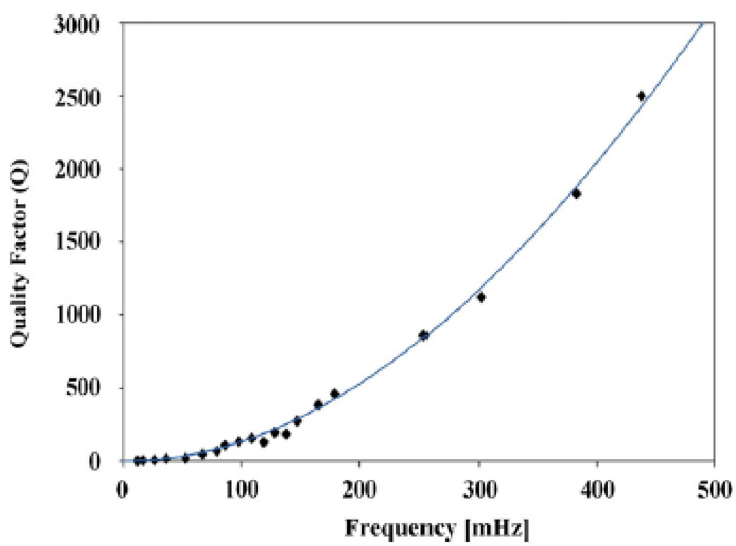

Figure 3.2: Measured quality factor versus resonant frequency of the HAM-SAS IP developed for LIGO [51].

3.2.3 Attenuation performance

Considering the frequence response of the IP to the ground motion, one has to take into account the mass distribution of the IP leg. Assuming that the leg has uniform mass distribution between the flexure and the payload with total mass of m and moment of inertia of I, the trasnfer function from the ground displacement to the payload displacement is written as [50]

$$H_{\mathrm{IP}}(\omega) = \frac{A + B\omega^2}{A - \omega^2}, \tag{3.5}$$

$$\text{where} \quad A = \frac{k_{\mathrm{eff}}}{M + \frac{m}{4} + \frac{I}{L^2}}, \quad B = \frac{\frac{m}{4} - \frac{I}{L^2}}{M + \frac{m}{4} + \frac{I}{L^2}}. \tag{3.6}$$

Figure 3.3 shows the amplitude of $H_{\mathrm{IP}}(\omega)$ as a function of frequency. The attenuation ratio saturates at high frequencies due to the coefficient B in equation (3.5). This behavior is physically related to the Center of Percussion (CoP) effect [52, 50]. The IP legs should be made as light as possible to minimize the CoP effect and improve the attenuation performance at high frequencies. In order to further compensate the CoP effect, the mass distribution of the leg can be changed by introducing a counter weight at the bottom of the leg (figure 3.4).

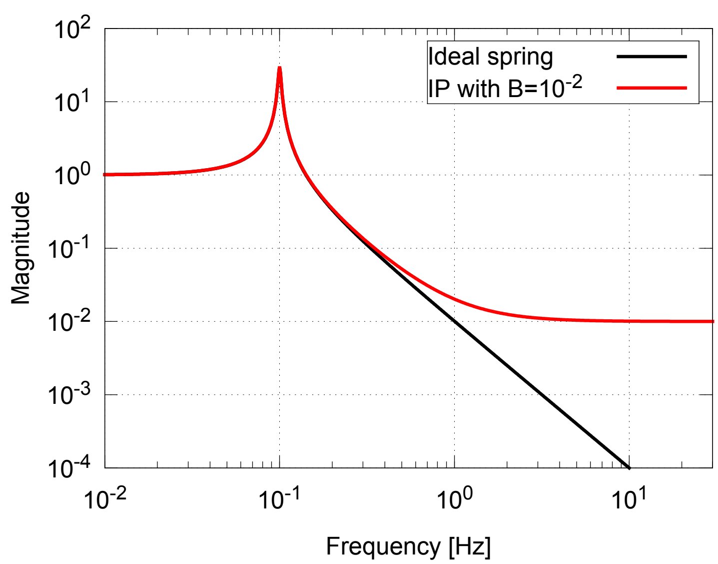

Figure 3.3: The transfer function of an IP with the resonant frequnecy of 0.1 Hz and the saturation level of 10^{-2}. The measurement data fit with a quadratic function.

The IP of the HAM-SAS developed for advanced LIGO [53] has an aluminum pipe with 1 mm thickness and 50 cm length as a leg. With the aid of the lightness of the leg ($m \sim 0.2$ kg), the attenuation performance reaches $\sim 10^{-3}$ without couter weights and 10^{-5}-10^{-4} with them.

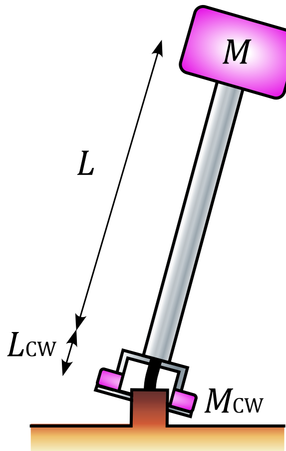

Figure 3.4: An illustration of the IP with the counter weight mounted at the bottom of the leg.

3.2.4 Horizontal modes of IP-stage

In the Seismic Attenuation System for gravitational wave detectors, IPs are used in the primary isolation stage, which provides pre-isolation of seismic vibration in horizontal directions with a platform supported by three IP legs. Neglecting the vertical elasticity of the IP legs, the platform has three normal modes with two translation and one rotation DoFs. A model of the isolation platform is illustrated in figure 3.6. There is a round rigid-body platform connected to three horizontal springs, which correspond to the IPs with effective spring constants of k_1, k_2 and k_3. The IPs are arragend in a distance of R from the central point and seperated by 120° with each other. The motion of the rigid-body is characterized by a vector defined by the position and rotation angle $(x, y, R\phi)$ in the Cartesian coordinate system. By giving a small perturbation in each degree of freedom, one obtains the following stiffness matrix of the system:

$$K = \begin{bmatrix} k_1 + k_2 + k_3 & 0 & \frac{\sqrt{3}}{2}(-k_2 + k_3) \\ 0 & k_1 + k_2 + k_3 & \frac{1}{2}(2k_1 - k_2 - k_3) \\ \frac{\sqrt{3}}{2}(-k_2 + k_3) & \frac{1}{2}(2k_1 - k_2 - k_3) & k_1 + k_2 + k_3 \end{bmatrix}. \tag{3.7}$$

In the symmetric system with $k_1 = k_2 = k_3$, the non-diagonal elements of the stiffness matrix diminish and the eigen modes are seperated into pure translation modes in the x, y directions and a rotation mode about ϕ. In actual system, there exists asymmetry in the effective stiffness and thus translation and rotation modes are coupled with each other.

3.2.5 Response to ground tilt

When the ground tilts by an angle of θ, it introduces additional force of $\frac{k_\theta \theta}{L}$ to the suspended payload. The transfer function from the ground tilt to the induced payload

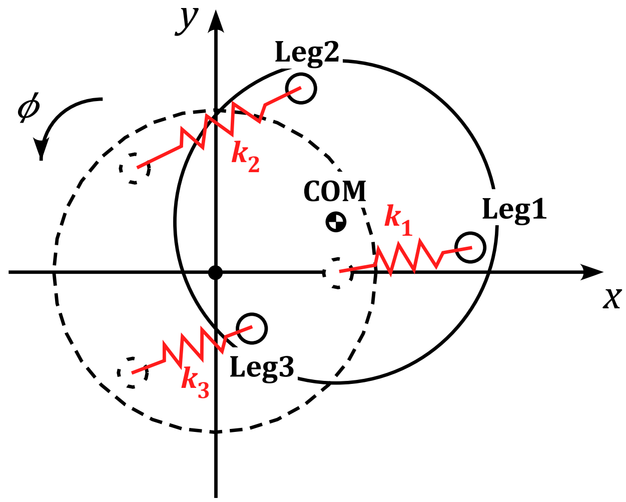

Figure 3.5: A rigid-body model of the isolation platform with three IP legs.

displacement is then described as

$$H_{\mathrm{IP,tilt}}(\omega) = \frac{AC}{A-\omega^2},, \quad \text{where} \quad C = \frac{k_\theta}{Lk_{\mathrm{eff}}}. \tag{3.8}$$

In the low frequency limit, the transfer function approaches C. The coupling coeffcient increases as the effective spring constant k_{eff} is reduced by gravitational anti-spring effect. This means the system with lower resonant frequency gets more sensitive to the DC ground tilt. The DC tilt of the IP support strcture may reach 10^{-5} rad, which would be induced by crustal movement of the earth, human activities around the system and thermal deformation of the structure. It would induce the payload displacement of sub-millimeters and thus should be compensated by active control systems.

In the isolation platform supported by multiple IP legs, couplings by the ground tilt at high frequencies would be dominated by contribution from the rigid-body motion of the platform. Since the IP legs are rigid in the vertical direction, the ground tilt induces the tilt of the platform in the same rotation angle. When the measurement point is vertically seperated from the center of platform rotation by a distance of d, the rotation angle θ directly couples to the displacement at the measurement point by $d\theta$. Therefore the transfer function from the ground tilt is revised as

$$H_{\mathrm{IP,tilt}}(\omega) = \frac{AC}{A-\omega^2} + d \tag{3.9}$$

in the frequency region where the IP legs and the payload can be regarded as rigid bodies. Figure 3.7 shows the amplitude of the transfer function with the coupling coefficient of $C = 30$ m/rad and $d = 50$ mm.

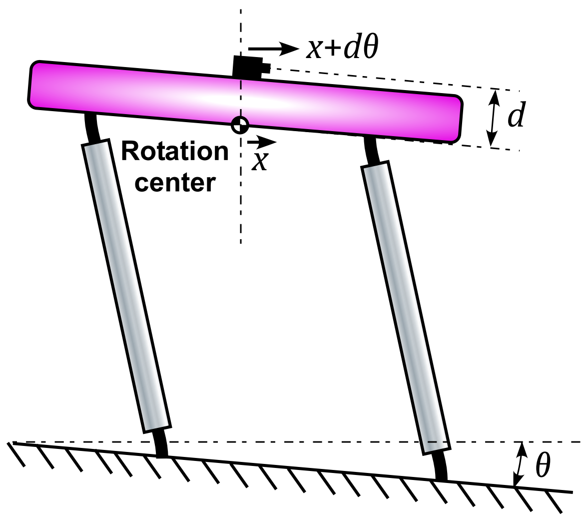

Figure 3.6: Ground tilt coupling through rigid-body motion of the platform.

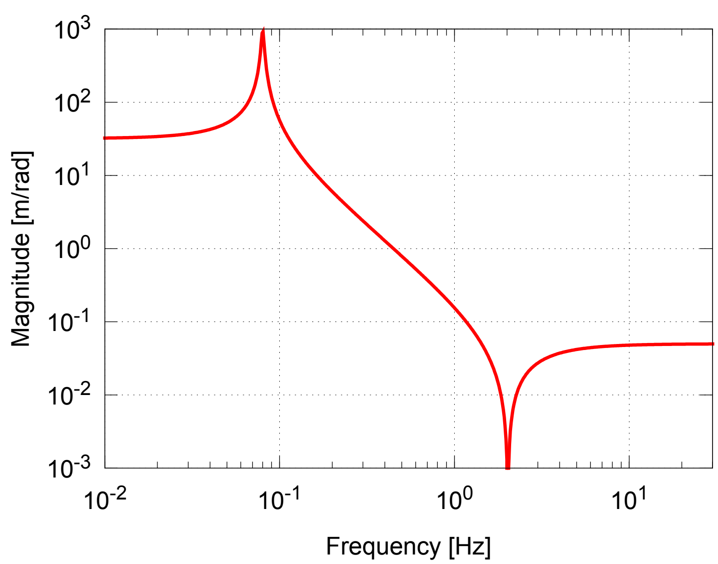

Figure 3.7: Expected ground tilt coupling of the IP as a function of frequency, assuming $C = 30$ m/rad and $d = 50$ mm.

3.3 Geometric Anti-Spring (GAS) Filter

3.3.1 Low-frequency vertical isolator

One of the major difficulties in designing vibration isolation systems for gravitational wave detecotrs is to achive vertical attenuation performance comparable to that obtainable in the horizontal direction. For achiving low frequency seismic isolation one needs to implement soft springs, while at the same time the sprigns must support the weight of the suspended payload.

One solution to the problem is based on magnetic anti-spring technology [48], which has been implemented in the superattenuator for the Virgo detector. It utilizes permanent magnets faced each other in a horizontal plane with the same magnetic pole. These magnets produce a repulsive force and it transmits to the vertical direction as they are displaced vertically. This replusive force works as an anti-spring force and reduces the effective stiffness of the vertical spring. A drawback of using the technology is that the resonant frequency fluctuates by temperature shift, since the magnetic field strength strongly depends on the temperture. Also the additional components such as permanent magnets and centering devices induce unwanted mechanical resonaces around few tens of Hz, which degradate the attenuation performance in the detection band of gravitational waves.

A considerable improvement of the magnetic anti-spring is the Geometric Anti-Spring (GAS) technique [54], which allows increases of attenuation performance, thermal stabilty and simpleness of the mechanics. This section briefly explains the working mechanism and expected mechanical properties of the vertical isolator with GAS technology, called the GAS filter.

3.3.2 Basic working principle

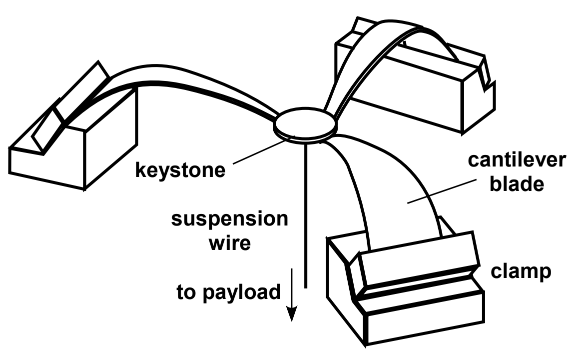

Figure 3.8: A schematic drawing of the GAS filter.

The GAS filter consists of a set of radially-arranged cantilever blades clamped on the base frame and to the central disk called the keystone. (figure 3.8). The blades are flat when they are manufactured and bend like fishing rods when they are loaded. The working principle of the GAS filter is mathematically described in reference [54], while its behavior can be understood by means of a simple analytical model shown in figure 3.9. In this model, a cantilever spring is represented as a combination of vertical and horizontal linear springs. Due to the symmetry of the system, one can simplify the model to a single blade model with the constraint that the tip of the blade moves only along the vertical axis.

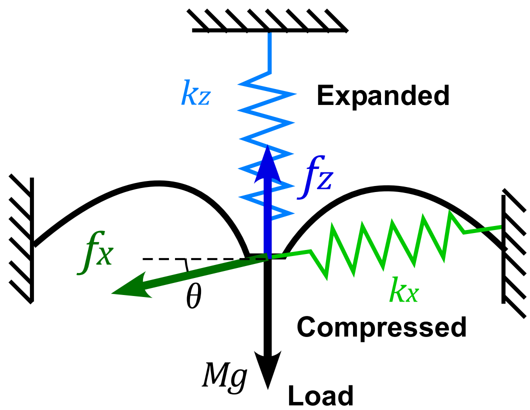

Figure 3.9: An analytical model of the GAS filter.

The payload of mass M is suspended by a vertical spring of elastic constant k_z and a horizontal spring of elastic constant k_x. The angle formed by the horizontal spring and the horizontal axis θ is zero when the tip of the blade is at the equilibrium position ($z = z_{\text{eq}}$). Then the equation of motion in the vertical axis is written as

$$M\ddot{z} = -k_z(z - z_{\text{eq}}) - k_x(l - l_{0x})\sin\theta, \tag{3.10}$$

where l is the actual length of the horizontal spring and l_{0x} is its natural length. Expanding the equation of motion around the working point z_{eq} to the first order of z, one obtains the following linearized equation of motion:

$$M\ddot{z} = -\left[k_z - \left(\frac{l_{0x}}{x_0} - 1\right)k_x\right](z - z_{\text{eq}}) = -k_{\text{eff}}(z - z_{\text{eq}}). \tag{3.11}$$

Here x_0 is the horizontal distance between the central keystone and the support point of the horizontal spring. When the horizontal spring is under compression ($x_0 < l_{0x}$), it causes a repulsive force in the vertical direction and therefore the effective spring constant is reduced from the spring constant of the vertical spring ($k_{\text{eff}} < k_y$). This is the principle of the anti-spring effect in the GAS springs. The name of Geometric Anti-Spring stands for the fact that the anti-spring is realized by a specific geometry of the cantilever blade. The effective stiffness and the resonant frequency can be reduced by increasing the compression of the blades (decreasing x_0).

3.3.3 Quality factor

When the GAS filter is tuned toward lower resonant frequencies, its quality factor decreases progressively, as observed in the IP. Figure 3.10 shows measurement results of the quality factor versus resonant frequency of the GAS filters [55]. In contrast to the quality factor of the IP, the measurement data do not show quadratic behavior with the structural damping model. This indicates contribution of other damping mechanisms such as thermoelastic damping. One possible explanation of the behavior by the Self Organized Criticality (SOC) of the dislocation can be found in reference [56].

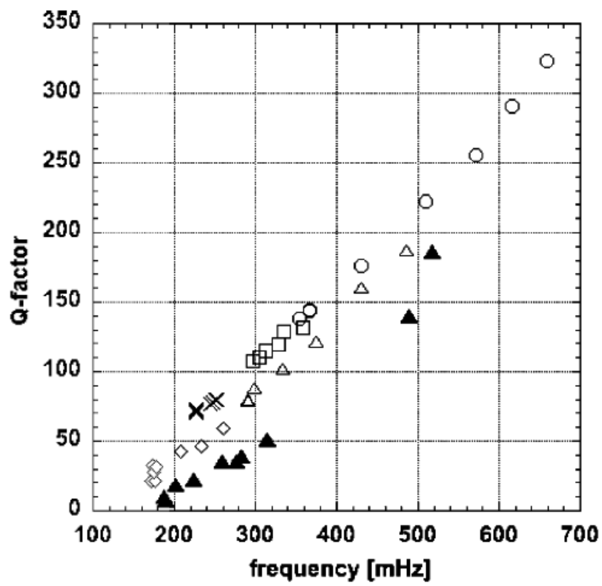

Figure 3.10: The measured quality factor versus resonant frequency of the GAS filters [55].

3.3.4 Attenuation performance

The transfer function of the GAS filter from the vertical displacement of the frame to that of the keystone is written in the same form as that of the IP, equation (3.5). Due to the CoP effect, the attenuation performance saturates at high frequencies and is typically limited to $\sim 10^{-3}$ (see figure 3.11). It can be compensated by adding a wand with a counter weight in parallel to the blades, so-called the magic wand (figure 3.12), which allows to improve the attenuation level down to 10^{-4}. [57].

3.3.5 Thermal drift

The GAS filter achives siginificant softness by balancing the anti-spring effect by horizontal compressive force and intrinsic vertical stiffness of the cantilever blade. Due to the softness, the vertical position of the keystone moves easily by a small change of the

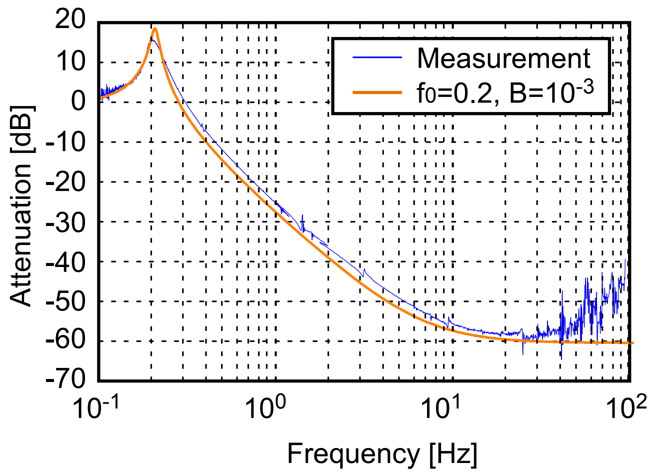

Figure 3.11: Attenuation performance of the GAS filter without the magic wand [57].

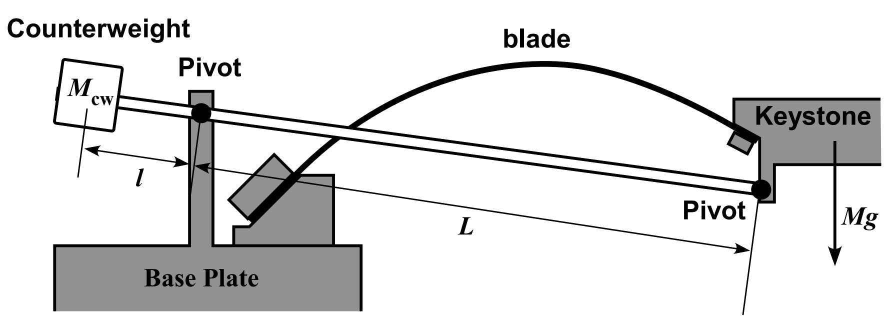

Figure 3.12: The magic wand used to compensate the CoP effect.

payload mass and the blade springs' physical properties. Especially the thermal drift due to the temperature dependence of the Young's modulus of the spring material is a big issue in operating the GAS filter. Assume that the GAS filter is balanced at the working point with the payload mass of M, the optimal load to keep the keystone in the working point is shifted with the temperature change by:

$$\Delta M \approx \frac{M}{E}\frac{\partial E}{\partial T}\Delta T. \tag{3.12}$$

Here E is the Young's modulus of the spring material and ΔT is the shift of the temperature. In a small perturbation, this change is equivalent to an additional force applied to the keystone by $\Delta F = \Delta M g$. Since the system has an effective spring constant of k_{eff}, the displacement caused by thermal shift is calculated as

$$\Delta z = \frac{\Delta F}{k_{\mathrm{eff}}} = \frac{g}{E\omega_0^2}\frac{\partial E}{\partial T}\Delta T. \tag{3.13}$$

Here the resonant frequency of the GAS filter is tuned at ω_0 and thus the effective spring constant is written as $k_{\mathrm{eff}} = M\omega_0^2$. The system gets more sensitive to the temperature change as the resonant frequency is reduced by anti-spring effect. By the use of typical parameters, the temperature dependence is calculated as

$$\frac{\Delta z}{\Delta T} = 0.83\ [\mathrm{mm/K}]\ \left(\frac{2\pi \times 0.3\ \mathrm{Hz}}{\omega_0}\right)^2 \left(\frac{\frac{1}{E}\frac{\partial E}{\partial T}}{3.0\times 10^{-4}\ [1/\mathrm{K}]}\right). \tag{3.14}$$

3.4 Developed Seismic Attenuation Systems

3.4.1 Various SASs for gravitationoal wave detectors

The SAS technology has been adopted to several vibration isolation systems for gravitational wave detectors, such as HAM-SAS developed for advanced LIGO [53], AEI-SAS for 10-m prototype detector in Hannover [?], EIB-SAS and Multi-SAS for advanced Virgo [58]. A visual impression of one of the systems is shown in figure ??. They are designed to provide seismic attenuation for optical benches which various optics for the interferometers are fixed to or suspended from. They basically provide 1-2 stages of seismic attenuation for all six DoFs of the bench rigid-body motions, with attenuation factors of 10^{-2}-10^{-6} in the detection band of gravitational waves.

The SAS aiming for directly suspending the core optics of the interferometer is developed in TAMA and called the TAMA-SAS [50]. A schematic drawing of the TAMA-SAS is shown in figure 3.14. The TAMA-SAS provides 5-stage attnuation (including the IP stage) for the horizontal motions and 3-stage attenuation for the vertical motions to the suspended optic. The top stage supported by three IPs is actively controlled by using position sensors and accelerometers. The internal modes of the suspension system is passively damped by the use of an eddy-current damper implemented just above the optic.

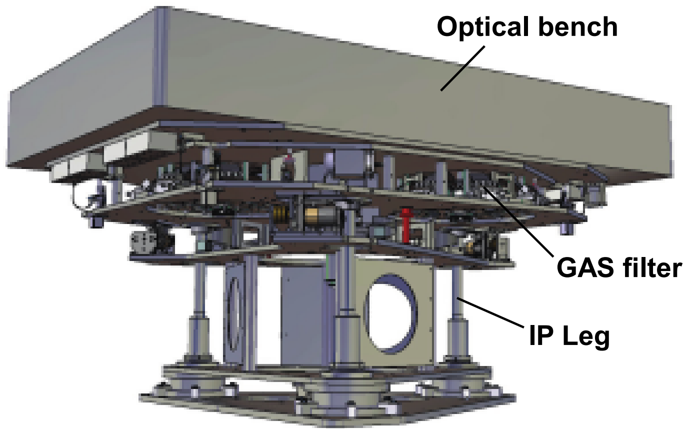

Figure 3.13: A visual impression of the EIB-SAS developed for advanced Virgo [59].

The TAMA-SAS should provide enough seismic attenuation performance at 10 Hz so that the contribution from seismic noise gets much less than that from other fundamental noise sources.

3.4.2 Interferometer operation with TAMA-SAS

The vibration isolation systems for TAMA were replaced from conventional vibration isolation stacks to TAMA-SAS, and the interferometer started its operation with TAMA-

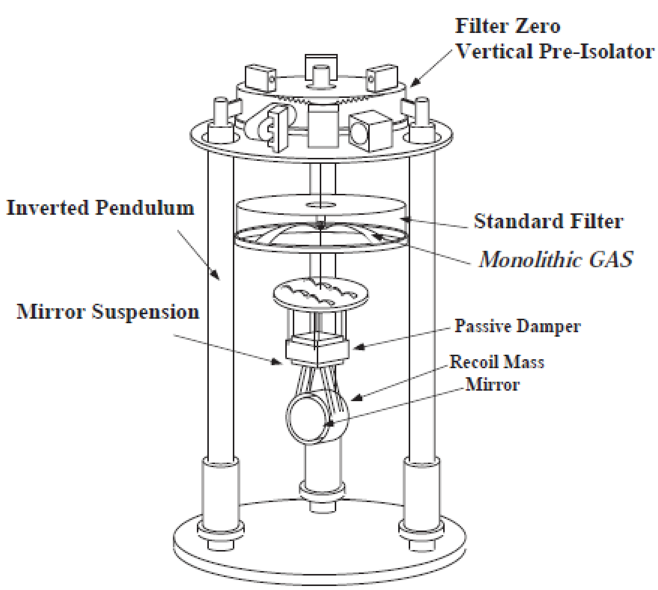

Figure 3.14: A schematic drawing of the TAMA-SAS [50].

SAS from 2006. Figure 3.15 shows the achieved displacement noise level of the detector and the noise budget. The noise level below 200 Hz was improved by introducing TAMA-SAS, owing to reduced alignment control noise of the interferometer. This was achieved by reduction of angular motion of the test mass in the 1-10 Hz band.

Although the noise level was improved by introducing SAS, the detector sensitivity of TAMA is still limited by practical noises rather than fundamental noises such as thermal noise and quantum noise. The main contribution in the 100-500 Hz band comes from upconversion noise, which is induced by feedback forces applied on the mirrors in a low frequency band ($<$ 1 Hz). The noise is expected to be related with acoustic noise emission from Nd-Fe-B magnets attached on the mirrors, due to discontinuous jumps of the magnetization (Barkhausen effect [60]). The alignment control noise limits the sensitivity below 100 Hz and further reduction of control bandwidth is required to expand the detection band of gravitational waves down to $\sim$10 Hz. The observation in TAMA indicates that it is mandatory to reduce low frequency fluctuation of the mirror displacements and angles with appropriate control loops. The attenuation performance of SAS is otherwise spoiled by control noise couplings and upconversion noise.

Another learning from the operation of TAMA-SAS was that one has to make sure that all the low-frequency resonances existing in the system are appropriately damped by passive/active damping mechanisms. In case of TAMA, the operation of the interferometer was often disturbed by large-angle rotation of the suspended optics around the vertical axis, which arises through excitation of the torsion modes of the suspension wires. Since the GAS filters and the lower stages are connected through single-wire suspensions, they form a multi-stage torsion pendulum with significantly low resonant frequencies ($\sim$ 10 mHz). The torsion modes have long decay time (in the order of 10^3-10^4 sec) unless they are appropriately damped. Thence TAMA-SAS afterwards introduced motion sensors to detect the torsion modes and actively damp them, as illustrated in figure 3.16 [61].

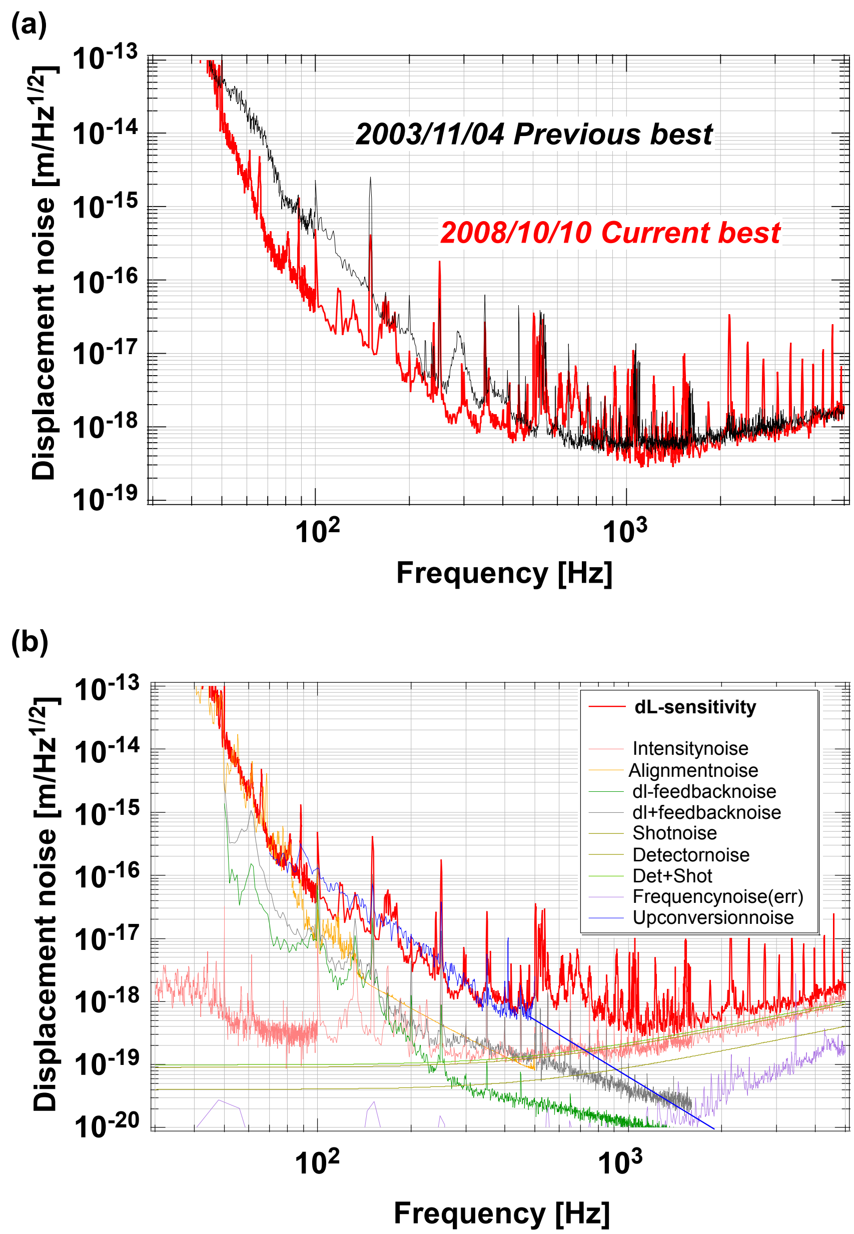

Figure 3.15: (a) Comparison of the detector sensitivity before and after the TAMA-SAS installation. (b) Noise budget of the interferometer with TAMA-SAS [?].

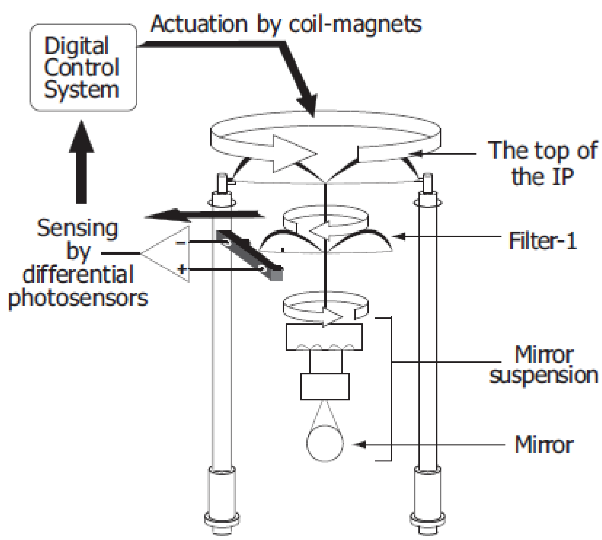

Figure 3.16: A conceptual diagram of the torsion mode damping system for TAMA-SAS [61].

Seismic Attenuation in KAGRA

Chapter 4

The previous section introduces the general concept of SAS and basic working principles of the mechanical components. This section forcuses on SAS developed for KAGRA, the Japanese second generation detector. As described in chapter 1, the second generation detectors aim for expanding the detection band of gravitational waves toward ∼10 Hz in the low frequency region. To achieve this goal, KAGRA employ SAS technologies for core optics vibration isolation, based on the studies obtained in the TAMA-SAS operation. This chapter describes conceptual design of KAGRA-SAS, mechanical simulations for verifying the performance and some detailed design of mechanical components.

Section 4.1 checks out the requirement on seismic attenuation performance for core optics of the KAGRA interferometer. Section **??** describes conceptual design of SAS for each core optic. In section **??**, mechanical simulations with rigid-body models are set out to verify the seismic attenuation performance.

4.1 Basic requirement

4.1.1 General consideration

Seimic isolation systems for the core optics of the interferometric gravitational wave detectors must possess the following features in general:

- Passive attenuation capability to suppress the seismic noise level well below the gravitational wave signal level or other noise levels in the detection band of gravitational waves.

- Capability of suppressing the RMS velocity/displacement of the suspended optics, which are typically concentrated at low frequencies below 1 Hz, for fast lock acquisition and stable operation of the interferometer.

- Active/passive damping capability of low-frequency mechanical resonances for fast recovery from unwanted excitation states.

- Sufficeint actuation range of the suspended optics in several DoFs to allow lock acquistion, alignment tuning and beam spot optimization of the interferometer.
- Stability of the mechanics and active components to allow long-term observation of gravitational waves.
- Ultra-High Vacuum (UHV) compatibility so as not to contaminate the detector sensitivity through the residual gas noise.

This section mainly discusses the in-band requirement of the seismic attenuation performance at frequencies above ~ 10 Hz. The out-band requirement below 10 Hz affecting RMS displacement/velocity, damping capability and mobility of the optics will be further discussed in chepter **??**.

4.1.2 Displacement noise requirement

As described in section 1.4, the second generation detectors employ dual-recycled Fabry-Perot Michelson interferometers for enhancing and optimizing the detector sensitivities. Differential length variation of the arm cavities (so-called DARM) contains gravitational wave signals and thus it is the most important DoF in the gravitational wave detectors. Since displacement noise of the test masses directly couples to the DARM signals, they have the strictest requirement on the displacement noise. Displacement noise of auxiliary optics also affects the detector sensitivity due to the couplings in the length sensing and control schemes of the interferometer [62], but to a much lower extent than the test masses.

Besides the seismic noise, the sensitivity of the interferometer is fundamentally limited by the thermal noise and the quantum noise (see figure 1.8). The goal of the vibration isolation system is suppressing the seismic noise level well below these noise levels in the detection band of gravitational waves. More specifically, the requirement for the seismic noise level is to be lower by a factor of 10 in amplitude spectrum densities than other noise levels in the frequency region above 10 Hz. Required displacement noise level of the core optcs of the KAGRA interferometer in two different detection modes is shown in figure 4.1 [63]. KAGRA has two optional detection modes called BRSE (Broadband Resonant Sideband Extraction) and DRSE (Detuned Resonant Sideband Extraction) [32]. These two modes can be switched by changing the resonant condition of the signal recycling cavity. The DRSE mode has better sensitivity around 100 Hz, aiming for detecting gravitational waves from binary neutron stars, while it spoils the sensitivity in the high frequency region.

The maximum permitted displacement noise level at 10 Hz is summarized in table 4.1. It takes lower values of the displacement noise required in the two detection modes. The auxiliary optics are allowed to have larger displacement noise than test masses, by a factor of $\sim 10^2$ for the beam splitter and signal recyclers, and by a factor of $\sim 10^4$ for the power recyclers. Folding mirrors for the power/signal recycling cavity have stricter requirement than PRM/SRM, since their longitudinal displacement alters the cavity length by twice of the distance.

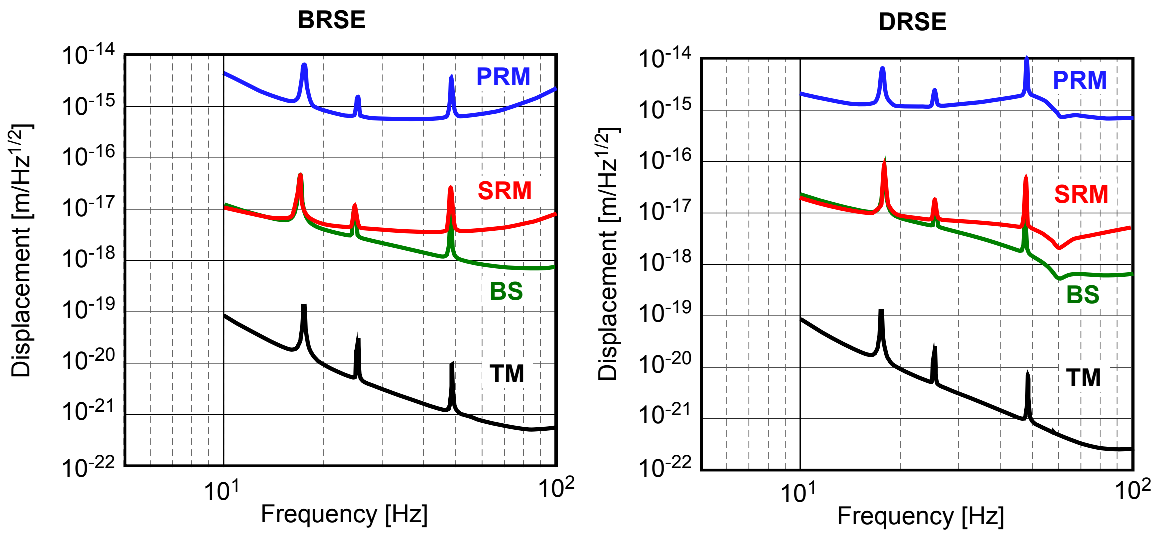

Figure 4.1: Longitudinal displacement noise requirements on core optics of the KAGRA interferometer, in two different detection modes. [63].

	spectrum density at 10 Hz
TM	1×10^{-19} m/$\sqrt{\text{Hz}}$
BS	1×10^{-17} m/$\sqrt{\text{Hz}}$
PRM	2×10^{-15} m/$\sqrt{\text{Hz}}$
PR2, PR3	1×10^{-15} m/$\sqrt{\text{Hz}}$
SRM	1×10^{-17} m/$\sqrt{\text{Hz}}$
SR2, SR3	5×10^{-18} m/$\sqrt{\text{Hz}}$

Table 4.1: Requirement on longitudinal displacement noise of the core optics for the KAGRA interferometer.

As described in chapter 2, 0.1-1% of the vertical motion is transferred to the longitudinal direction by mechanical cross-couplings, therefore vertical seismic attenuation is also required. Even without mechanical couplings, the vertical motion is coupled to the longitudinal direction at least by 0.3% in the KAGRA detector. This coupling comes from the fact that the KAGRA interferometer is not constructed in the horizontal plane for a practical reason. As there are many groundwater sources in the Kamioka mine (site of the KAGRA detector), one needs to flow the water outside the tunnel and therefore the interferometers is constructed in a tunnel with a tilt of 1/300. Here in the following investigation, vertical-horizontal coupling of 1% is assumed.

4.1.3 Seismic vibration in the Kamioka mine

KAGRA features in the underground environment with significantly low seismic vibration as described in section 2.1. The seismic vibration in the Kamioka mine has been monitored in a long term as a joint research of Disaster Prevention Research Institute and Cryogenic Laser Interferometer Observatory (CLIO) [64] Project. Analysis of the 1.5-year (2009.9-2011.2) data of ambient seism motion, taken by a Güralp CMG-3T seismometer located at the CLIO site, obtains the following noise spectrum models shown in figure 4.2.

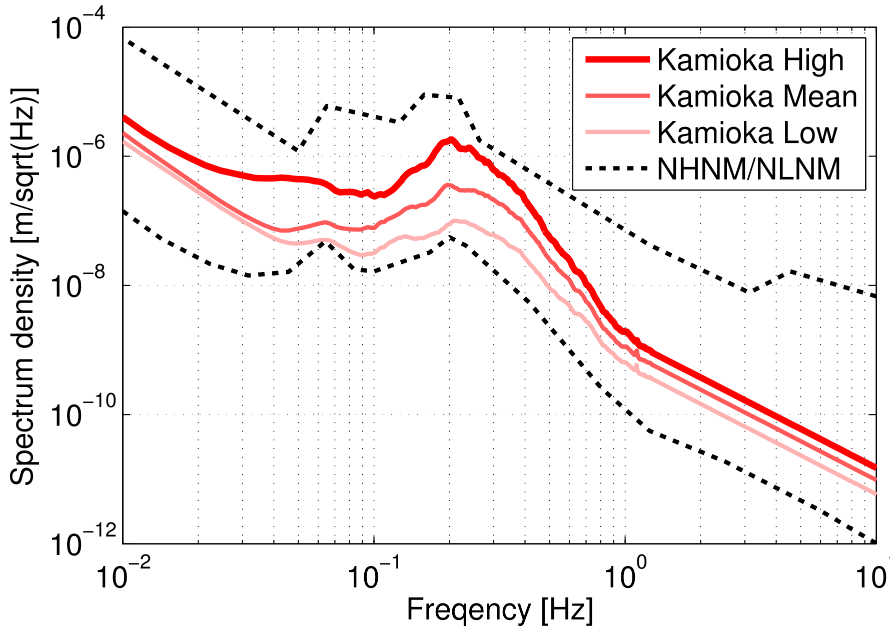

Figure 4.2: Seismic vibration spectrum of the Kamioka site.

The plots below 1 Hz shows measured seismic spectra in 10, 50 and 90 percentile levels and the spectra above 1 Hz are fit curves proportional to f^{-2}. The seismic spectrum around the microseismic peak widely spreads in magnitude, since the amplitude highly dependes on the oceanic activities and thus on the weather conditions. The RMS displacement of the seismic motion (integrated down to 10^{-2} Hz) varies from 0.08 to 0.5 μm, in the 10-90 percentile range. Although CMG-3T is not sensitive enough to measure the seismic vibration of the Kamioka site in the high frequency region above 1 Hz, another measurement set out with a Trillium 240 seismometer confirms the displacement spectrum in proportional to f^{-2} at high frequencies. More details on the analysis of the seismic spectrum measurement in the Kamioka mine will be described in Appendix **??**. In the following investigation, one assumes the high noise model in figure 4.2 as seismic vibration injected to the seismic attenuation systems.

Since the seismic vibration level of the Kamioka site is $\sim 10^{-11}$ [m/$\sqrt{\mathrm{Hz}}$] at 10 Hz, required attenuation ratio at this frequency is 10^{-8} for the test masses, 10^{-6} for the beam splitter and signal recycling mirrors, and 10^{-4} for the power recycling mirrors.

4.2 System Overview

4.2.1 Conceptual design

To meet the requirements described above, KAGRA employs several types of suspension systems for the core optics depending on the required seismic attenuation levels. The conceptual designs of three types of KAGRA-SAS are illustrated in figure 4.3 and their disposition is shown in figure 4.4. Table 4.2 shows their basic specifications. The suspension system can be divided into three separated parts:

1. The pre-isolation and static-control stage at the top of the chain.

2. The chain of mechanical filters to achieve the required seismic attenuation.

3. The mirror suspension providing control forces for lock acquisition and alignment.

The largest suspension system, so-called the type-A SAS, provide 8-9 stages of horizontal attenuation and 6 stages of vertical attenuation for the test masses. To take an advantage of the underground environment, the type-A SAS is constructed in a bilayer tunnel and the base of the suspension system sits directly on the upper floor. The IP stage located at the top of the chain provides pre-isolation and static-control of the whole

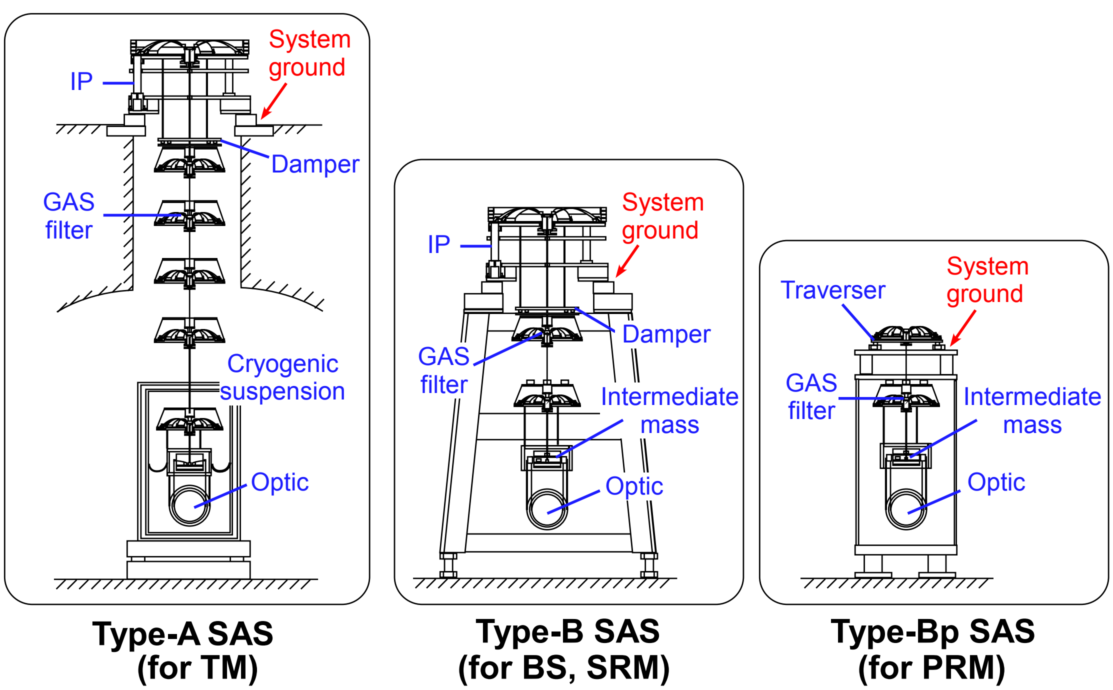

Figure 4.3: Conceptual designs of KAGRA-SAS. Their vacuum envelopes are not illustrated for simplicity.

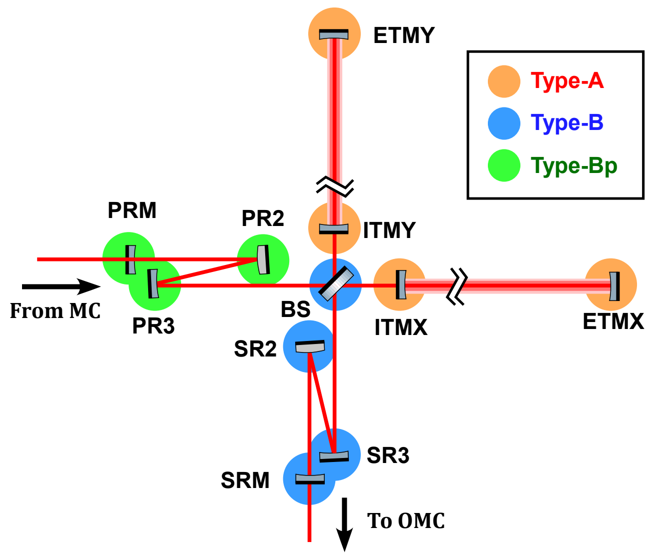

Figure 4.4: Disposition of SAS in the KAGRA main interferometer.

suspension system. The attenuation chain resides inside a borehole of 1.2 m diameter and connected to the mirror suspension located in the lower tunnel. Several attenuation stages around the optic are cooled down into cryogenic temperature for thermal noise reduction. The cryogenic part is coverred with aluminum boxes to shield black-body radiation from room temperature components.

The type-B SAS, used for seismic islation of BS and signal recycling mirrors, has smaller number of attenuation stages and a room temperature payload. The base of the suspension sytem sits on an external support frame enveloping the attenuation chain. The support frame is supposed to be a rigid structure and transmit the seismic vibration to the suspension system straightforwardly, but in practice it has unavoidable mechanical resonances and thus enhances the vibration injected to the suspension system. The type-B SAS also has the IP stage for pre-islatoion and static-control of the suspension chain. Three stages of GAS filters provide vertical seismic attenuation in the detection frequency band of gravitational waves. The optic is suspended from the upper stage called the intermediate mass by two-loops of wires. It works as a marionette and the alignment of the optic can be adjusted through rotating the intermediate mass.

	Type-A	Type-B	Type-Bp
suspended optics	TM	BS, SRM, SR2, SR3	PRM, PR2, PR3
horizontal stage #	8-9 (include IP)	5 (include IP)	3
vertical stage #	6	3	2
payload temperature	cryogenic (< 20 K)	room-temperature	room-temperature

Table 4.2: Basic specification of three types of KAGRA-SAS.

The type-Bp SAS is a reduced version of the type-B SAS and employed to the optics for the power recycling cavity. Although the power recycling mirrors were planned to employ type-B SAS in the preliminary design of the KAGRA detector, their suspension systems were reduced due to budgetary constrains. The type-Bp system does not contain the preisolation stage with IP and have only two stages of GAS filters for veritcal isolation. In order to control the horizontal static position of the suspended optic, a motorized stage called the traverser is implemented on the top of the chain. This system however does not provide pre-isolation of horizontal vibration in contrast to the IP stage, and thus the suspended optics are expected suffer from large RMS displacement/velocity.

4.2.2 IP stage

This stage is in charge of seismic attenuation starting from $f \sim 0.1$ Hz and static-control of the suspension point position and yaw orientation of the chain. Figure 4.5 shows the schematic design of the pre-isolator. The stage is supported from the ground or the support structure by three Inverted Pendulums (IPs), which provide seismic attenuation in the horizontal plane. At the top of the stage, there is a large Geometric Anti-Spring (GAS) filter for vertical seismic attenuation. It is twice as large in diameter as the standard GAS filter used in the attenuation chain, and called the top filter. In order to achieve seismic attenuation at the microseismic peak (100-300 mHz) and reduce the RMS amplitude of the mirror displacement, the IPs and top filters will be tuned at resonant frequencies lower than 100 mHz. The working principle of the IP and GAS filter will be explained in the next section.

The horizontal motion of the stage will be controlled by the use of three single-axis accelerometers [65], three Linear Variable Differential Transformer (LVDT) position sensors [66] which measure the relative motion of the stage with respect to an external frame fixed to the ground, and three coil-magnet actuators [67]. The design of the control system is essentially the same as developed for and used in TAMA-SAS and Virgo [68, 69].

Standard GAS Filter

In order to achieve required seismic attenuation both in horizontal and vertical directions, a chain of standard GAS filters will be suspended from the pre-isolation stage. Each GAS filter is suspended by a single wire, and its suspension points are placed nearby its center of mass (Figure 4.6). In this configuration, the motion of the filter is attenuated in every translational and rotational DoF. The cantilever blades and the suspension wires are made of maraging steel [70], which has particularly good creep characteristic [71].

Mirror Suspension System (Payload)

This part is located at the very bottom of the attenuation chain. It plays a role to precisely control the mirror position and orientation and provide additional seismic attenuation. As they hold directly the mirrors of the interferometer, suspensions must be

Figure 4.5: The 3D drawing of the pre-isolator.

Figure 4.6: The schematic design of the standard GAS filter

carefully designed so that they do not generate thermal noise or acoustic emission noise above the acceptable level.

Figure 4.7: The conceptual designs of the mirror suspension systems in type-A and type-B vibration isolation systems.

Figure 4.7 shows the conceptual designs of the suspension systems in type-A and type-B systems. In both cases, an intermediate mass is suspended by a single wire from the upper stage, and the mirror and its recoil mass are suspended from the intermediate mass by four wires each. The control force and torque are exerted onto mirrors from the coil-magnet actuators on its recoil mass. A recoil mass hanging from the bottom GAS filter is added to provide control actuation to the intermediate mass. A two level control is necessary because only very delicate forces can be applied on the mirror, while larger authority can be applied on the intermediate mass without fear of injecting excessive control noise. The concept of using a recoil mass (reaction mass) hung in parallel to the mirror suspension was introduced in Virgo last stage suspension system [72] and adopted in TAMA [73]. There are several technical advantages of using a recoil mass:

- The actuator is isolated from seismic disturbance, and therefore the fluctuation of the actuation efficiency due to the change of the relative position between the mirror and actuation mass is suppressed.

- The actuation on the mirror is isolated from the upper stages, because the reaction from the mirror and the recoil mass compensate each other at the intermediate stage. It simplifies the servo design for the mirror actuation.

The recoil mass for the intermediate mass is equipped with actuators and position sensors to control the motion of the intermediate mass. In type-B system, Optical Sensor and Electro-Magnetic actuator (OSEM) [74], which has been developed for advanced LIGO, will be used for the position sensing and actuation.

In type-A system, the suspension system is cooled down at cryogenic temperature to reduce the thermal noise. In order to transfer the heat absorbed in the mirror from the laser beams, the test mass is suspended by four sapphire fibers with 1.6 mm diameter and 30 cm length. The heat is transferred from the intermediate mass to the upper stage (platform), and then finally transferred to the inner shield of the cryostat via heat links made of pure aluminum. Since the heat link wires are mechanically connected to the cryostat, which is firmly fixed to the ground, extra vibration from the cryostat may be introduced to the suspension system through the heat links. This problem will be studied later.

Active suspension controls

Chapter 5

5.1 Motivation of active controls

Mechanics of suspension systems are designed so that they achieve sufficient vibration isolation in the frequency band of gravitational wave observation. On the other hand, the suspension systems also have to suppress the mirror vibration outside the band, for stable operation of the interferometer. Without any damping mechanisms, mirror vibration tends to be enhanced at low frequencies by mechanical resonces which typically possess high quality factors. Also, low frequency oscillators often suffer from thermal drifts or mechanical creeps, which blow the suspended mirrors away from the controllable range during the interferometer operation.

In order to suppress the low frequency vibration due to these mechanical characteristics, we control the vibration of mechanical components by the use of vibration sensors and actuators. Note that damping of mechanical resonances can be also achieved by passive dampers such as eddy-current dampers. Passive dampers are stable and easy of maintainance once they are installed to the suspension systems. Active control systems are rather delicate and we have to design the control servo carefully to operate them stably. On the other hand, active systems are more flexible and can be switched easily after installed to the suspension systems. We often need the flexiblity since different controls are required depending on the states of the interferometer and surrounding environment such as temperature and seismic vibration levels. This becomes a big motivation of using active control systems regardless of the complexity.

Another point we have to take care regarding active control systems is the control noise. Noises can be introduced by electronics of vibration sensors and actuators, and also by servos such as quantization errors in digital control systems. We have to make sure that the control noises do not contaminate the interferometer sensitivity any more than the required level.

5.2 Requirement on active controls

5.2.1 Interferometer phases and requirements

As mentioned in the previous section. there are different requirements on the active controls depending on the operation status of the interferometer. Here the operation status of the interferometer are categorized into three phases: the calm down phase, lock acquisition phase, and observation phase.

In the calm down phase, the suspension systems are under large disturbances and the mirrors are swinging in large amplitudes. In this phase, signals for some delicate sensors and week actuators for the active controls can saturate due to the large oscillation amplitude. One has to calm down the vibration using sensors and actuators with sufficient range, and set the position or orientation of masses back to the nominal places. Active controls in this phase require robustness rather than quietness. The fast we get back the suspension systems into working status, the more observation time we can acquire for gravitational wave observation. Thus decay times of the mechanical reosnances should be minimized in this phase for fast recovery.

In the lock acquisition phase, the mirrors in the interferometer are brought to their operation points to get ready for gravtitaional wave observation. For smooth lock acquisition of the interferometer, velocities of the mirrors have to be suppressed so that control forces can freeze their motion and trap them into the linear regime of the interferometer signals. Thence the active controls in this phase are required to minimize the velocities of the suspended mirrors. Typically the RMS velocities of the suspended mirrors have to be suppressed less than 1 μm/sec for smooth lock acquisition of optical cavities. Note that the RMS velocity of the ground vibration is roughly 1 μm/sec and the RMS velocities of the suspended mirrors tend to be enhanced by mechanical resonances with high Q factors. Damping controls for mechanical resonances are demanded, while we have to take care of control noises since they might enhance mirror velocities. The requirements on mirror velocities are discussed in details later.

After the lock acquisition achieved successfully, we get into the observation phase in which the interferometer is under operation and gravitational wave observation is taken in place. In this phase, silent controls are required so that the control noises do not contaminate the detector sensitivity in the observation frequency band ($>$ 10 Hz). Some noisy control loops should be opened or their control gains should be reduced. While at the same time the mirror displacements and orientation have to be kept in a certain range so that the interferometer is kept with good sensitivity to gravitational waves.

The phases of interferometer consitions and requirements on the active controls are summarized in Fig. 5.1.

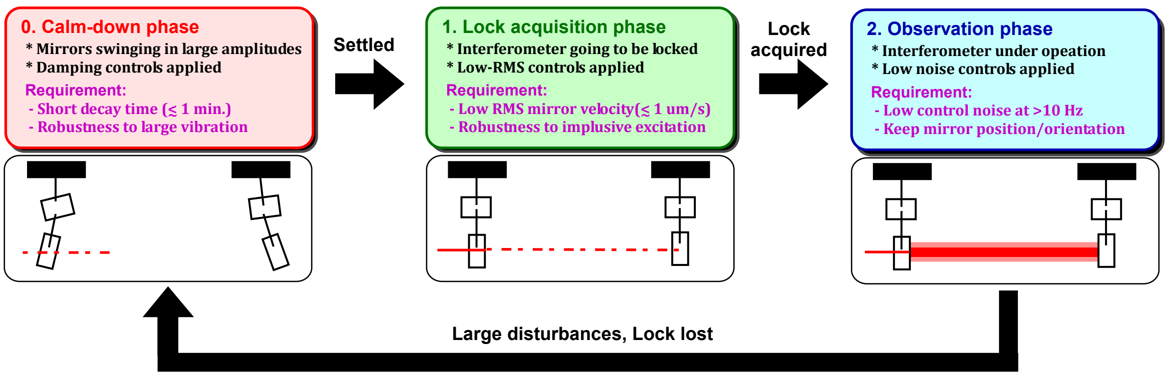

Figure 5.1: Digram of active control phases and the requirements in each phase.

5.2.2 Mirror velocity requirement

As discussed in section **??**, control signals of a linear optical cavity and a Michelson interferometer can be obtained by using frontal modulation technique. By demodulating detected laser power in a proper phase, one can obtain a control signal proportional to the optical cavity length around the operation point. The linear range of the control signal can be roughly calculated from the finesse of the cavity ($\mathcal{F}$) and wave length of the laser light (λ) as

$$\varDelta L_{\mathrm{lin}} = \frac{\lambda}{2\mathcal{F}}. \tag{5.1}$$

The finesses of the cavities are 38 for the signal recycling cavity, 57 for the power recycling cavity and 1550 for the arm cavities (and 1 for the Michelson interferometer) in the KAGRA interferometer. For the arm cavities, we plan to use green lock scheme and the finesse for the green laser will be set ~ 50.

In order to acquire the lock of an optical cavity, the velocity of cavity length change should be nulled by feedback forces applied to suspended mirrors while the mirrors pass through the linear range. The maximum momentum applied to the suspended mirror by feedback force is limited by staying time of mirrors in the linear regime, the control bandwidth and maximum actuation power of coils.

When the control bandwidth is not large enough, the servo responds too slowly and fails to apply sufficient feedback force before the mirrors pass by the linear regime. The control bandwidth would be limited by response of actuators and existence of mechanical resonances. For the lock acquisition of the arm cavities, we can use voltage controlled oscillators (VCOs) to modulate the laser frequencies as actuators, which have large controllable range and bandwidth. These actuators are free from mechanical resonances of mirrors and therefore we can set the control bandwidth as high as 10 kHz. On the otherhand, lock acquisition about the other DoFs should be accomplished by mechanical actuators attached on mirrors and the bandwidth is limited by existence of mechanical resonances especially from violin modes of suspension wires which produce peaks in the frequency response around 200 Hz and its harmonics. Thence we need to set the control bandwidth as low as 50 Hz for these DoFs.

Assuming that the actuators have sufficient actuation range and feedback controls are applied only during the time mirrors are in the linear regime, the requirement on the incident velocity of the cavity length change to acquire the lock is calculated as

$$v_{\rm in} \lesssim \omega_b \Delta L_{\rm lin} = \frac{\omega_b \lambda}{2\mathcal{F}}. \tag{5.2}$$

Here ω_b is the control bandwidth or unity gain frequency of the feedback loop. Note that actual feedback signals are non-linear to the cavity length and the requirement could differ if the non-linearity is taken into account, but the order should be the same.

In actual cases, maximum forces which can be applied by the actuators are limited from the point of view of control noise requirement. The stronger actuators we use, the more noise introduced to the mirror displacement in the observation frequency band. Typically the voltage applied on the coil magnet actuators has a noise level $\tilde{V}_{\rm n} \sim 10^{-8}\ \mu{\rm V}/\sqrt{\rm Hz}$ around 10 Hz and the maximum applicable voltage is $V_{\rm max}$ =10 V. The coil driving noise should be suppresed lower than the required displacement noise of the mirrors. Thence maximum acceleration applicable on the mirror is calculated as

$$a_{\rm max} = \frac{V_{\rm max}}{\tilde{V}_n} \tilde{x}_{\rm req} \omega_{\rm obs}^2. \tag{5.3}$$

Here $\tilde{x}_{\rm req}$ is the required displacement noise level (in ${\rm m}/\sqrt{\rm Hz}$) and $\omega_{\rm obs}$ is the frequency at which the noise requirement should be satisfied. In our case, the requirement gets strictest at $f_{\rm obs} = 10$ Hz.

Here we set different assumption that the control bandwidth is large enough but the actuators can apply limited acceleration ($a_{\rm max}$) on the mirrors. The requirement on the velocity to achieve lock acquisition during the mirrors stay in the linear regime is calculated as

$$v_{\rm in} \lesssim \sqrt{2 a_{\rm max} \Delta L_{\rm lin}}. \tag{5.4}$$

Cavity/interferometer	Requirement from BW	Requirement from $a_{\rm max}$
Arm cavities	10	–
Power recycling cavity	2.8	37
Signal recycling cavity	4.1	3.2
Michelson interferometer	157	20

Table 5.1: Requirement

5.3 Active Controls for KAGRA-SAS

As described in the previous chapter, SAS has a feature of utilizing low frequency oscillators such as inverted pendulums and GAS filters. Such oscillators often suffer from large thermal drift and creep due to cracks inside elastic components. Therefore active DC controls are required to hold the oscillators back to their nominal positions. Regarding the controls for high frequencies, active damping controls are required to suppress the vibration due to mechanical resonances of the suspension systems.

The follwing figure shows the schematics of active control loops for KAGRA-SAS. The top stage held by inverted pendulums is controlled by the use of two kinds of sensors: displacement sensors and seismeters. The displacement sensors measure the relative displacement between the top stage and the frame fixed to the ground. They are used to compensate the drift of the inverted pendulums. Seismometers, or accelerometers measure the vibration of the top stage with respect to the inertial frame. They are used to damp the pendulum modes of the masses suspended below.

Each GAS filter possesses a displacement sensor on the vertical axis to measures the displacement of the keystone with respect to the frame holding the springs. Signals from the displacement sensor are used to compensate the drift of the springs and to damp the resonances.

The vibration of the payload is observed by the use of displacement sensors which measure the relative displacements of the intermediate mass and mirror with respect to their recoil masses. They are used to damp mechanical resonances of the payload which cannot be damped by the top stage active control. Especially, tilt motions of the mirror can be only controlled in this part since the intermediate mass is suspended by a single wire and the tilt motions are seperated from the tilt of upper masses.

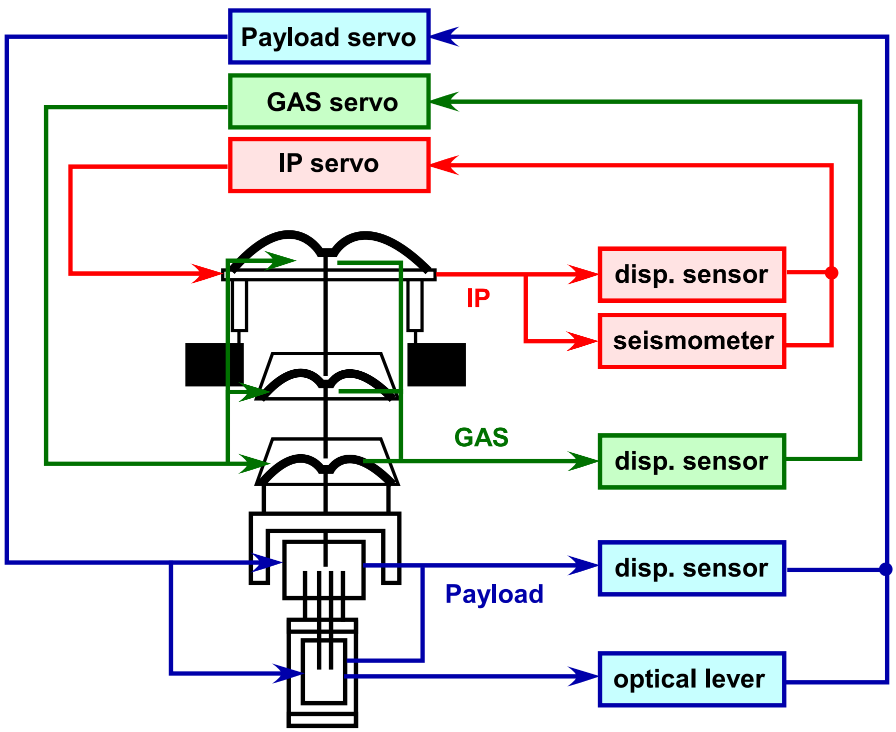

Figure 5.2: Schematics of the active control structure for KAGRA-SAS.

Performance test on individual SAS components

Chapter 6

6.1 Overview

6.2 倒立振り子の制御

6.2.1 制御試験の目的

6.2.2 実験セットアップ

倒立振り子の制御実験のセットアップを図 6.1 に示す。倒立振り子によって支えられたトップステージには鉛直方向防振用の GAS フィルターが搭載され、GAS フィルターよりワイヤーにてマスが懸架される。懸架されるマスの質量は GAS フィルターが支える重量に等しく約 330 kg である。倒立振り子の共振周波数は 100-120 mHz に調整されている。トップステージの水平面内の動きは LVDT，geophone の 2 種類のセンサーを用いて測定され、LVDT は地面に対するステージの変位を、geophone は慣性系に対するステージの速度を測定する。センサーの信号は ADC (Analog to Digital Converter) を通じてデジタルシステムに送られ、デジタルシステム内で処理された信号が DAC (Digital to Analog Converter) を通じてコイル-磁石アクチュエータに向かいトップステージの動きを制御する。

トップステージ上のセンサーおよびアクチュエータの配置を図 6.1 に示す。ステージの 3 自由度の動きを測定するため、制御に用いる LVDT および geophone がそれぞれ 3 個ずつ 120 度離れた位置に配置されている。トップステージを駆動するためのコイル-磁石アクチュエータは LVDT と同軸上に配置されている。またセンサーやアクチュエータの雑音といった制御雑音の影響を調べるため、制御ループ外センサーとしてステージの X 軸方向の並進モードを見る geophone をステージ上に配置した。

ステージの DC 位置を調整するため、ステッピングモーターで駆動するばねが 3 箇所に配置されている。DC 位置調整用のばねの構造を図 6.3 に示す。ステッピングモータでスライドするブロックには厚さ 0.3 mm の 48Si7 鉄の板ばねが 2 枚取り付けられ、ブロックが移動すると左右のばねの引張力が変化しブロックが移動した向きにトップステージが引

Figure 6.1: 倒立振り子の制御実験のセットアップ

Figure 6.2: トップステージ上のセンサーおよびアクチュエータの配置

き寄せられる。板ばねにより生じる復元力は倒立振り子自身が持つ復元力よりも小さく倒立振り子の動作に大きな影響を与えないようになっている。

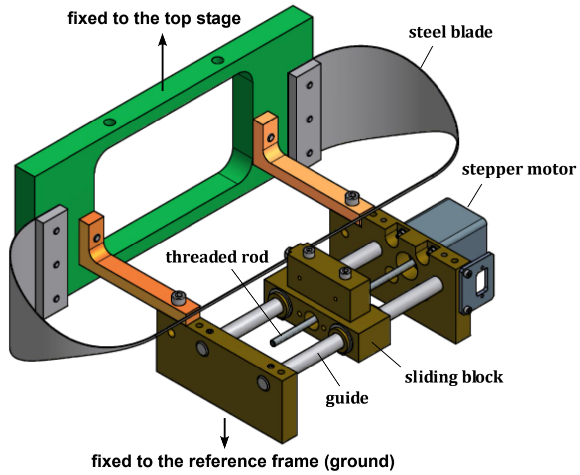

Figure 6.3: トップステージの DC 位置調整用のばね＋スライダー機構

倒立振り子の制御ダイアグラムを図 6.4 に示す。センサー (LVDT，geophone) の信号はキャリブレーション結果や周波数応答の補正により変位情報に変換された後、座標変換によりステージの x, y, θ 座標の変位に変換される。座標変換は $3{\times}3$ の変換行列 S によって行われる。2 種類のセンサーで測定された各座標の変位はそれぞれサーボフィルターを通り、足し合されて各座標に関するアクチュエータの信号となる。各座標に関するアクチュエータの制御信号は、座標変換（$3{\times}3$ 変換行列 D）によりステージ上に配置された各アクチュエータに対する信号に変換され、ステージの動きが制御される。

Figure 6.4: 倒立振り子の制御ダイアグラム

6.2.3 センサーの準備と雑音評価

LVDT

LVDT は地面に対するトップステージの相対変位を測定し、主にステージの DC 制御に用いられる。LVDT はコイル-磁石アクチュエータと一体になっており、図 6.5 に示されるような構造をしている。変調磁場を発生させる emitter coil はトップステージ側に固定され、変調磁場による誘導起電力を受ける receiver coils は地面側に固定される。

Figure 6.5: LVDT とコイル磁石アクチュエータのユニット

LVDT 駆動回路の概略図を図 6.6 に示す。信号発生器より発生させた変調信号はバッファを通して emittor coil に送られ変調磁場を発生させる。今回の試験では変調信号として 10 kHz のサイン波を用いた。誘導起電力により receiver coil に発生した信号が位相ソフト回路を通した変調信号により復調され、ローパスフィルターを通って低周波成分のみが取り出される。今回使用した駆動回路は advanced Virgo 用に NIKHEF で開発されたもので、詳細は [75] に記載されている。

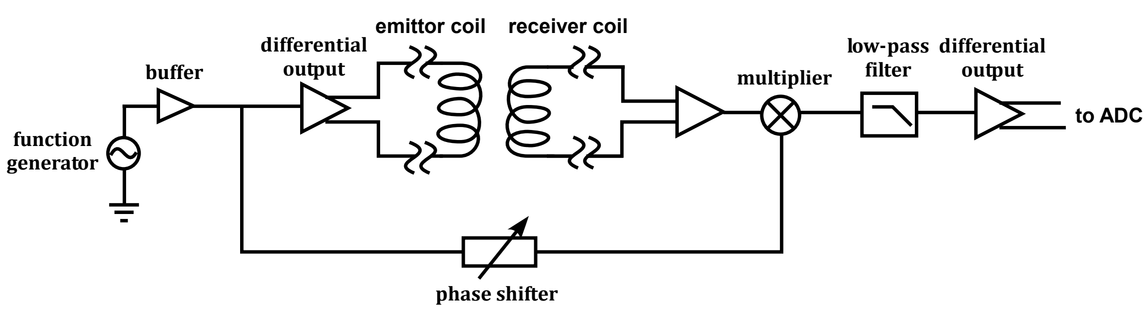

Figure 6.6: LVDT 駆動回路の概略図

1 台の LVDT に関するキャリブレーション結果を図 6.7 に示す。LVDT の出力が 0 となる点より ±5 mm の範囲内で LVDT は線形な応答を示しており、およそ 2 V/mm の感度が得られている。

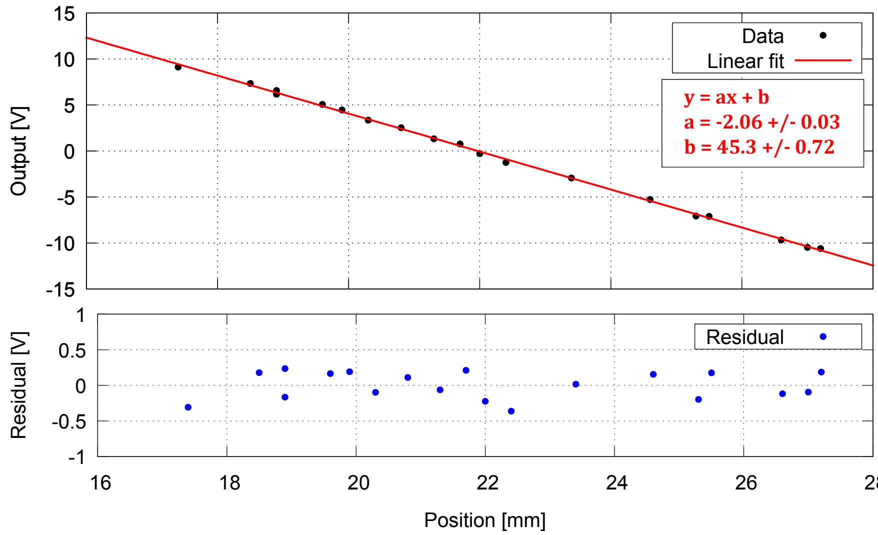

Figure 6.7: LVDT のキャリブレーション結果

ステージを固定した状態での LVDT の雑音スペクトルを測定結果を図 6.8 に示す。LVDT の雑音はデジタルシステムのデータ取得系の雑音 (ADC の量子化雑音) により制限されており、測定された雑音のスペクトル密度は 10 Hz において 4 μV/$\sqrt{\mathrm{Hz}}$、変位換算で 2 nm/$\sqrt{\mathrm{Hz}}$ であった。

Geophone

高周波においてトップステージの振動を制御する際、地面振動雑音の再導入による防振比悪化を防ぐため制御には地面振動を参照しない慣性系に対するセンサーが用いられる。今回の制御試験では Mark Product 社の geophone L-4C を使用した。Geophone は電磁誘導を利用して振動子の振動を読み出す型の地震計で、外部からの制御を必要としない受動的なセンサーである。振動子の共振周波数よりも高い周波数において出力電圧は地面振動の速度に比例する。Geophone の地面振動速度に対する周波数応答は以下の式で表される。

$$H_{\mathrm{geo}}(\omega) = \frac{G\omega^2}{\omega_0^2 + 2ib\omega_0\omega - \omega^2} \tag{6.1}$$

G は速度に対する感度を表し generator constant とも呼ばれる。ω_0 は内部に含まれる振動子の共振周波数、b はその減衰比を表す。典型的な L-4C のパラメータと地面振動の速度に対する周波数応答を表 6.1 および図 6.9 に示す。

Geophone の感度は信号を増幅するためのプリアンプの雑音により主に制限される。今回の試験では advanced Virgo 用に NIKHEF にてデザインされたプリアンプを使用した [?]。図 6.10 にプリアンプの写真および初段の増幅回路を示す。Geophone の信号は初段の増幅回路で約 380 倍に増幅された後、5 倍のゲインでシングルエンドから差動出力に変換され信号取得系に送られる。

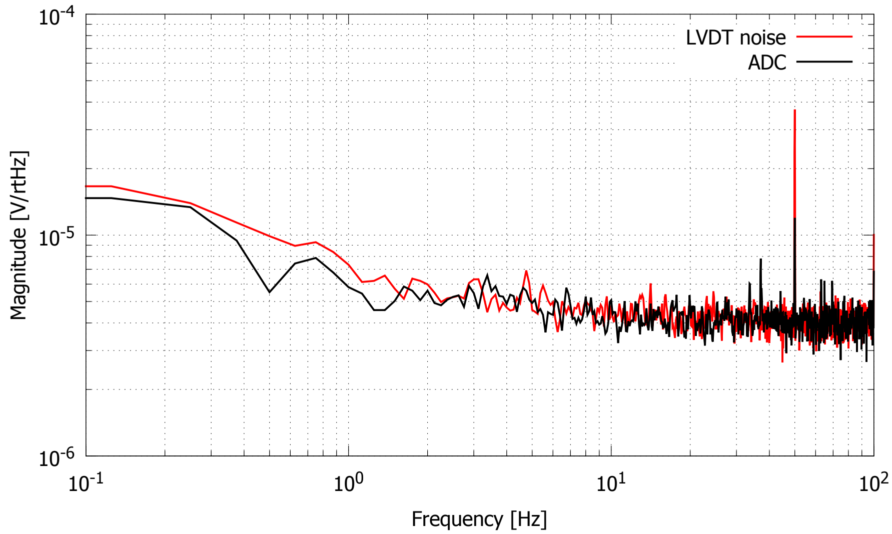

Figure 6.8: LVDT の雑音スペクトルと ADC の雑音の比較

Generator constant (sensitivity)	276 V/(m/sec)
Mass of the oscillator	0.970 kg
Resonant frequency of the oscillator	1.0 Hz
Intrinsic damping ratio	0.28
Coil resistance	5500 Ω

Table 6.1: L-4C の典型的なパラメータ

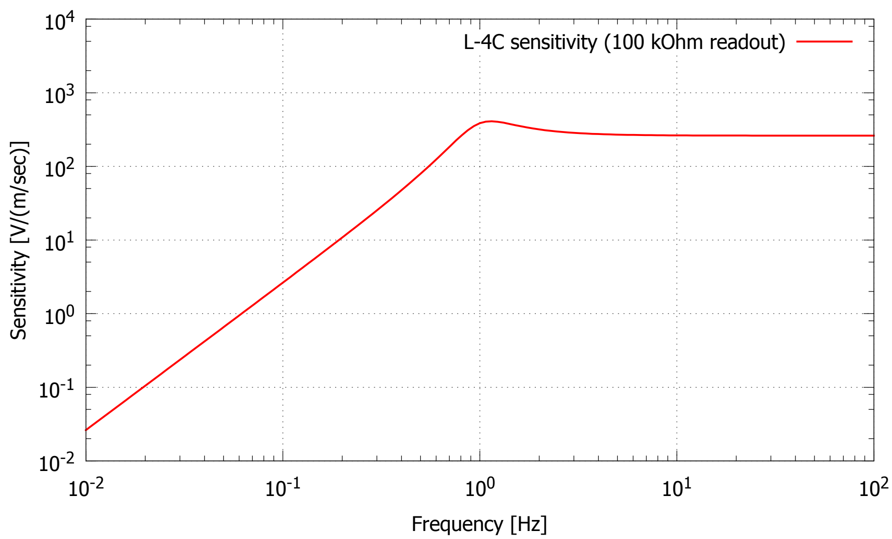

Figure 6.9: L-4C の地面振動に対する周波数応答

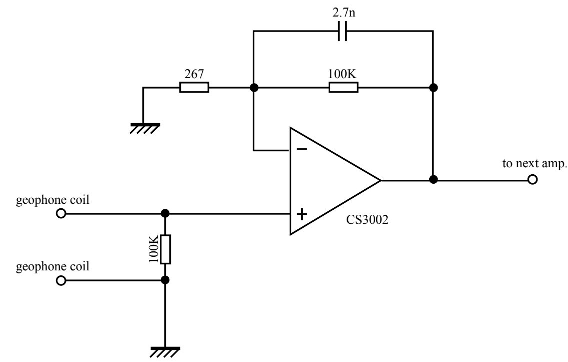

Figure 6.10: Geophone 用プリアンプの写真 (左) および初段の増幅回路の配線図 (右)

プリアンプの雑音は初段の増幅回路のオペアンプ (CS3002) の電圧性雑音および電流性雑音、入力抵抗の熱雑音により決定される。プリアンプの雑音のパワースペクトル $P_{nn}(f)$ は以下の式で計算される。

$$P_{nn}(f) = V_{nn}\left(1+\frac{f_{cv}}{f}\right) + I_{nn}\left(1+\frac{f_{cc}}{f}\right)R^2 + 4\pi k_B RT. \tag{6.2}$$

第 1 項がオペアンプの電圧性雑音、第 2 項がオペアンプの電流性雑音、第 3 項が抵抗の熱雑音を表す。ここで R は回路の入力抵抗、k_B はボルツマン定数、T は温度である。オペアンプの電圧性および電流性雑音は低周波で $1/f$ に比例して上昇し、f_{cv} および f_{cc} はその立ち上がり周波数を表す。

図 6.11 にプリアンプ回路の入力換算雑音の見積もりと実測データ（出力電圧のスペクトルを回路のゲインで割ったもの）との比較を示す。雑音測定はプリアンプの入力に L-4C のコイルと同じ抵抗値 (5500 Ω) を持つ抵抗器をつなげた状態で行った。グラフの measurement(1) はプリアンプを大気に露出した状態で測定したもので、measurenet(2) はプリアンプを断熱材で囲まれた箱に入れた状態で測定したものである。Measurement(2) の測定結果は計算結果と良く一致しているが、プリアンプを大気に晒した measurement(1) の測定結果では 1 Hz 以下の低周波でプリアンプ雑音が増大している。原因としては、プリアンプ自身が発生する熱により温度揺らぎが生じ増幅回路内の抵抗値が変動したり熱起電力が生じたりといったことが考えられる。

プリアンプの雑音の測定結果 (measurement(2)) と周波数応答 (図 6.9) から計算される geophone の変位換算雑音と LVDT の変位雑音の比較を図 6.12 に示す。Geophone の雑音は 0.1 Hz 以上で LVDT の雑音レベルを下回るが、振動子の共振周波数以下では急激に雑音レベルが上昇する。

6.2.4 倒立振り子の共振周波数の調整

地面振動の 200 mHz 付近の micro-seismic peak の影響を低減するため、倒立振り子の共振周波数は 100 mHz 以下に下げることが求められる。トップステージに荷重を加えてい

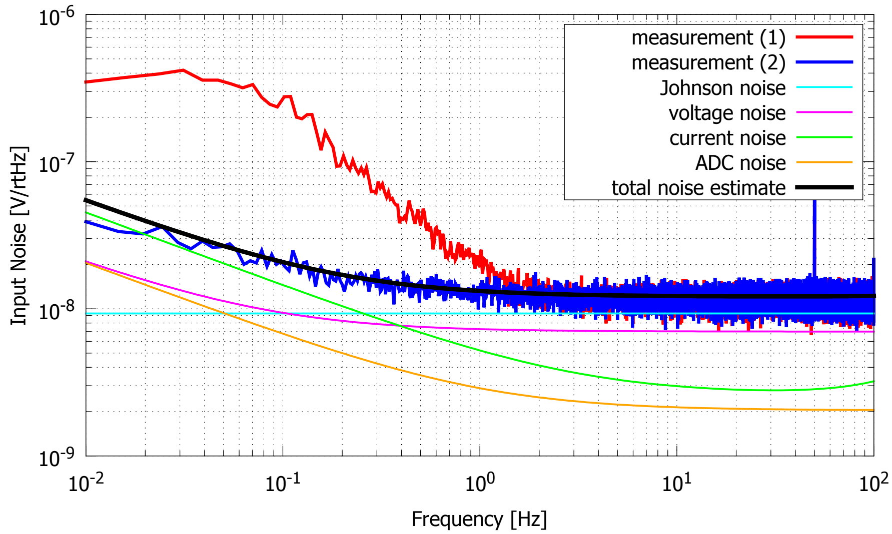

Figure 6.11: プリアンプの入力換算雑音。赤線と青線が実測データ、その他の細線が推定される雑音源のスペクトルを表し、黒い太線がその総和を表す。

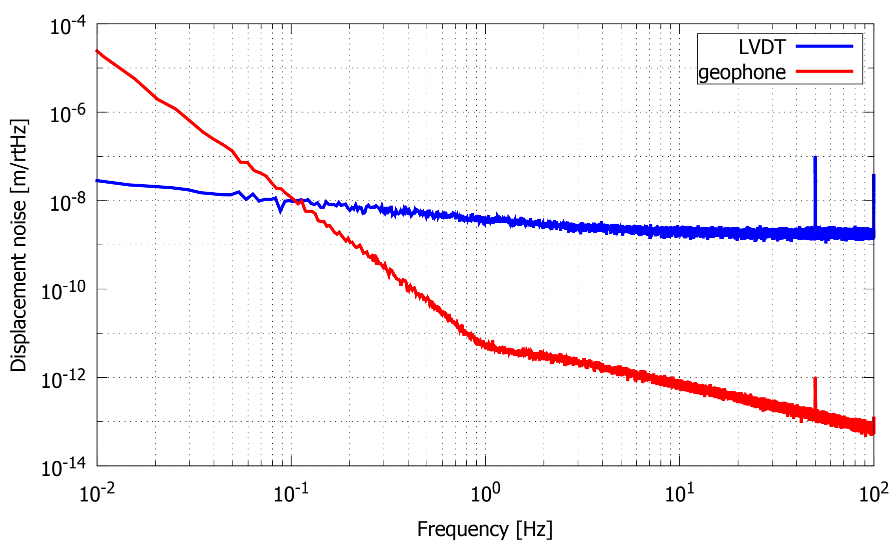

Figure 6.12: Geophone と LVDT の変位雑音レベルの比較

くことで重力による反ばね力が増大し倒立振り子の共振周波数は下がっていく。倒立振り子に荷重を加えていった時の並進モードの共振周波数の推移の測定結果を図 6.13 に示す。

Figure 6.13: 倒立振り子の荷重と共振周波数の関係

トップステージに質量 x のおもりを追加したときの倒立振り子の共振周波数 f_{IP} は以下の式で表される。

$$f_{\mathrm{IP}} = f_0\sqrt{\frac{M_c}{x+M_0}-1} \quad \left(f_0 = \frac{1}{2\pi}\sqrt{\frac{g}{L}}\right). \tag{6.3}$$

ここで L は倒立振り子の脚の長さ、M_0 はおもりを除いたトップステージの質量を表し、今回のセットアップでは $L = 0.48$ m, $M_0 = 310$ kg となっている。この式より共振周波数を 0 Hz とするのに必要な倒立振り子の荷重 M_c をフィッティングにより求めると $M_c = 1108 \pm 4$ kg となる。

6.2.5 座標変換とステージの変位スペクトル

倒立振り子の並進モードの共振周波数を 0.12 Hz に調整した時の、定常状態における各 LVDT の出力のスペクトルと、それを行列 S で変換したステージの座標系における変位スペクトル密度を図 6.14 に示す。各センサーの変位出力 (S_1, S_2, S_3) をトップステージの座標系 (x,y,θ) に変換する変換行列 (S) は以下の式で表される。

$$\begin{pmatrix} x \\ y \\ r\theta \end{pmatrix} = \underbrace{\begin{pmatrix} 1/3 & 1/3 & -2/3 \\ 1/\sqrt{3} & -1/\sqrt{3} & 0 \\ 1/3 & 1/3 & 1/3 \end{pmatrix}}_{\boldsymbol{S}} \begin{pmatrix} S_1 \\ S_2 \\ S_3 \end{pmatrix}. \tag{6.4}$$

ここで r はトップステージの中心からセンサーの位置までの距離を表し、LVDT に対しては $r = 0.7$ m，geophone に対しては $r = 0.5$ m となる。

ステージの座標系に変換することにより共振ピークが分離し、各ピークに対応する共振モードを推定することができる。図 6.14 右下に、この系の剛体モデルから予想される各共振ピークのモードを示す。最も低い周波数の共振は懸架されたダミーマスの鉛直軸周りの回転モードにより生じ、1 本吊りの懸架ワイヤーが捩れる動作に対応する。倒立振り子の動作に対応するのは 0.12 Hz の並進モードと 0.20 Hz の回転モードのピークで、どちらも機械的 Q 値は 10 程度である。0.37 Hz 付近の鋭いピークは懸架されるダミーマスの振り子の共振に対応する。振り子の共振は Q 値が非常に高く、ステージの変位の RMS 振幅に大きく寄与する。

Figure 6.14: LVDT により測定されたステージの変位スペクトルと共振モードの同定

6.2.6 アクチュエータの対角化と伝達関数

倒立振り子をトップステージの座標系 (x, y, θ) について制御するためには、それぞれの向きにステージを駆動するためのアクチュエータへの入力信号の配分を知る必要がある。

すなわちステージの各座標に対応する仮想的なアクチュエータの信号を、実際に設置されている 3 台のアクチュエータの入力信号に変換する行列を決定する必要がある。この行列の決定をアクチュエータの対角化と呼ぶ。アクチュエータによって得たいステージの変位を (u_x, u_y, u_θ)、3 台のアクチュエータへの入力信号を (A_1, A_2, A_3) としてアクチュエータの対角化行列 D は以下の式で表される。

$$\begin{pmatrix} A_1 \\ A_2 \\ A_3 \end{pmatrix} = \underbrace{\begin{pmatrix} D_{1,x} & D_{1,y} & D_{1,\theta} \\ D_{2,x} & D_{2,y} & D_{2,\theta} \\ D_{3,x} & D_{3,y} & D_{3,\theta} \end{pmatrix}}_{\boldsymbol{D}} \begin{pmatrix} u_x \\ u_y \\ u_\theta \end{pmatrix}. \tag{6.5}$$

アクチュエータの対角化の手順は以下の通りである。最初に対角化行列 $\boldsymbol{D}$ に適当な成分を与える ($\boldsymbol{D} = \boldsymbol{D}_{\rm init}$)。このようにして仮に設定された仮想アクチュエータを用いてステージの振動を励起し、ステージの各座標に対する仮想センサーの出力 (x, y, θ) を読み取る。励起には系の持つ共振周波数よりも十分低い周波数 f_D のサイン波を使用する（本実験では $f_D = 10$ mHz を使用)。これにより各座標に対応する仮想アクチュエータから仮想センサーへの周波数 f_D における伝達係数行列 $\boldsymbol{E}$ が求まる。

$$\boldsymbol{E} = \begin{pmatrix} \tilde{x}/\tilde{u}_x & \tilde{x}/\tilde{u}_y & \tilde{x}/\tilde{u}_\theta \\ \tilde{y}/\tilde{u}_x & \tilde{x}/\tilde{u}_y & \tilde{x}/\tilde{u}_\theta \\ \tilde{\theta}/\tilde{u}_x & \tilde{\theta}/\tilde{F}_y & \tilde{\theta}/\tilde{u}_\theta \end{pmatrix}_{f=f_D}. \tag{6.6}$$

得られた行列 $\boldsymbol{E}$ の逆行列を $\boldsymbol{D}$ に掛けることで新たな対角化行列 $\boldsymbol{D}_{\rm new} = \boldsymbol{E}^{-1}\boldsymbol{D}_{\rm init}$ を得る。ここで得られた対角化行列により設定された仮想アクチュエータを用いて再び伝達係数を測定し、行列 $\boldsymbol{D}$ をアップデートする。伝達係数行列 $\boldsymbol{E}$ が単位行列に近付くまでこの作業を繰り返す。今回の測定では行列 $\boldsymbol{E}$ の非対角項が 0.01 以下 (自由度間のカップリングが 1%以下) になるまで対角化作業を繰り返した。

こうして設定された仮想アクチュエータから LVDT で測定されたステージの各自由度の変位への伝達関数を図 6.15 に示す。対角化により 10 mHz 付近で自由度間のカップリングが 1%程度に低減されていることがわかる。一方で共振周波数近傍とそれよりも高い周波数ではカップリングは 1%よりも大きくなっている。これは 3 本の倒立振り子の脚が持つ実効的なばね定数に非対称性があり、低周波において対角化されたアクチュエータは純粋な x 軸や y 軸方向の力、z 軸周りの回転トルクを与えるものではないためであると考えられる。

6.2.7 制御フィルター

ステージの変位の RMS 振幅に大きく貢献する振り子の共振を減衰するためのダンピング制御を実施した。使用したサーボフィルターは

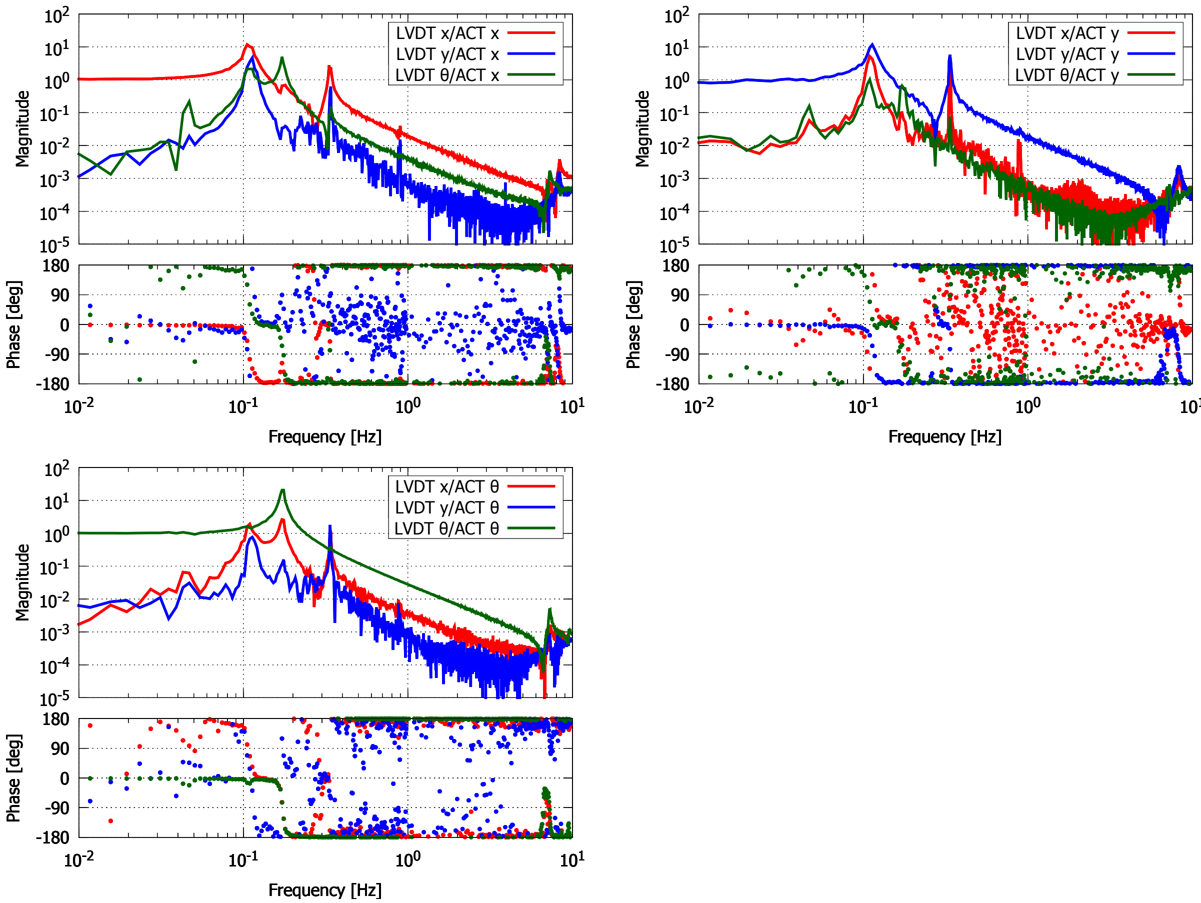

Figure 6.15: 対角化されたアクチュエータから LVDT で測定されたステージ変位への伝達関数

6.3 防振性能の評価

6.3.1 Multi-SAS 用倒立振り子

倒立振り子の防振性能を測るため、地面振動から倒立振り子で支持されたステージの振動への伝達関数の測定を行った。測定に使用した倒立振り子は、ヨーロッパの第 2 世代干渉計型重力波検出器 Advanced Virgo において Multi-SAS と呼ばれる防振系で用いられるものである。Multi-SAS は干渉計のアラインメントを測定するための光学系が搭載される光学ベンチを防振するシステムであり、その基本構造は KAGRA-SAS と良く似ている（図 6.16）。Multi-SAS で用いられる倒立振り子は KAGRA-SAS で用いられるものと同様のデザインであり、今回の測定結果は KAGRA-SAS における倒立振り子の防振特性も示唆する。本実験は Advanced Virgo のための機器開発が行われている研究機関の一つである NIKHEF（オランダ）にて、2013 年 1-3 月の同機関滞在中に行ったものである。

Figure 6.16: multi-SAS の概観

6.3.2 実験セットアップ

図 6.17 に Multi-SAS 用倒立振り子の伝達関数測定のセットアップの写真と概略図を示す。測定の対象となる系は倒立振り子によって支えられるトップステージとそこからワイヤーを通じて懸架されるダミーマスの 2 段振り子構成となっている。測定時、倒立振り子の並進モードの共振周波数は 250 mHz に調整されていた。倒立振り子を支えるベースは金属板ばねにより懸架され、ピエゾアクチュエータを用いて水平方向に加振される。振動を測定するため Wilcoxon 社のピエゾ型加速度計 Model 731-20 をベースおよびトップステージに配置した。加速度計の感度は 10 V/g (2.5 Hz – 2.5 kHz) で雑音レベルはおよそ 0.1 $\mu g/\sqrt{\mathrm{Hz}}$ である。加振と平行な方向の振動を測定するため水平加速度計がトップステージとベースにそれぞれ 1 個ずつ配置し、ベースの傾きを測定するため鉛直加速度計をベースに 2 個配置した。

伝達関数の測定には swept-sine 法を使いた。LabView のプログラムを利用し、励起するベースの振動の周波数を少しずつ変えながら各加速度計の出力電圧の振幅および位相を

比較した。今回測定を行った周波数の帯域は 2 – 80 Hz である。測定に使用した加速度計はあらかじめ同じステージ上で加振して出力電圧の差を測定し、測定された出力電圧に係数を掛けることで加速度計ごとの感度の違いを補正した。

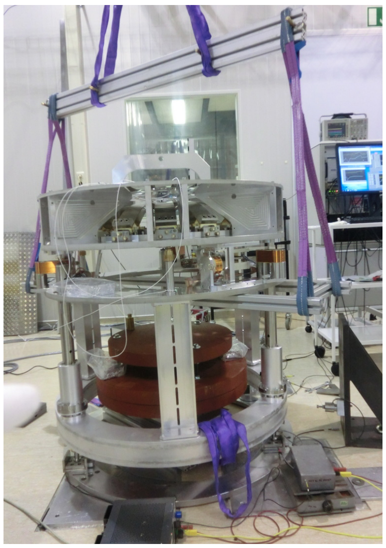

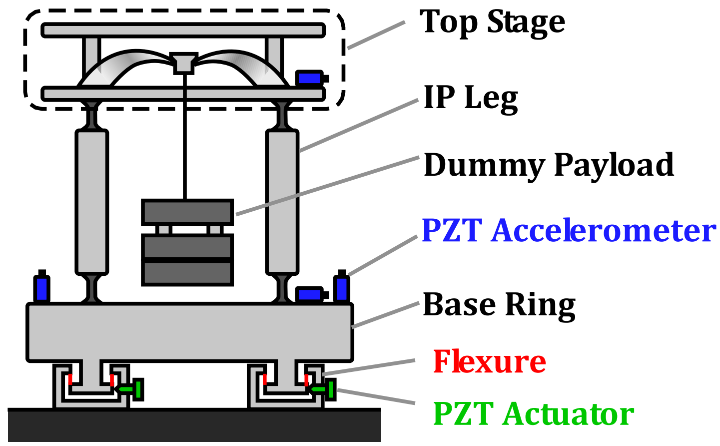

Figure 6.17: multi-SAS 用倒立振り子の伝達関数測定のセットアップ

6.3.3 測定結果

図 6.18 に測定された加速度計の周波数ごとの出力電圧振幅を示す。ベースの傾きはベースに設置された鉛直加速度計の出力の差分を取り計算した。グラフにおいて 68 Hz に現れるピークはベースを支える板ばねの共振によるものである。ピエゾアクチュエータへの入力電圧の振幅は全周波数で一定であり、ベースの変位振幅がほぼ一定であるためベースに設置された水平加速度計の出力電圧の振幅は周波数の二乗に比例している（図 6.18 青線）。トップステージに設置された水平加速度計の出力（図 6.18 赤線）はベースに設置された水平加速度計の出力よりも小さく、倒立振り子による防振効果が確認できる。

ベースの傾きの振幅（図 6.18 緑線）は周波数が上がっていくと急激に上昇し板ばねの共振周波数でピークを迎える。ベースが傾く理由としてはアクチュエータの設置位置とベースの重心位置のズレや、ベースを支持する板バネの非対称性等が考えられる。ベースの傾きは後述するように高周波における倒立振り子の伝達関数測定に影響する。

ベースとトップステージに設置された水平加速度計の出力の比から計算される倒立振り子の振動伝達関数のボーデ線図を図 6.19 に示す。青線は 2 段振り子の質点モデルにより計算される伝達関数の理論曲線で、Center of Percussion 効果による倒立振り子の防振比飽和は –80 dB を仮定している（式??における $\beta = -10^{-4}$）。理論曲線に現れる 0.8 Hz のディップと 1.2 Hz のピークはトップステージから懸架される振り子の寄生共振によるものである。

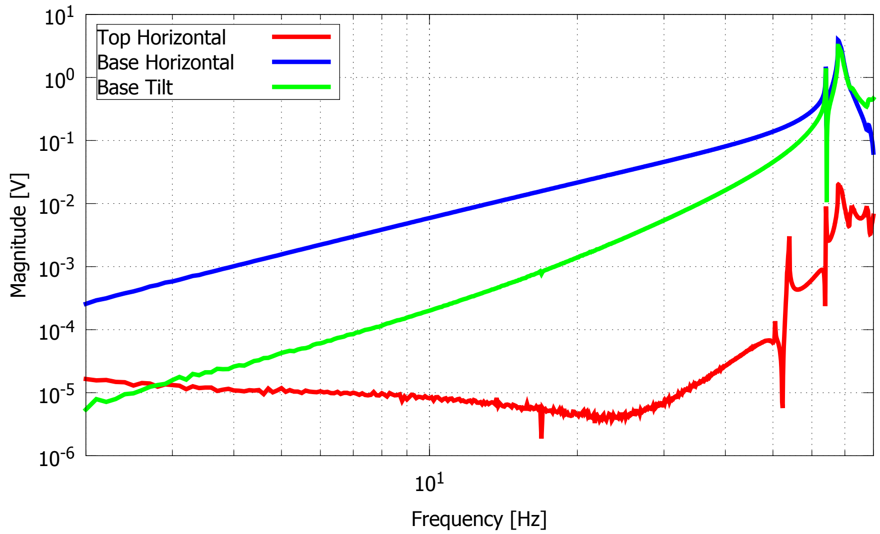

Figure 6.18: 加速度計の周波数ごとの出力電圧振幅

測定された伝達関数は 20 Hz 以下で理論と良く一致しており、最大で −80 dB の防振効果が確認された。一方で高周波では伝達関数の絶対値が上昇していく様子が確認されているが、これは倒立振り子の防振性能が悪化している訳ではなく、後述するベースの傾きからのカップリングによりトップステージに設置した水平加速度計の出力が増大しているためであると考えられる。

6.3.4 傾きによるカップリング

今回の試験では倒立振り子を支持するベースには純粋な水平並進運動だけではなく回転運動（傾き）が生じている。ベースの回転運動がトップステージ上に設置された水平加速度計に与える影響は、1. トップステージの並進運動によるもの と 2. トップステージの回転運動（傾き）によるものの 2 種類に分けられる（図 6.20）。

最初に考えられる影響は、ベースが傾くことで倒立振り子の flex joint の弾性によりトップステージに並進運動が生じ、トップステージに設置された加速度計に出力が生じるものである（図 6.20 左）。ベースの回転角度からステージの変位への伝達関数は図 6.21 の赤線で表される。振り子の共振よりも高い周波数では伝達関数の絶対値は周波数の 2 乗に反比例して落ちていくため、高周波ではこちらの影響は効き難い。

次に考えられる影響は、ベースの傾きによりトップステージが傾くことで加速度計に出力が生じるものである（図 6.20 右）。倒立振り子の脚が軸方向に非常に硬く剛体と見なせる場合、トップステージの回転角はベースの回転角と等しくなる。ステージの回転中心が加速度計と同じ水平面内に無い場合、ステージの回転運動により水平加速度計に出力が生じる。カップリングの大きさはステージの回転中心と加速度計設置位置の高さの差 δh に比例する。倒立振り子の脚を剛体と見なした場合、ベースの傾きから加速度計の位置における水平方向の変位への伝達関数は図 6.21 の青線で示されるように周波数に対してフラットとなり、高周波ではこちらの影響が支配的となる。

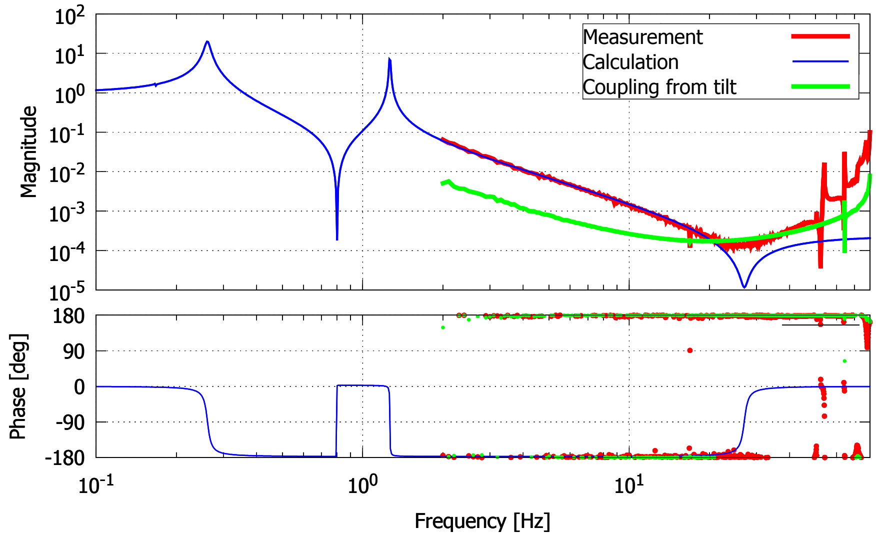

Figure 6.19: Multi-SAS 用倒立振り子の伝達関数

ステージの回転運動からのカップリングは、トップステージに設置された加速度計の位置を調整することにより低減が可能である。図 6.19 で測定された伝達関数は加速度計の高さを最適化した時のものである。図 6.19 の緑線は図 6.21 に示される関数をもとにベースの傾きからのカップリングを計算したものである。ステージの回転中心と加速度計設置位置の高さのずれは $\delta h = 1$ mm としている。計算されたカップリングは 20 Hz 以上の測定結果を良く説明している。

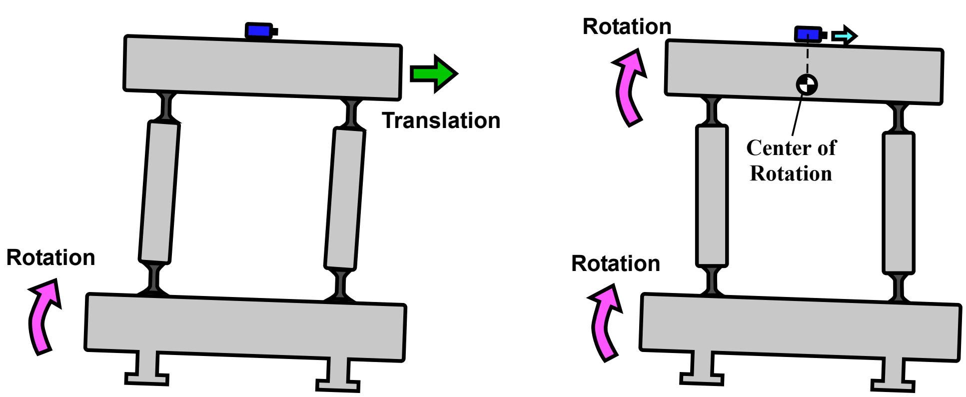

Figure 6.20: ベースの傾きからトップステージ上の水平加速度計へのカップリング

6.3.5 カウンターウエイトの調整

??節で説明した Center of Percussion 効果による防振比飽和を緩和するため、倒立振り子の脚にはカウンターウエイトを取り付けることができるようになっている。カウンター

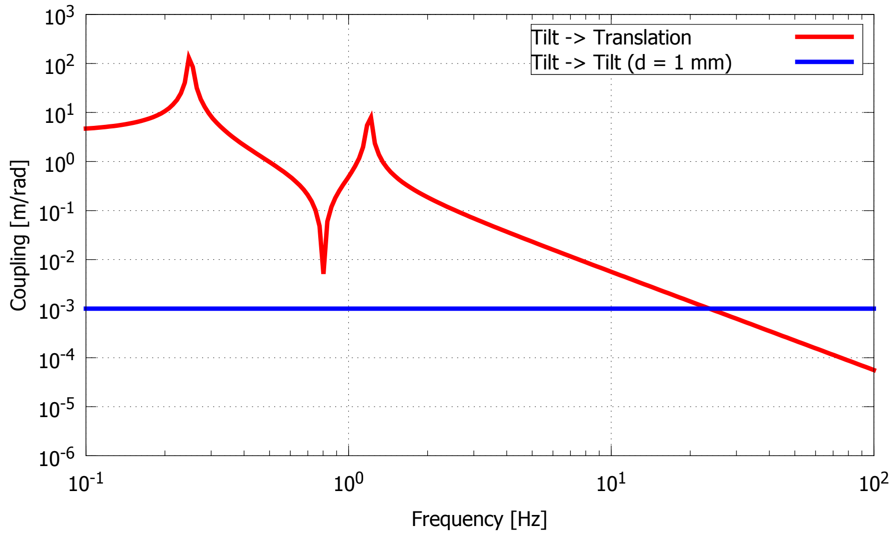

Figure 6.21: ベースの傾き角度からトップステージに設置された水平加速度計の位置における水平変位への伝達関数

ウエイトの重さを変化させた時の 10 – 50 Hz の倒立振り子の防振比の変化を図 6.22 に示す。カウンターウエイトを載せない場合には防振比は-65 dB 程度で飽和するが、カウンターウエイトの重さを調節することで-80 dB 以上の防振比を持たせられることが、この測定結果により示された。

6.4 GAS フィルターの防振性能測定

KAGRA-SAS において鉛直方向防振の要となる GAS フィルターの防振性能を評価するため、加振実験による GAS フィルターの伝達関数測定を実施した。GAS フィルターの防振性能は振動子を構成する板ばねの質量分布のために、倒立振り子の Center of Percussion 効果と同様の効果によって高周波において飽和すると考えられている。この防振比飽和を低減するため、倒立振り子におけるカウンターウエイトと同様の効果を持つ、magic wand と呼ばれる機構が導入される。本試験では伝達関数測定のセットアップを用いて magic wand の調整による防振性能の低減を確認する。

6.4.1 実験セットアップ

GAS フィルターの伝達関数測定のセットアップを図 6.23 に示す。測定を行ったのは KAGRA 用に開発された standard GAS フィルターのプロトタイプである。GAS フィルターのベースをコイルばねを用いて懸架し、電磁アクチュエータにより振動を励起する。GAS フィルターのベースと GAS フィルターより懸架されるダミーマスには鉛直方向に加速度計が取り付けられ、両者の出力の比を取ることにより伝達関数が測定される。使用した加速度計は TEAC 社のピエゾ型加速度計 SA-710 で感度はおよそ 280 mV/(m/s^2) であ

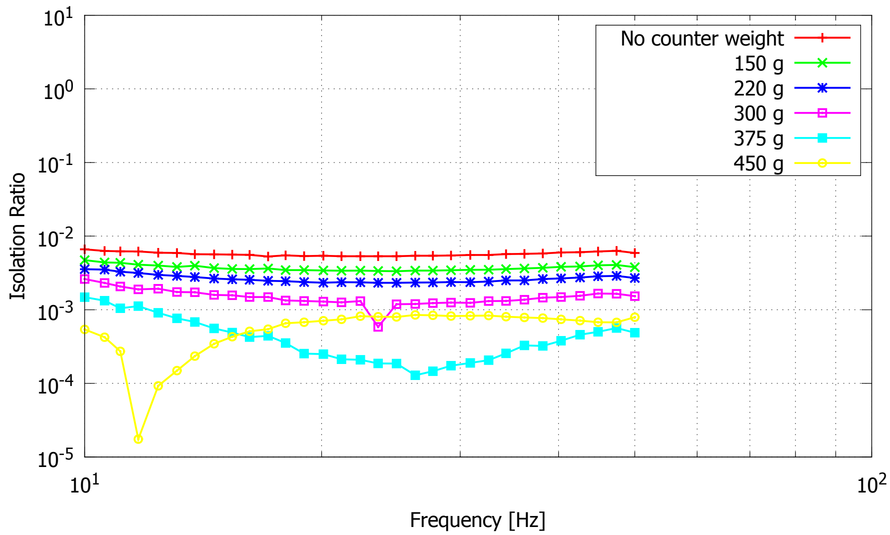

Figure 6.22: カウンターウエイトの重さを変化させた時の倒立振り子の防振比の比較

る。測定には swept-sine 法を用いた。

6.4.2 防振比と magic wand

GAS フィルターの防振性能を向上させるために導入される magic wand の概念を図 6.24 に示す。GAS フィルターに使用される板ばねは質量 m_b および水平軸周りの慣性モーメント I_b を持つものとする。GAS フィルターの中央部に位置する keystone と GAS フィルターのベースを結ぶように質量 m_w, 慣性モーメント I_w の剛体棒がヒンジで接続され、magic wand の片端には質量 M_{cw} のカウンターウエイトが固定される。この系における伝達関数は以下の式で表される [57]。

$$H_{\mathrm{GAS}}(\omega) = 6\frac{\tilde{z}(\omega)}{\tilde{z}_0(\omega)} = \frac{{\omega_0}^2(1+i\phi)-\beta\omega^2}{{\omega_0}^2(1+i\phi)-\omega^2} \tag{6.7}$$

$$\beta = \frac{1}{M}\left[\frac{m_b l_b(L_b-l_b)}{L_b^2} - \frac{I_b}{L_b^2} + \frac{m_w(L^2-l^2)}{4L^2} - \frac{I_w}{L^2} - M_{\mathrm{cw}}\frac{l(L+l)}{L^2}\right] \tag{6.8}$$

ここで M は GAS フィルターが支える質量、$omega_0$ は共振周波数、l_b, L_b, l, L はそれぞれ図 6.24 において定義される長さである。高周波における防振比は $|\beta|$ で飽和する。本試験におけるパラメータを表 6.2 に示す。このパラメータより計算される magic wand が無い場合の防振比の飽和レベルは $\beta \sim 10^{-3}$ である。

6.4.3 測定結果

図 6.26 に GAS フィルターの伝達関数の測定結果を示す。グラフの縦軸は伝達関数の絶対値を表している。Magic wand が無い場合の防振比はおよそ-60 dB で飽和しているが、

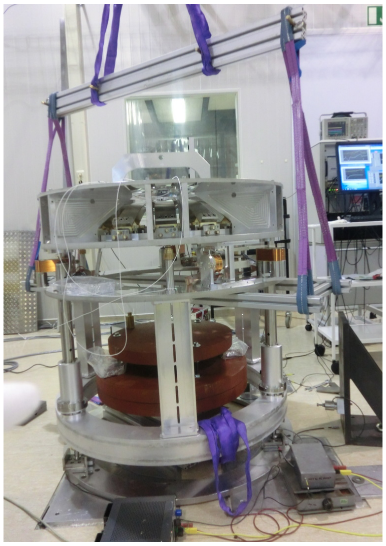

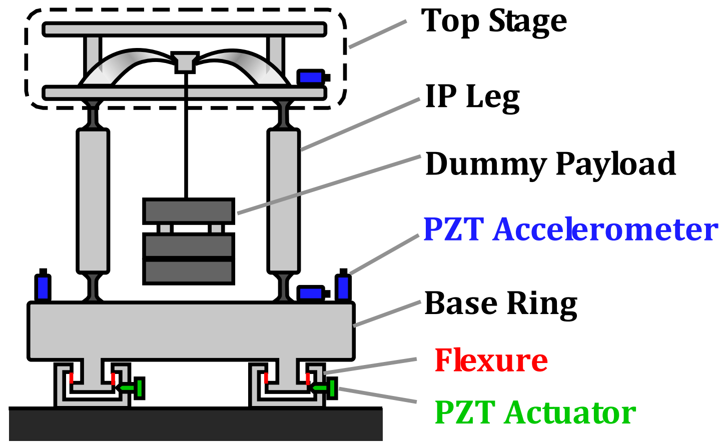

Figure 6.23: GAS フィルターの伝達関数測定のセットアップ

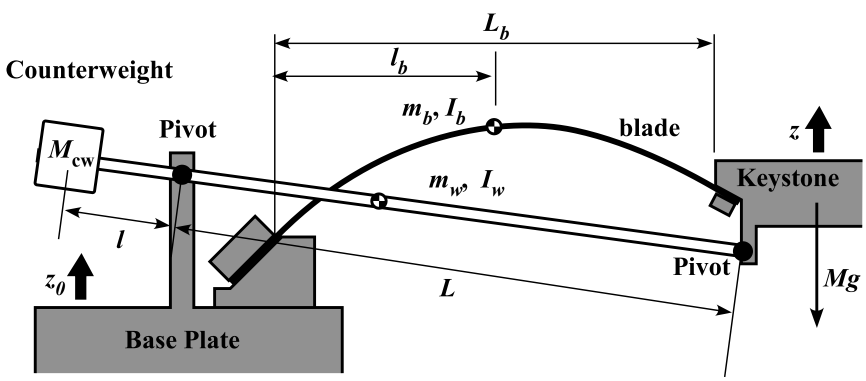

Figure 6.24: Magic wand の概念

M	232 kg
m_b	0.30 × 6 kg
I_b	0.0065 × 6 kg m^2
L_b	245 mm
l_b	90 mm
m_w	0.053 kg
I_w	0.0002 kg m^2
L	280 mm
l	50 mm

Table 6.2: Magic wand に関するパラメータ

Figure 6.25: GAS フィルターに配置された magic wand

カウンターウエイトの調整により

Figure 6.26: カウンターウエイト質量と GAS フィルターの防振比の関係

Type-B SAS prototype

Chapter 7

A prototype of the type-B SAS for KAGRA is assembled and tested in the facility of TAMA300, located in Mitaka Campus of National Astronomical Observatory of Japan. The prototype is made for the purpose of checking the assemblability, vibration isolation performance and controllabilty with digital system, and providing feedback on the actual design of vibration isolation systems for KAGRA.

In this chapter, the experimental setups of the type-B SAS prototype are explained in detail. Section 7.1 describes an overview of the experimental setups and associated facilities. Section 7.2 describes mechanics of the type-B SAS prototype. Section 7.3 describes sensors and actuators for active controls and some auxiliary sensors as observatories. Section **??** describes digital system and design of control servos.

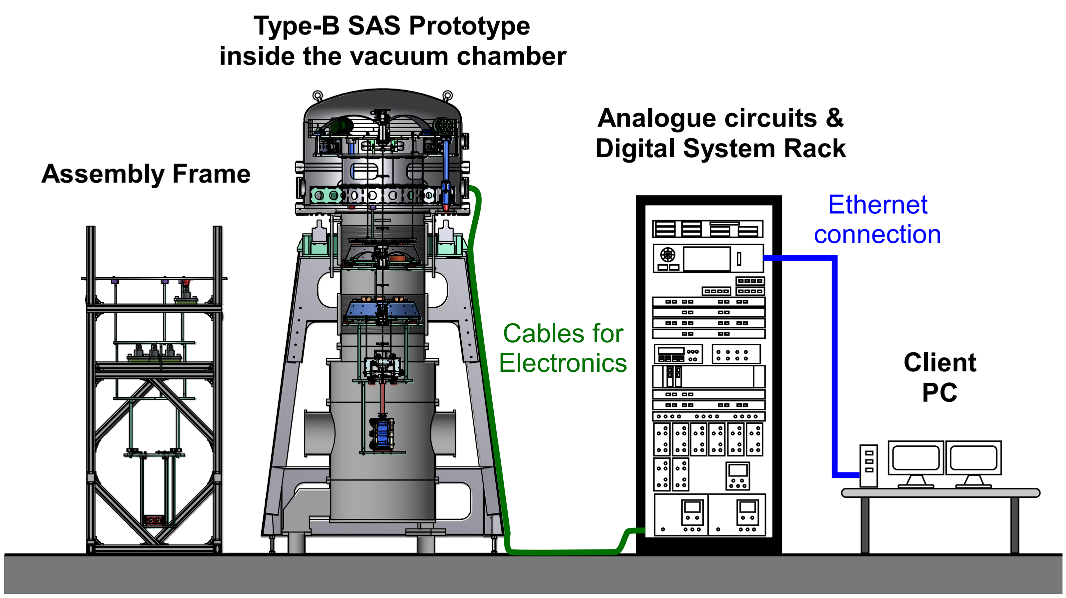

Figure 7.1: A schematic view of the experimental setup for the type-B SAS prototype test.

Figure 7.2: (*Left*) The type-B SAS prototype on an assembly frame waiting for installation into the vacuum chamber on the left. (*Right*) A rack containing digital system and analogue circuits for sensors and actuators. Electrical cables from the suspension system have not been connected yet.

7.1 Overview

A schematic view and pictures of the experimental setup are shown in figures 7.1 and 7.2, respectively. The type-B SAS prototype constructed in TAMA300 is an integration of the vibration isolation components described in chapter **??**. It suspends a dummy mirror made of aluminum instead of an actual mirror made of silica glass. The suspension system contains sensors and actuators for active controls, and auxiliary sensors for the performance check. The signals from the sensors and toward the actuators are integrated into digital system placed next to the type-B SAS prototype. The digital system applies active controls, actuates the suspension for the performance check and stores data of

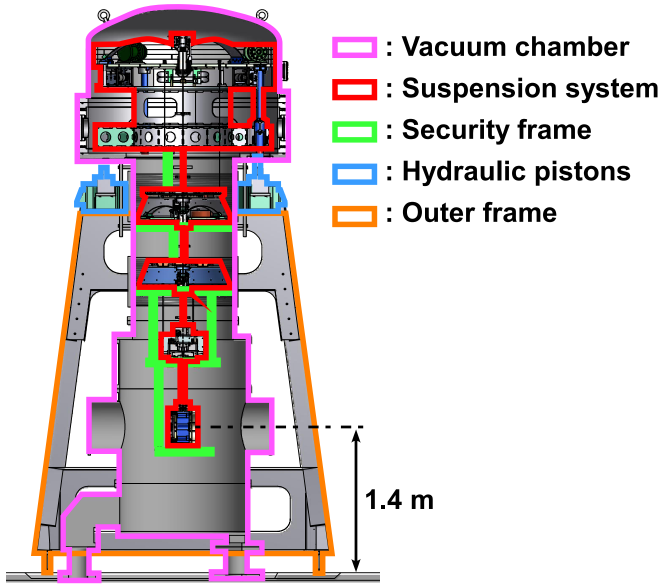

Figure 7.3: A schematic view of the suspension system and surrouding mechanical structures. Respective mechanical components are marked with colored boxes.

input/output signals. The suspension system is assembled on an aluminum assembly frame and then installed into the vacuum chamber. The chamber is evacuated using an oil-free vacuum pump, for reduction of acoustic and air-current noise.

7.2 Mechanics

This section explains the mechanics of the suspension system and related structures. The type-B SAS prototype and surrounding mechanical components are illustrated in figure **??**. The suspension system locates inside the vacuum chamber and holds the dummy mirror at a height of 1.4 m from the ground. A metal frame structure, called the security frame, is constructed around the suspnesion system in order to secure the suspension components in case mechanical failue occurs in suspension wires.

The base of the suspension system, which locates in the middle of the vacuum chamber, is supported by hydraulic pistons from outside the vacuum chamber. The hydraulic pistons are used for adjustment of the tilt of the suspension system base structure. The hydraulic pistons are supported from the ground by a steel frame called the outer frame, which surrounds the vacuum chamber and stands on the ground by four legs.

7.2.1 Suspension system

A picture of the assembled type-B SAS prototype is shown in figure **??**. The bottom three stages of the suspension system, including the dummy mirror or the test mass (TM),

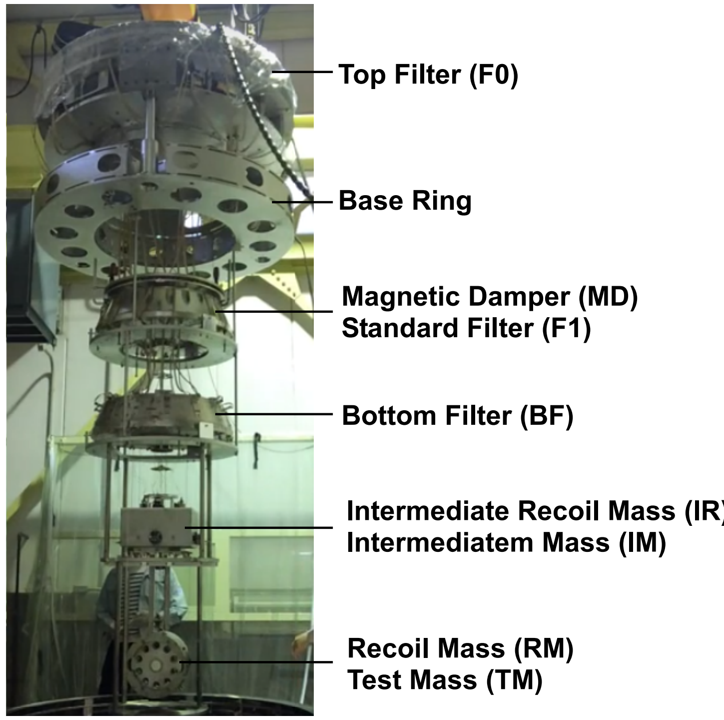

Figure 7.4: A picture of the type-B SAS prototype withdrawn from the vacuum chamber by a crane. The suspension components are fixed to the security frame during the crane operation.

the recoil mass (RM), the intermediate mass (IM), the intermediate recoil mass (IR) and the bottom filter (BF), are the same as the payload prototype described in section **??**. They are suspended from the standard filter (F1) and the from the top filter (F0) by single-wire suspensions. The magnetic damper (MD) is placed above F1 to damp the torsion modes of the single-wire suspensions. F0 is supported from the base structure by inverted pendulum (IP) as described in section **??**.

Suspension wires connecting the suspension components above IM are made of maraging steel. They have nail head structures and are hooked into the masses. The wires are manufactured from rods and turned off into the structure with nail heads. The wires are heat treated after machining to increase the tensile strength.

GAS filters

Three GAS filters implemented in the type-B SAS prototype (F0, F1 and BF) have different numbers of cantilever blades with different dimensions. They are designed so that their optimal loads fit with the weight of their payloads. Table 7.1 shows parameters of the cantilever blades and measured properties of the GAS filters.

Resonant frequencies of GAS filters are tuned beforehand by changing the radial compression of cantilever blades. They are set between 0.3 and 0.5 Hz, so that the filters provide enough isolation performance but do not suffer from hysteretic behavior as described in section **??**. The magic wands (see **??**) are not attached to them.

		BF	SF	TF
Thickness	[mm]	2.4	2.4	5.0
Width	[mm]	35.3	80.0	125
Length	[mm]	274	274	606
Number of blades		3	4	3
Optimal load	[kg]	50.1	165.2	276.2
Resonant frequency	[Hz]	0.44	0.38	0.33

Table 7.1: Parameters on the GAS filters used in the type-B SAS prototype. Upper four raws describe the parameters on cantilever blades and lower two raws desribe measured properties of asesmbled GAS filters.

Mass distribution

Since GAS filters only work when appropriate loads are applied, the mass of each stage in the suspension system must be adjusted in ∼0.1 kg precision. Fine tuning of the weight distribution is achieved by attaching small metal discs (same as used in section **??**) on the suspended components. The discs are also used to balance the tilt of each stage with their horizontal positions. The mass distribution of the type-B SAS prototype is shown in table 7.2.

	Mass [kg]	Sum [kg]	Note
TM	11.1		
RM	12.5		
IM	26.5	50.1	Load of BF
IR	8.1		
BF	107.0	165.2	Load of F1
F1	111.0	276.2	Load of F0
MD	17.8		
F0	545	839	Load of IP

Table 7.2: Mass distribution of the type-B SAS prototype. Mass of each stage is tuned so that the loads on GAS filters and IP are optimized.

Tuning of inverted pendulum

The diameters of the bottom flexure joints of IP are originally 10.50 mm and the corresponding critical load is 1080 kg as described in section **??**. Weight of F0 is 300 kg without ballast masses, while the required weight of F0 to operate IP with low resonant frequencies is ∼500 kg in addition. This is huge and there is no enough space on F0 to place such big amount of ballast masses.

Thence the flexure joints of IP are trimmed into the diameters of 9.70 mm by a turning machine, which reduces the critical load of IP into ∼845 kg. The weight of F0 is adjusted ∼545 kg so that resonant frequencies of the translation modes becomes ∼80-100 mHz.

Tuning of magnetic damper

Simulation shows that damping coeffecients between MD and F1 about yaw motions should be set ∼2 [Nm/(rad/sec)] for efficient damping of torsion modes of single-wire suspensions (see section **??**). From the results of damping strength measurement (section **??**), number of cubic magnets attached to MD is set 72 and the distance between MD and the copper plate on SF is set 5 mm.

7.2.2 Security frame

Figure 7.5 shows an illustration of the security frame designed for the type-B SAS prototype. Below each stage of the suspension chain, there placed a metal disc to secure the suspended masses in case they drop due to mechanical failure in suspension wires. The discs holds range limiter which restricts the displacement of the suspended mass into few millimeters during the operation. They also contain locking mechanism used when the assembled system is transported.

Discs are connected to the IP base by metal pillars with enough thickness so that they can hold the weight of suspension system in case of accidents. Basically the diameters of the pillars are set 25 mm in design. However, in the prototype test, the diameters of the pillars connecting upper two stages are reduced to 15 mm, because of limited space in the vacuum envelope. The resonant frequency of the lowest-order mode is as low as 3 Hz according to an FEM simulation (see figure 7.5). The frequency increases to 7 Hz when the pillars on the two stages are replaced to those in 25 mm diameter. Although the flexibility of the security frame does not affect the vibration isolation performance of SAS itself, its vibration may introduce scattered light noise in the interferometer and must be treated carefully in the actual system.

7.2.3 Vacuum envelope

The vacuum envelope for the type-B SAS prototype consists of two vacuum chambers and metal bellows connecting them. The bottom chamber, housing the payload part of the suspension system (below BF), is a reuse of the vacuum chamber for the end test mass

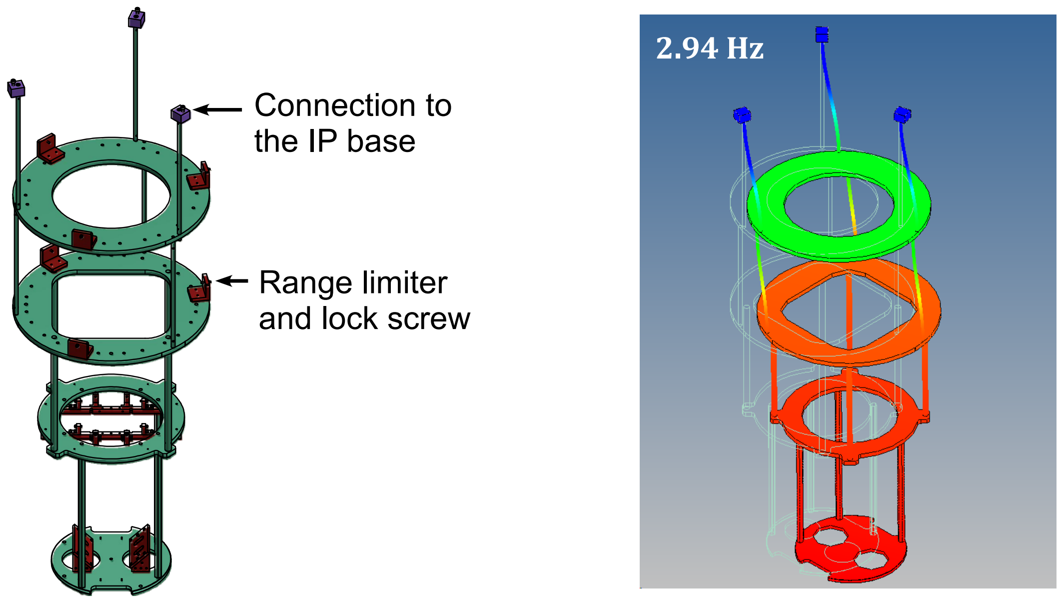

Figure 7.5: An illustration of the security frame for the prototype system (*left*) and its lowest-order resonant mode shape (*right*).

of TAMA300 [?]. It has several ducts with viewports, so the suspended mirror can be monitored from outside the chamber. An optical lever to monitor the TM angle is also implemented by using one of these ports (see section **??**).

The top chamber of mashroom shape is newly manufactured for the prototype test. It has an inner diameter of 1500 mm and contains F0 and the base ring structure of the suspension system. It has several ducts with feedthroughs on side to derive the signals from sensors and toward actuators outside the vacuum chamber. The top and bottom chambers are connected by metal bellows with an inner diameter of 800 mm. The bellows contain F1 and BF inside. The structure of the bellows is strengthen by four threaded tie-rods to hold the weight of the top chamber. Length of the bellows is adjusted for positioning the top chamber in an appropriate height with respect to the base of the suspension system.

On the bottom surface of the top chamber, there are three ports for mechanical connection of the suspension system inside the vacuum with the hydraulic pistons outside the vacuum. Figure 7.6 shows an extended view around the boundary between the base of the suspension system and a hydraulic piston. The suspension system base is supported by cone shape adapters placed just below IP legs, and each adapter sits on a hydraulic piston. The adapters are welded to small metal bellows which separates the vacuum and air parts.

The small bellows works as mechanical isolators separating the vibration of the suspension system from that of the vacuum chamber. Since the vacuum chamber has huge mass and its support is not robust, vibration of the chamber tends to be enhanced by me-

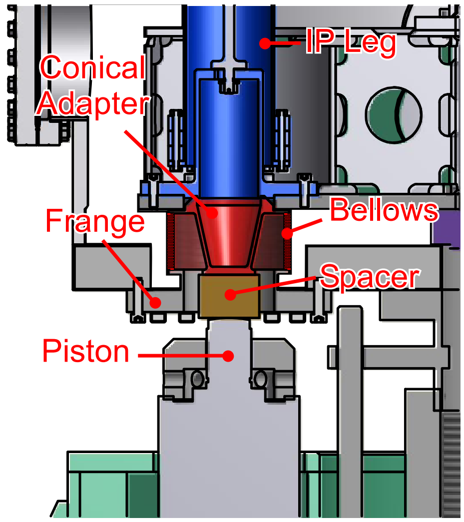

Figure 7.6: An extended view of the boundary between the suspension system base and a hydraulic piston.

chanical resonances at low frequencies (few Hz) and it tends to be an antenna of acoustic noise. This may degradate performance of SAS and thus mechanical isolation between the chamber and the suspension system is mandatory.

7.2.4 Outer frame

The ground vibration is transmitted to the suspension system through the outer frame surrounding the vacuum chamber. The rigidity of the outer frame is essential since its mechanical resonances can enhance the vibration of the suspension system base and degradate the vibration isolation pefromance. In addition, flexibility of the outer frame causes back-action in the actuators on F0, and thus can cause instability of active controls. It is important to push the resonant frequencies as high as possible, at least higher than the bandwith of the IP active controls ($\sim$ 1 Hz). According to an FEM simulation on the currently designed outer frame, the resonant frequency of the lowest-order resonant mode (the mode shape is illustrated in figure 7.7) is $\sim$8 Hz, assuming 1400 kg load on top of the frame.

Figure 7.8 shows measured vibration spectrum on top of the outer frame, compared with that on the floor. Amplitude ratio of two spectra is also shown in the lower graph. The measurement shows that, in high frequency region, the amplitude of the outer frame vibration gets 1-2 orders of magnitude larger than that of the ground vibration, due to mechanical resonances and pickup of acoustic noise. A large peak at 8.8 Hz would correspond to the lowest-order resonant mode of the outer frame.

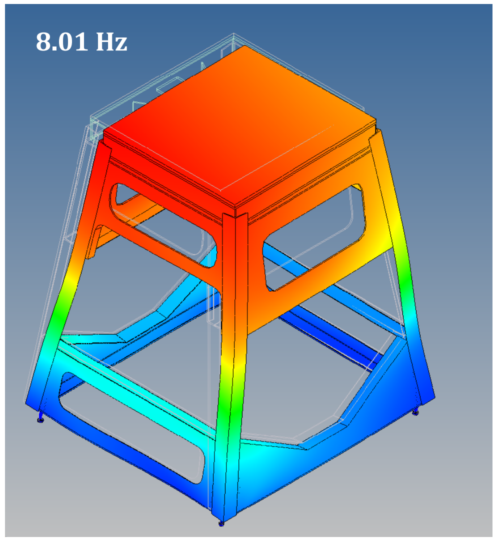

Figure 7.7: An illustration of the lowest-order resonant mode of the outer frame predicted from an FEM simulation. The simulation assumes $\sim$ 1400 kg load on top of the frame.

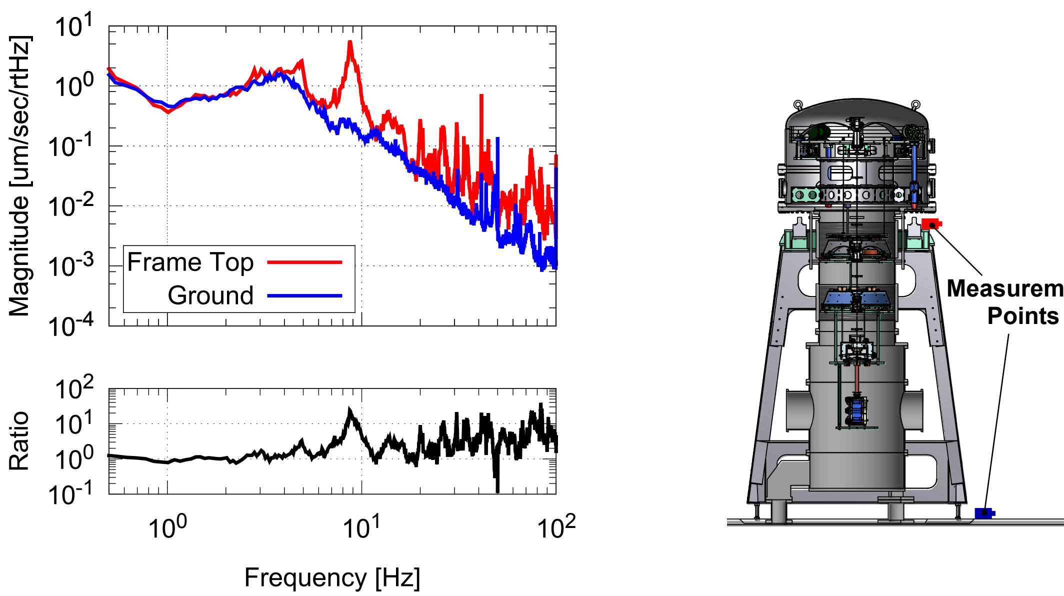

Figure 7.8: Comparison of horizontal vibration spectrua on the floor and on top of the outer frame in velocities, measrured by a geophone L-4C. Amplitude ratio of two spectra ($\tilde{x}_{\text{frame}}/\tilde{x}_{\text{floor}}$) is shown in the lower graph.

7.3 Sensors and actuators

A bunch of sensors and actuators are used in the prototype test for controlling and characterizing the suspension system. Sensors and actuators are categorized into three groups depending on purposes of their use.

For initialization.
The sensors and actuators in this group are used for DC positioning and alignment of suspension components. They are used only in the initial setup or for the recovery after large disturbances like big earthquakes. They are not used during the observation and are often switched off to avoid noise injection.

For active controls.
The sensors and actuators in this group are used for active vibration controls of the suspension system. The noise level should be cared since they may introduce vibration on the suspension components through the controls.

For characterization.
The auxiliary sensors and actuators in this group are and only used for the characterization of the suspension system and surrounding environment. Some of them are not implemented or are replaced with other ones in actual KAGRA detector.

Details about the sensors and actuator implemented in individual suspension components are explained in chapter **??**. This section describes sensors and actuators not explained in the previous chapter, some devices for vacuum operation and controllability as an integrated system.

7.3.1 Actuators for positioning and alignment

Actuators for initial positioing and alignment of the suspension components are summarized in table 7.3. They are used for relative positioing and alignment between suspension bodies, to avoid mechanical contact between them. They are used for DC positioning and alignment of TM (with respect to the interferometer beam in the actual detector),

The three hydraulic pistons implemented below the suspension system base (see section **??**) are used for arranging equillibrium points of IP and the height of the whole suspension system. The horizontal DC position of F0 is adjusted by the motorized sliders (see section **??**) and it also determines the horizontal DC position of TM.

Adjustment of the vertical DC position of TM is achieved by using the fishing rod (described in section **??**) implemented in F1. The fishing rod implemented in F0 arranges the relative DC position between MD and F1, which determines the damping strength between the two bodies. Although the BF fishing rod is not implemented in the prototype test due to lack of attachment mechanisms, it should be used for tuning relative DC position of IM and IR vertically. In the prototype test, this positioning is achieved by applying DC current to the actuator coil on BF. Applying much DC current to actuator

Position	Name	Actuated DoF	Main purpose
Base	Hydraulic pistons	LF0, TF0, YF0	Make IP in operation state.
			Rough vertical positioning of TM.
F0	Motorized sliders	LF0, TF0, YF0	Horizontal positioning of TM.
	Fishing rod	VF1	Relative positioning of F1 and MD.
	Rotation mechanism	YF1	Alignment of TM in yaw.
F1	Fishing rod	VBF	Vertical positioning of TM.
BF	(Fishing rod)	(VIM)	(Relative positioning of IM and IR.)
	Moving masses	PBF, RBF	Relative alignment of IM and IR.
	Rotation mechanism	YIM	Relatiev alignment of IM and IR.
IM	Moving masses	PIM, PTM	Alignment of TM in pitch and roll.

Table 7.3: Actuators for initial positioning and alignment of the type-B SAS prototype. The BF fishing rod is not implemented in the prototype due to lack of attachment mechanism, but will be implemented in the actual system.

coils should be avoided in terms of noise injection and heating problems, so the BF fishing rod will be implemented in the actual detector.

The DC pitch and roll angles of TM are controlled by the moving masses with picomotors on IM, as described in section **??**. The moving masses are also implemented on BF, while they are used for relative alignment and horizontal positioning between IM and IR. The alignment of TM in the yaw angle is achieved by the rotation mechanism with a picomotor implemented in the keystone of F0. The rotation mechanism is similar to that implemented in the keystone of BF (see section **??**). The rotation mechanism on BF is used for taking relative alignment between IM and IR.

In the prototype system, no interferometer beam exists and therefore DC position and alignment of TM is adjusted to a different standard. The motorized sliders on F0 are adjusted so that F0 comes in the nominal center (where all the LVDT signals on F0 are nulled). The fishing rod on F1 is adjusted so that the keystone comes in the nominal working point (where the resonant frequency is minimized). The DC pitch and yaw angles of TM are adjusted to the optical lever so that the beam spot comes in the center of the QPD.

7.3.2 Sensors and actuators for active controls

Sensors and actuators for active controls are summarized in table 7.4. The LVDT, geophone and coil-magnet actuators implemented on F0 in horizontal directions are used for the IP control. On the keystones of GAS filters, LVDTs and coil-magnet actuators are implemented in vertical directions and are used for damping and thermal-drift compensation of GAS filters. OSEMs, units of optical sensors and coil-magnets actuatros, are implemented on the IM and TM levels for active damping of mechanical resonances of the

Position	Name	Sensed/actuated DoF
F0	LVDT+Act	LF0-LGND, TF0-TGND, YF0-YGND
	Geophone	LF0, TF0, YF0
	LVDT+Act	VF1-VGND
F1	LVDT+Act	VBF-VF1
BF	LVDT+Act	VIM-VBF
IM	OSEM	LIM-LIR, TIM-TIR, VIM-VIR
		RIM-RIR, PIM-PIR, YIM-YIR
TM	OSEM	LTM-LRM, PTM-PRM, YTM-YRM
	Optical lever	PTM, YTM

Table 7.4: Sensors and actuators used for active controls of the type-B SAS prototype.

bottom parts. An optical lever is implemented to monitor the alignment of TM about yaw and pitch rotation.

Optical lever

A schematic view and a picture of the optical lever setup are shown in figures 7.9 and 7.10 respectively. The opical setup is similar to the setup used for the payload test (see section ??). The fiber-collimated light from an SLD is injected to the aluminum-coated mirror placed at the center of TM, and the reflected light is guided to a QPD on an XZ stage. A half mirror is inserted between TM and the QPD, which works as an attenuator to adjust the light power injected to QPD. The launcher after collimation and the QPD are placed as close as to the viewports possible for aircurrent noise reduction. The optics outside the chamber are covered by a paper windshield for the same purpose.

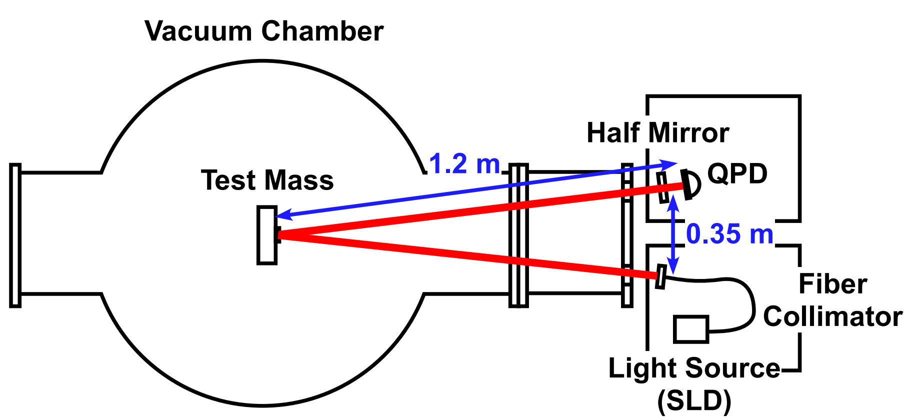

Figure 7.9: A schematic drawing of the optical lever setup.

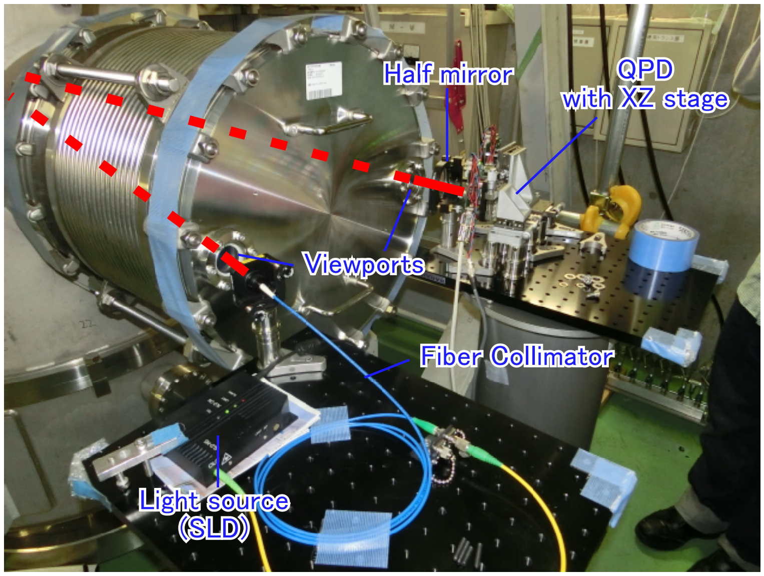

Figure 7.10: A picture of the optical lever setup. The optics shown in the picture will be covered by a windshield for air-current noise reduction.

The optics are horizontally arranged on optical tables at the level of TM. The cylindrical supports for the optical tables are made of aluminum to have good thermal conductivity and reduce the tilts of the optical tables due to thermal inhomogeneity in the supports. The lowest mechanical resonant frequency of a support is around 50 Hz, which is much higher than the bandwith of the optical lever controls (∼1 Hz).

Vacuum pod for geophone

Since the geophone L-4C and its preamp are not vacuum compatible, they are packed in vacuum pods made of stainless steel (see figure 7.11) and their insides are kept in atmospheric pressure. Air leaks from the vacuum pods are checked beforehand in a small vacuum chamber and are proved to be small enough to be operated in vacuum at least for several months.

7.3.3 Auxiliary sensors

Several additional sensors are implemented for characterization of the prototype system. Figure 7.12 shows their disposition.

Thermometer

Two thermometers are installed to monitor the temperature of the environment and the suspension system. One of them is placed outside the vacuum chamber to measure the air temperature, and the other is attached to the base ring of the suspension system inside

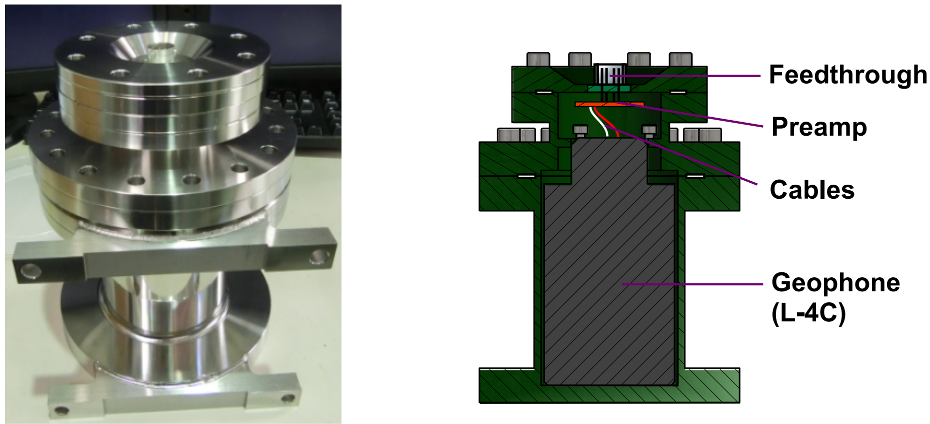

Figure 7.11: A picture of a vacuum pod for the geophone L-4C and its cut view drawing. In the picture the pod stands vertically, but is implemented on F0 horizontally in actual.

the vacuum chamber. The thermometers utilize temperature sensors LM45 [?], whose output voltage is linearly proportional to the Centigrade temperature. The output voltage of LM45 is enhanced by an amplifier circuit whose DC gain is set 10.

Seismometer

A geophone L-4C is placed on top of the outer frame to monitor the seismic vibration injected to the suspension system. The output voltage from the geophone is enhanced by a preamp as other geophones.

Photosensor

The longitudinal displacement of TM is monitored by photosensors attached to the security frame. Figure 7.13 shows pictures of the photosensors and the detection mechanism. Note that the photosensors detect the relative displacement between TM and the secirity frame, while OSEMs on TM detect the relative displacement between TM and RM.

The photosensors adopt a detection scheme used for the space gravitational wave antenna SWIM$\mu\nu$ [?]. The target object (the back surface of TM) is illuminated by an LED and the reflected light is detected by two photo detectors (PDs) placed next to the LED. The total power detected by two PDs depends on the distance between the sensor and the target. Symmetric configuration is adopted for the purpose of omiting the detector's sensitivity to the the target inclinement.

Displacement of the TM centeral point cannot be measured directly due to existence of a central hole on TM. Therefore two photosensors are placed with horizontal seperation and the average of two sensor readouts is used as a displacement readout of TM. Since the positioning of two photosensors is not accurate, the displaement readout can suffer from the coupling from TM yaw motion by $\sim$5 [mm/rad] at most.

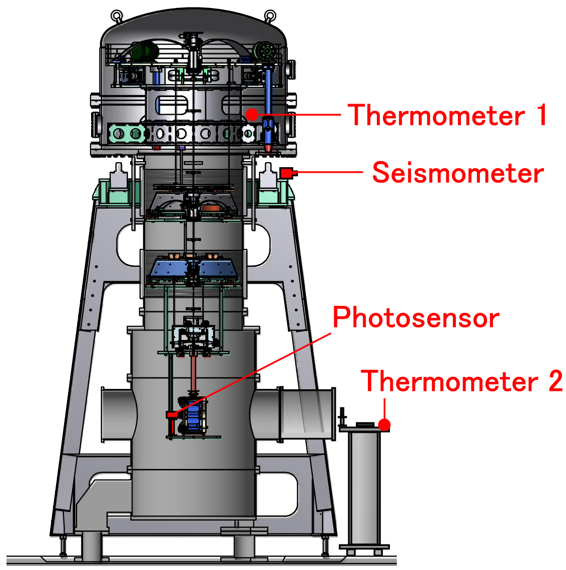

Figure 7.12: Disposition of auxiliary sensors for characterization of the prototype system.

Figure 7.14 shows the calibration result of one of the photosensors. The calibration is done by arranging the distance between an aluminum target and the photosensor with a micrometer stage. The sensor output voltage increases as the target goes away from the sensor until the distance reaches 5 mm. Then the voltage decreases if the target goes further away Although the response is non-linear in a global regime, a linear response is obtained in the distance between 2-3 mm and the obtained sensitivity is 2.65 V/mm.

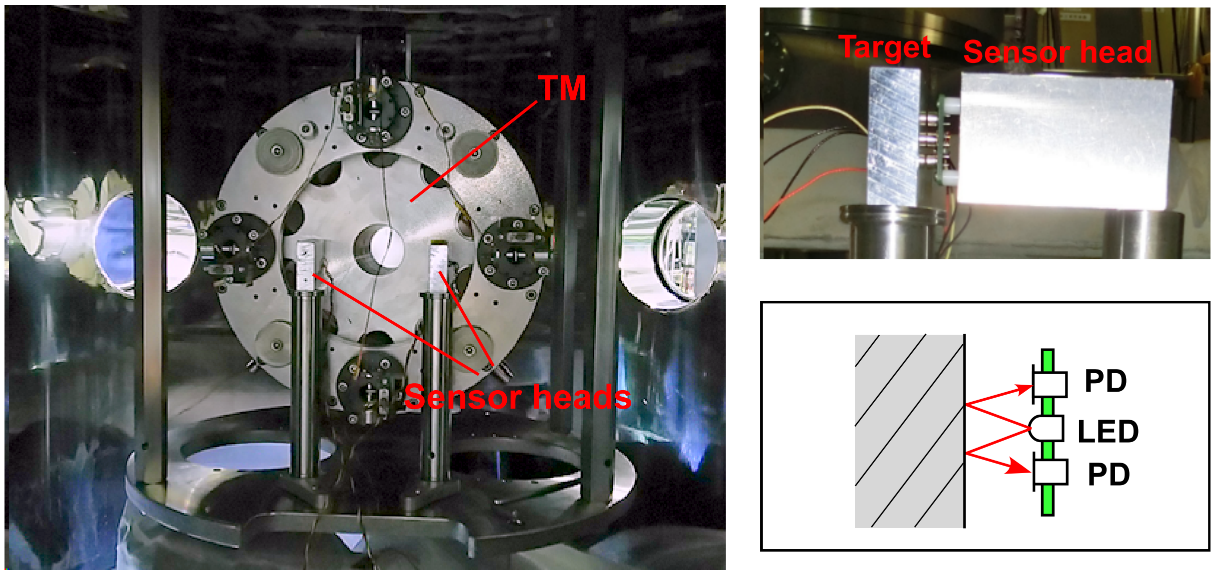

Figure 7.13: (*Left*) A picture of the photosensors installed to the suspension system. (*Right*) A closer look at a photosensor during the calibration and an illustration of the detection mechanism.

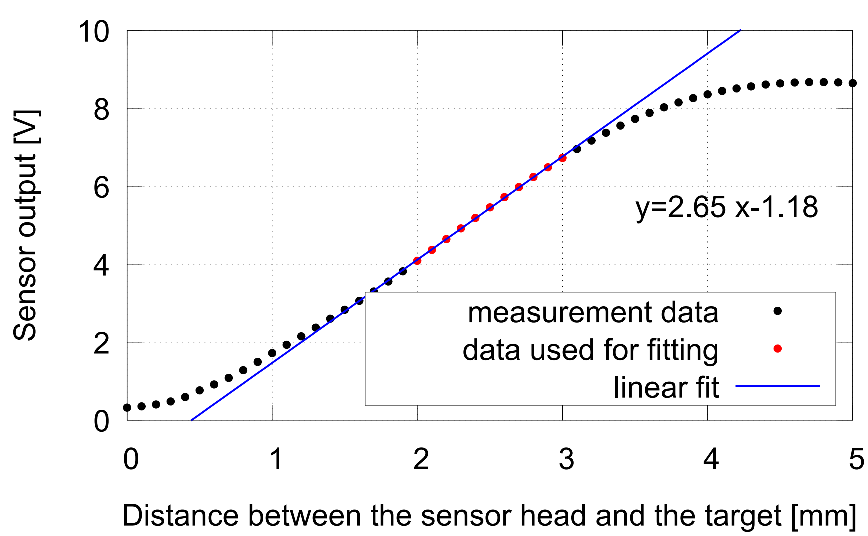

Figure 7.14: A calibration result of one of the two photosensors.

7.3.4 Cabling

Electrical cables from the sensors and actuators for the suspension system are guided upwards and collected to the feedthrough on the top chamber. The cables are anchered to suspension stages and arranged loosely so as not to provide significant mechanical stiffness between them (see figure 7.15). Twisted-paired ribbon cables are used for carrying the electrical signals inside the vacuum chamber. They are plugged into 9-pin D-sub connectors on the feedthrough. Outside the chamber, the signals are carried to the rack containing digital system and electrical circuits by commercial 9-pin D-sub cables with electromagnetic intereference shieldings.

Figure 7.15: A picture displaying electrical cables between BF and F1. Rainbow-colored ribbon cables are clamped to the suspension stages and arranged loosely between them.

7.4 Digital control

Active controls of the suspension system require complicated Multiple Input Multiple Output (MIMO) control loops and switching servo filters depending on the situation. It is unrealistic to achieve such controls only by analogue circuits with manual operation and thus digital control system is required. The digital system also plays a role in storing data of signals, creating excitation signals for suspension system characterization, and automatizing control procedures which are routinely and frequently used.

7.4.1 Digital system overview

The digital system implemented in the type-B SAS prototype is basically an import from the LIGO detectors, which will be also adopted in the KAGRA detector for the interferometer control and data storage.

Real-time signal processing for the digital control is performed by a real-time OS machine custamized for highspeed signal processing and data communication. The signal processor is connected to a PCIe extension board which contains a timing clock, Analog-to-Digital Convertors (ADCs) and Digital-to-Analog Convertors (DACs). The real-time data of selected signals are stored in a 1 TB data storage hard-disc. Detailed contents of signal processing are implemented and controlled from a Scientific Linux machine connected to the real-time machine through a Local Area Network (LAN). Table 7.5 shows the specification of the digital system used in the prototype test.

Figure 7.16 shows a typical flow of signals processed by the real-time signal processor. Signals derived from numerous sensors are sent to the ADCs and digitized. The signals are passed to the processor in which a number of Infinite Implulse Response (IIR) filters, matrices, offsets and excitation signals are applied. After being processed, the signals are sent to DACs and converted to analog signals for the actuation of the suspension system.

The internal variables of the signal processor, such as feedback gains, coefficientes of the IIR filters and amount of the offsets, are controlled with the system called EPICS (Experimental Physics and Industrial Control System) [?], which communicates with the real-time system at 64 Hz. The EPICS variables can be rewritten from an interface computer easily, which enables a user to program various control sequences with computer language scripts.

Digital system requires signal conditioning filters called anti-aliasing (AA) and anti-imaging (AI) filters as analog circuits. They cut off the signals at frequencies higher than the Nyquist frequency to mitigate noise caused by quantization errors. The anti-aliasing and anti-imaging filters implemented in the prototype system are identical circuits, which have third order low-pass filters with 10 kHz cutoff and notch filters at 65536 Hz.

7.4.2 Loop delay and digitization noise

Although digital system provides significant flexibility and usability, the bandwith of the digital control is limited typically by one or two orders of magnitude less than the sampling frequency, because of time delay in the computing process. Figure ?? shows a transfer function from a digital system output to an input, when they are connected directly by an electrical cable. The transfer function includes the responses of analog AA

Item	Spec
Sampling rate	16384 Hz (sampled at 65536 Hz, decimated to 16384 Hz)
Number of ADC channels	64 ch. (with 2 ADC cards)
Number of DAC channels	32 ch. (with 2 DAC cards)
ADC/DAC bit resolution	16-bit = 65536 digital counts
ADC voltage range	$\pm$20 V (1 count = 0.61 mV)
DAC voltage range	$\pm$10 V (1 count = 0.31 mV)
ADC noise level	3 μV/$\sqrt{\text{Hz}}$ (> 10 Hz)
DAC noise level	2 μV/$\sqrt{\text{Hz}}$ (> 10 Hz)
Through delay	80 μsec

Table 7.5: Specification of the digital system for the type-B SAS prototype test.

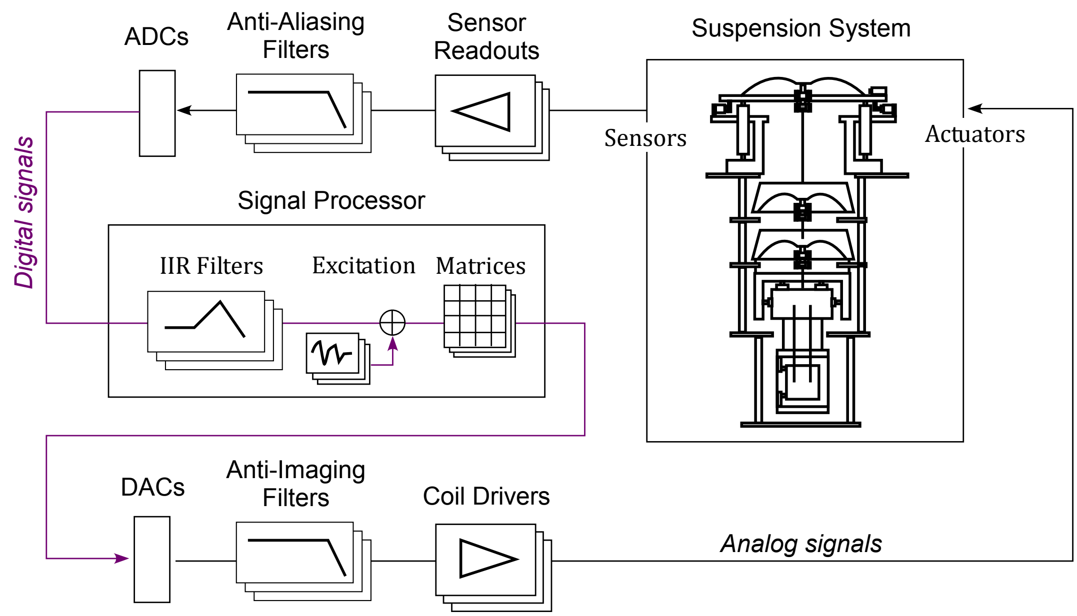

Figure 7.16: Block diagram of the real-time system for the suspension system controls.

and AI filters, while the cut-off at 5 kHz is caused by a software AA/AI filter implemented in the digital system. The measured phase delay is 15 deg. at 100 Hz and 45 deg. at 300 Hz. The measurement indicates that control signals are subjected to group delay of ∼420 μsec through the digital system.

So the control bandwith is limited by few hundred Hz using the digital system. However, this is not a problem in suspension active controls, because a typical control bandwith is few Hz at most and is much lower than the limitation.

Another drawback of using digital control is to suffer from larger sensing and actuation noises due to quantization errors in digitization processes. The power spectrum density of the quantization noise is estimated by the following formula [?].

$$P_{\rm n}(f) = \left(\frac{\Delta^2}{12}\right)\frac{2}{f_s}. \tag{7.1}$$

Here Δ is the step size of quantization and f_s is the sampling rate. In the prototype system, the noise level of the ADC is estimated to be 2 μV/$\sqrt{\rm Hz}$, while the measured noise level is 3 μV/$\sqrt{\rm Hz}$ at high frequencies and increases by $f^{-1/2}$ below 3 Hz as shown in figure ??. This is huge compared with the typical noise level of analog circuits (in the order of nV/$\sqrt{\rm Hz}$).

Although not implemented in the prototype test, the impacts from ADC and DAC noise can be mitigated by introducing whitening and dewhitening filters in analog circuits. Whitening filters enhance the sensing signals before injected to ADCs and dewhitening

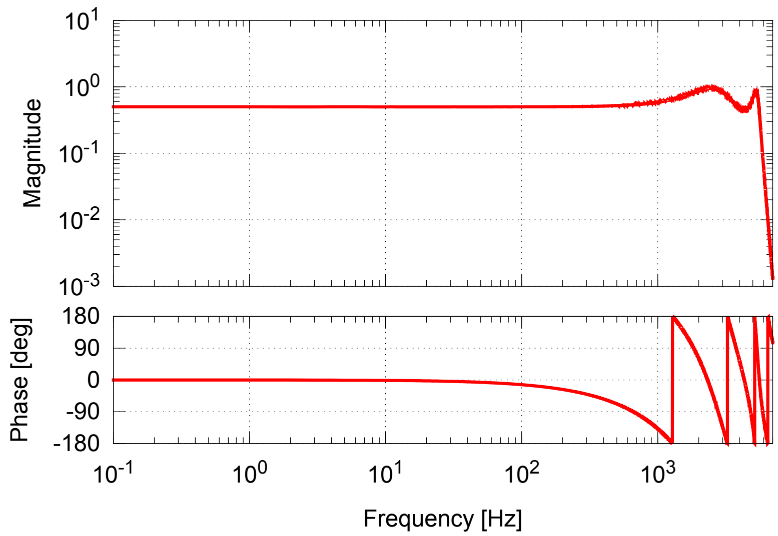

Figure 7.17: A loop-delay of the digital system measured with connecting an AA filter input and an AI filter output directly.

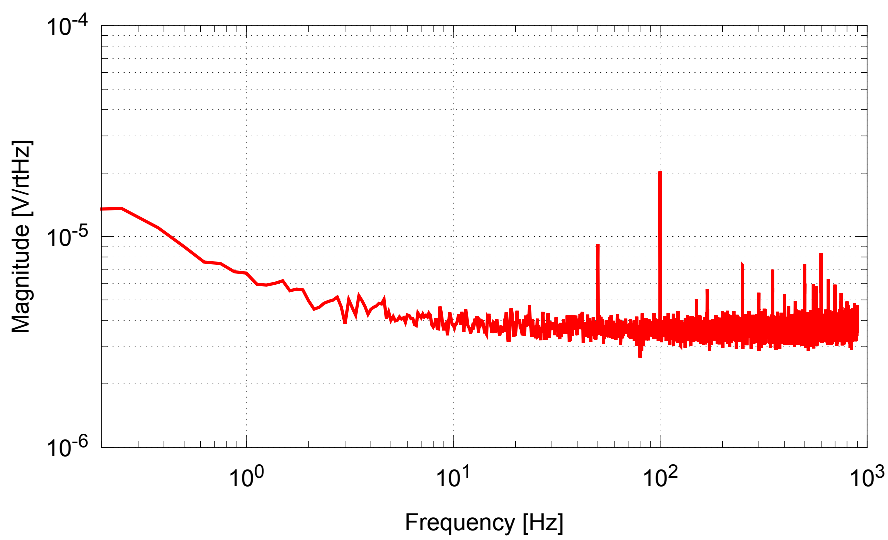

Figure 7.18: A typical noise spectrum of ADCs.

filters diminish the actuation signals after DACs, at frequencies where sensitive controls are required. The phases and loop gains are compensated by anti-whitening and anti-dewhitening filters implemented in digital system. Signal-to-noise ratio around the frequencies of interest is improved by this method, while the controllable range also decreases at those frequencies.

7.4.3 Signal processing

Figure 7.19 shows overview of the signal processing part for the digital control of the type-B SAS prototype. The sensing signals from LVDTs and geophones on F0, OSEMs on IM and TM, and LVDTs on GAS filters are used for the main streams of the active controls. The signals after being processed are fed back to the coil-magnet actuators on corresponsing stages. The signals from the optical lever and photosensors are processed in side streams, and the correction signals from these sensors are added to the actuation signals for IM and TM respectively. The signals from environmental sensors are processed by multiplying calibration factors and keep flowing in the data streams. The sensing signals including the signals from environmental monitors and feedback signals are stored in the data storage after down-sampled to 256 Hz.

Figure 7.20 shows a typical flow in the signal processing part for active controls of the suspension system. Raw signals from sensor readouts injected to ADCs are muliplied by calibration factors, which are measured beforehand, and converted to displacements or velocities at the sensing points. The real sensor signals are then transformed into virtual sensor signals, which describe the rigid-body motions of the suspension bodies in the Euclid coordinate system. This transformation is done by multiplying a sensor matrix whose elements are determined from geometric layout of sensors. When several kinds of virtual sensor signals are available for the same reconstructed DoF, the measurements are blended into a super sensor signal. This sensor blending scheme is used for the controls of the top stage motions which are measured by two different kinds of sensors; LVDTs and geophones. The super sensor signal is constructed by multiplying a lowpass filter $L(s)$ to the LVDT signal and a complimentary highpass filter $H(s) = 1 - L(s)$ to the geophone signal.

The virtual sensor signals are then injected to the servo systems in the signal processor. The sensor signals are firstly applied with offsets, which determines the DC operation points of the suspension bodies, and then applied with servo filters to obtain feedback signals. The control gains are switched between 0 and -1, which determines the active controls ON or OFF. The digital system can alter the control gains and offsets gradually so that the system transits to different control states smoothly.

The digital system can inject excitation signals in arbitrary points of the signal paths. When the characterization of the suspension system is performed, excitation signals are injected just after the servo filters so that the motion of a certain DoF is excited. The control signals from the optical lever and photosensors are also added to this point. Though the photosensors are explained to be observatory sensors for characterization, the signals

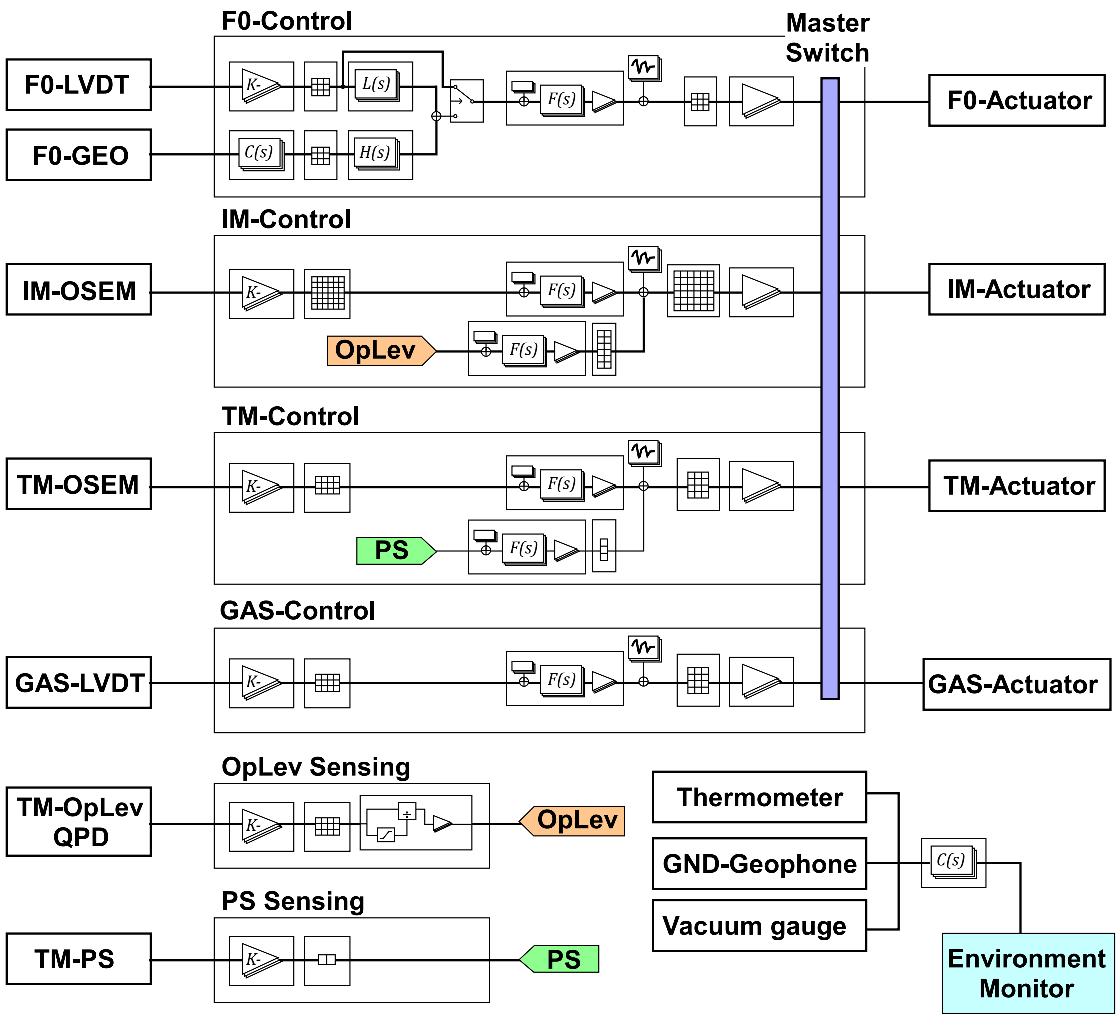

Figure 7.19: Overview of digital control and environmental monitor system.

are fed back to the actuators to demonstrate the lock of the interferometer (see section ??).

The virtual actuator signals from the servo system are then converted to the real actuator signals using a coil matrix. Coefficients of the coil matrix are determined from the results of actuator diagonalization, as described in section ??. The actuator signals are then injected to output filters, in which the sign of output voltage is compensated by multiplying ± 1, depending on the direction of coil windings and magnet poles. The master switch, placed after the output filters, regulates all the digital output and is switched off in case of accidents.

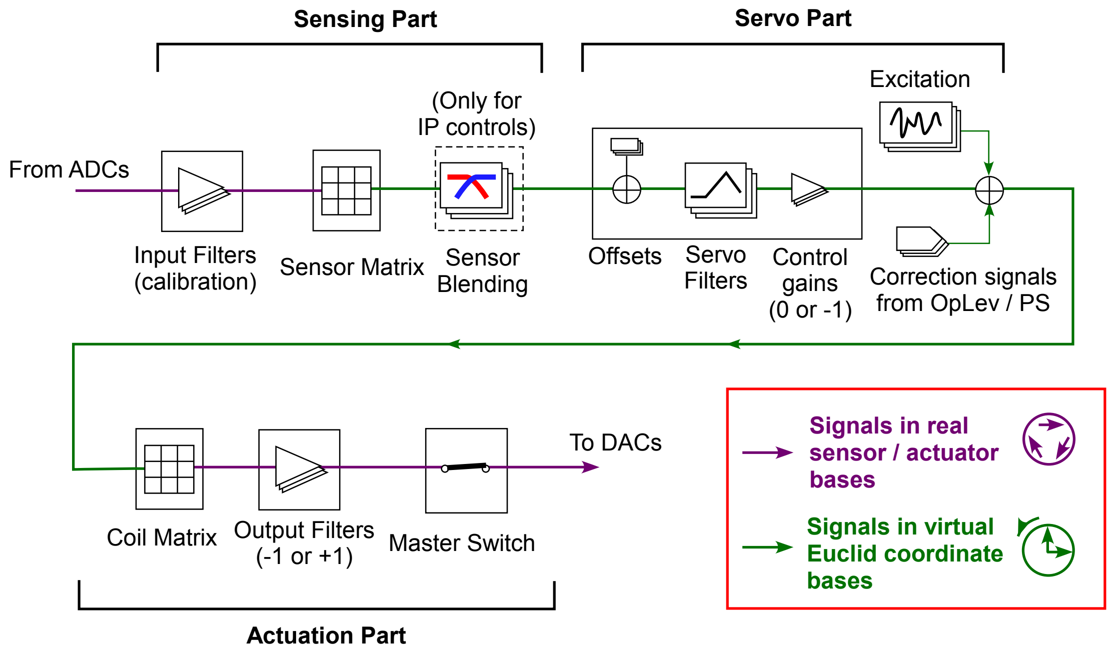

Figure 7.20: Block diagram of the signal processing in the digital system.

7.4.4 Motor controls from digital system

Number of stepper motors and picomotors implemented for DC positioning and alignment of the suspension system are controlled from the digital system through EPICS. Stepper motors are drived by using a TMCM-6110 controller/driver board [?], which supports up to 6 bipoler stepper motors and has various communication interfaces for digital controls. The TMCM-6110 board is connected to the digital system LAN with RS485 (2-wire) serial interface, through an Ethernet-serial convertor NPort 5110A [?]. Picomotors are drived by using a Newport / New Focus 8752 Picomotor Controller and slaved 8753 Picomotor Drivers [?], and the controller is connected to the digital sysytem LAN through an Ethernet cable.

The digital system communicates with the motor controllers using PyEpics [?], the EPICS Channel Access protocol interfaced by Python programming language. The direction, speed and amount of rotation are controlled through the program. Motors can be activated simultaneously and thus it is possible to move the suspension stage in a certain DoF by distributing rotation angles accordingly.

Performance test of type-B SAS prototype

Chapter 8

This chapter mentions the experimental results on the performance test of the KAGRA type-B SAS prototype, whose setups are describes in the previous chapter. The primary motivation of the experiment is to demonstrate the active controls of the suspension system and confirm their stability and feasibility.

In sec. 8.1, the mechanical response of the suspension system is checked with implemented sensors and actuators, before having active controls. Measured frequency responses are compared with simulation results using a rigid-body model. Deviation from the simulation is discussed and fed back to the servo design of the active controls.

Sections after 8.2 describe performance tests on the actively controlled suspension system. As discussed in **??**, the active control system has to accept three different control phases (the calm-down, the lock-acqusition phase and the observation phase). Section 8.2 forcuses on the calm-down phase and describes the performance of damping controls. Section **??** forcuses on the lock-acquisition phase, in which low RMS displacement and rotation angles of TM are required. In section **??**, the lock of the TM longitudinal displacement is demonstrated using photosensors as substitution for a laser interferometer. The noise couplings from the control system are discussed in terms of the impact on the detector sensitivity in the observation phase.

In section **??**, long-term tests of the active control system are performed. An automaton is constructed in the digital system so that the control loops switches between the three control phases automatically. The TM displacement is kept controlled for few days with the automaton operated. Section **??** describes summary of the performance tests and possible feedback to the actual design of the mechanical and servo system.

8.1 Mechanical response of suspension system

In this section, the mechanical responses of the type-B SAS prototype is investigated by using implemented sensors and actuators. Frequency response of the mechanical system affects the design of servo filters which are implemented in the following active control tests. The measured frequency responses are compared with simulation results and are fed back to the servo filter designs according to the deviation from the simulation.

8.1.1 Measurement setup

Frequency responses of the suspension system are measured in terms of rigid-body motions of the suspension bodies in the Euclid coordinate system. Virtual sensors and actuators, which measure and excite the rigid-body motions in certain DoFs, are constructed in the digital system with linear combination of real sensors and actuators. The measurement is done by injecting broadband gaussian noise from a virtual actuator in a certain DoF and checking the resulting displacements measured by virtual sensors. The noise injection point and measurement point in the digital system are indicated in the block diagram shown in Fig. 8.1. The frequency responses are calculated as $H(\omega) = \tilde{x}/\tilde{e}$.

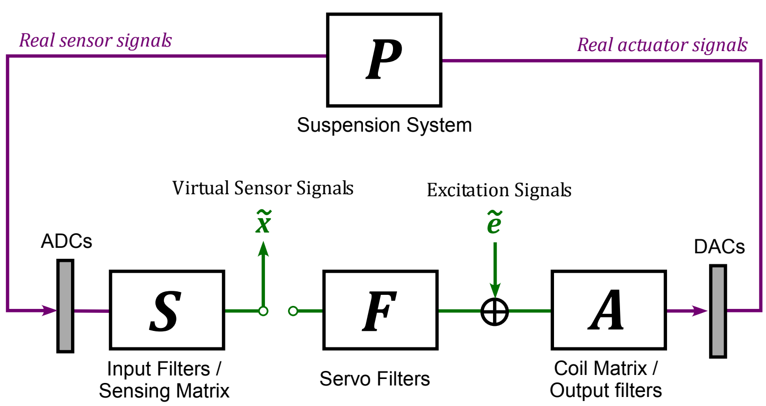

Figure 8.1: Signal flows in the transfer function measurement.

The virtual actuators to which the noise is injected are diagonalized beforehand. The actuator diagonalization about the IM and TM stage is conducted using the method described in section **??** with sinusoidal excitation at a frequency well below the resonant frequencies regarding the mass to be actuated. The diagonalization frequencies are set 20 mHz both for the actuators on IM and TM. On the other hand, we do not use the same diagonalization scheme for the actuators on F0. Due to large couplings between different DoFs, the frequency response to the virtual actuators diagonalzed with this scheme gets complicated, and that makes the SISO-type control quite difficult. Thence the coil matrix for the F0 actuators is roughly set from geometry, and then is normalized so that the amplitudes of diaognal transfer functions from the actuators to the sensor signals become 1 in DC.

Amplitude and spectrum of the excitation signal are tuned so that sufficient S/N is obtained in the whole interested frequency band but do not excite the mechanical resonances much, to let the sensors staying in the linear regime. Excitation amplitude is reduced around 1 Hz where many resonant frequencies of the suspension system exist and notch filters are introduced for some specific resonances. The left graph in figure 8.2 shows an example of spectra about the excitation in the TM longitudinal direction and displacements measured by OSEMs on TM. A notch filter is introduced to the excitation signal at 0.66 Hz, which is the resonant frequency of the pendulum mode about TM and RM. The right graph shows the coherence between the excitation signal and measured displacement signals. Good coherenence is observed between the excitation signal and longitdinal displacement in a wide frequency band, while poor coherence is observed around resonant frequencies because of disturbances from seismic vibration.

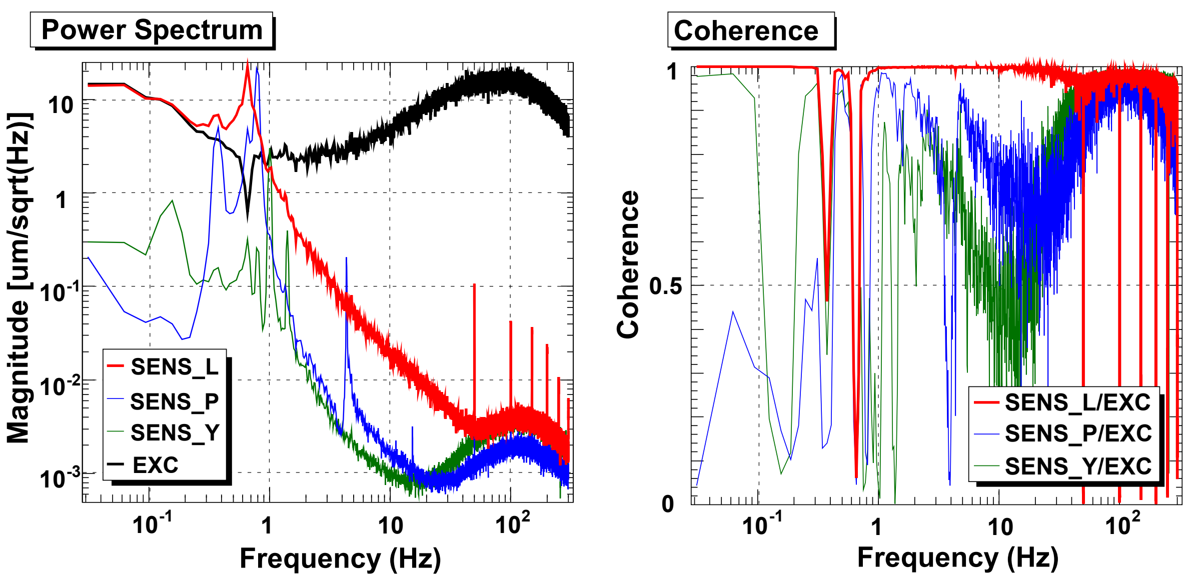

Figure 8.2: (*Left*) Spectra of the excitation signal in the TM longitudinal DoF and measured displacement signals. (*Right*) Coherence between the excitation signal and sensor signals.

8.1.2 Diagonal transfer functions

Figures 8.3-?? show bode plots of diagonal transfer functions (e.g. longitudinal → longitudinal) measured by implemented sensors and actuators, compared with predictions from a rigid-body model simulation. The measurements on the TM and IM stages are done by using OSEMs, while the measurements on the F0 stage and GAS filters are done by using LVDT-actuator units. The sensing signals from LVDTs on F0 are blended with geophone signals with blending filters described in section 8.3.

Measured transfer functions basically fit well with the prediction. This indicates that the suspension system has no critical troubles like mechanical contact or friction between suspension bodies. Nevertheless, several descrepancies are found between the measurement and simulation. The observed descrepancies and possible explanations are described below:

- Measured transfer functions deviate from the prediction above ∼30 Hz for the measurements with OSEMs and above ∼5 Hz for the measurement with LVDTs. The deviation is caused by electro-magnetic coupling between the actuation signal and sensing signals. The measurements with LVDTs suffer from larger couplings since the sensing coils are arranged coaxially with actuation coils and the signals couple directly through magnetic fields.

- Position of resonant peaks observed in the IM vertical, pitch and roll transfer functions deviate largely from the prediction. The simulation predicts a resonance at 4.9 Hz in the pitch transfer function, while measured resonant frequency is 4.3 Hz. Also the measured resonant frequencies found around 45 Hz in vertical, and 60 Hz in roll are lower than the prediction. These resonances corespond to the pitch, roll and vertical bounce modes about RM. A possible reason for the deviation is that hanging condition of RM is not good and one of the 4 wires suspending RM is not loaded. The floating wire doesn't contribute to the stiffness in pitch, roll and vertical motions of RM and the spring constant is reduced by 25%. Consequently the resonant frequencies of these mode are reduced by 13%, which is consistent with the observed deviation.

- The frequency responses at low frequencies in F0 transversal and yaw modes deviates largely from the prediction. The deviation can be explained by asumming asymmetry in the IP stiffness and large couplings between the transversal and yaw motions. Actually the resonant peak corresponding to the transversal mode of IP is also found in the transfer function in yaw, and vice versa. The simulated frequency response shown in figure 8.5 doesn't take into account the asymmetry.

- There are several resonant peaks observed at high frequencies but not predicted in the rigid-body model simulation. The peaks at 50 and 100 Hz observed in the TM longitudinal transfer function are due to ham noise in electronics. Resonances found around 70-80 Hz in IM roll and pitch trasnfer functions are caused by violin modes of the suspension wires for RM. Reosnant peaks above 20 Hz in F0 transfer functions are caused by the backaction in the outer frame.

8.1.3 Couplings with other DoFs

The measurement results described above only show the diagonal transfer functions, looking at the same DoFs as those of the excitation. Here the couplings between other DoFs are discussed.

Figure 8.7 shows the transfer functions from the TM longitudinal actuator to the TM-RM motions including other DoFs than longitudinal. Since the actuators are diagonalized

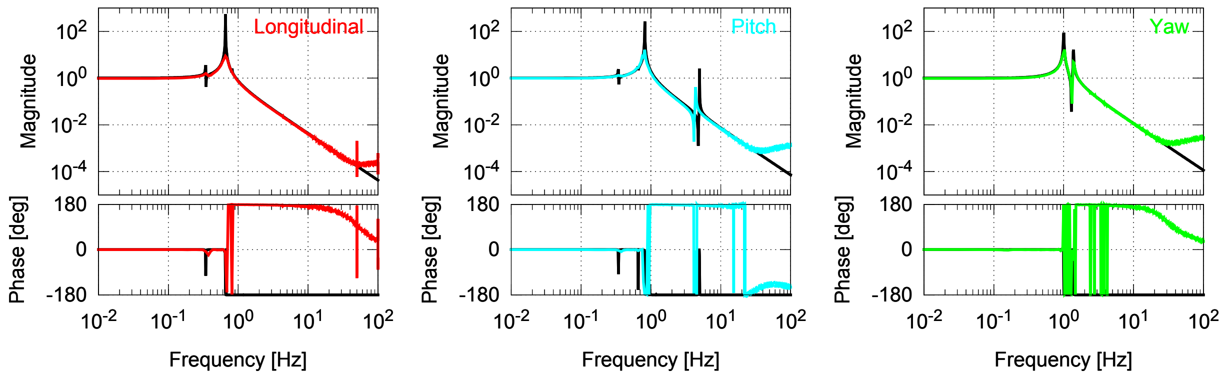

Figure 8.3: Comparison of diagonal transfer functions measured by TM-OSEMs (shown in colored lines) and prediction from the rigid-body model simulation (shown in black lines).

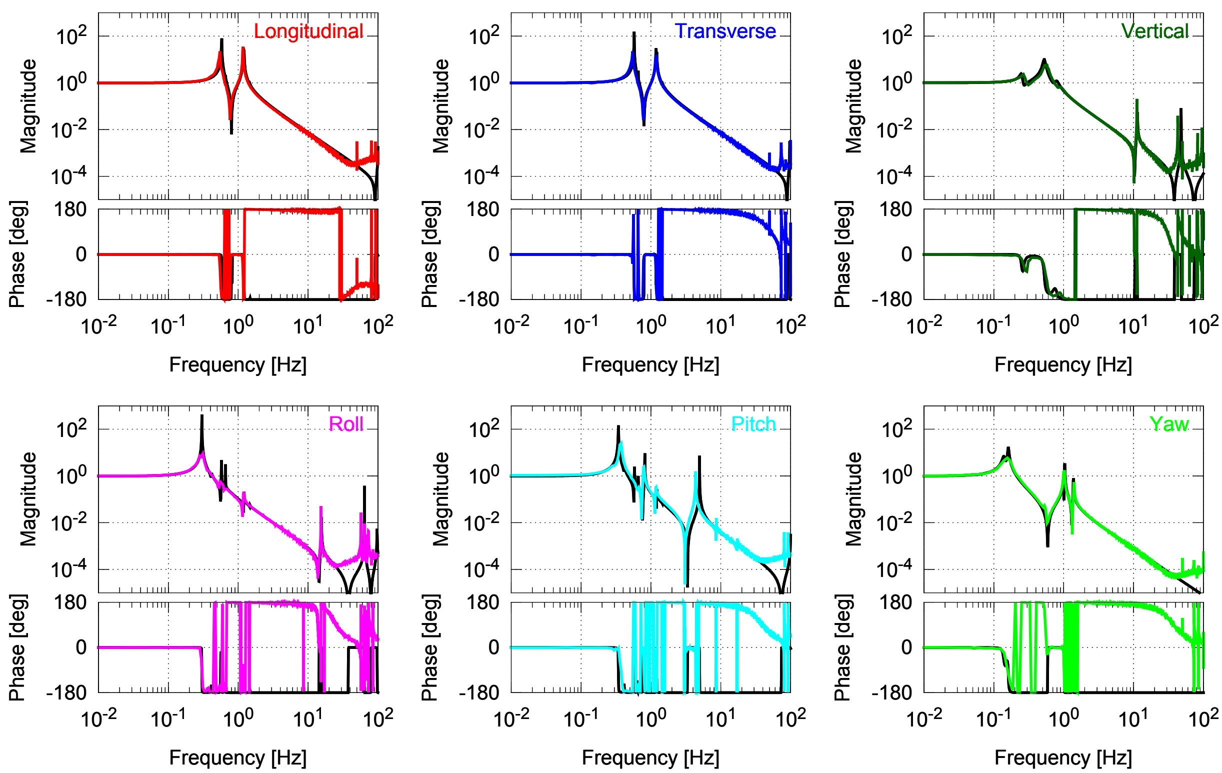

Figure 8.4: Comparison of diagonal transfer functions measured by IM-OSEMs (shown in colored lines) and prediction from the rigid-body model simulation (shown in black lines).

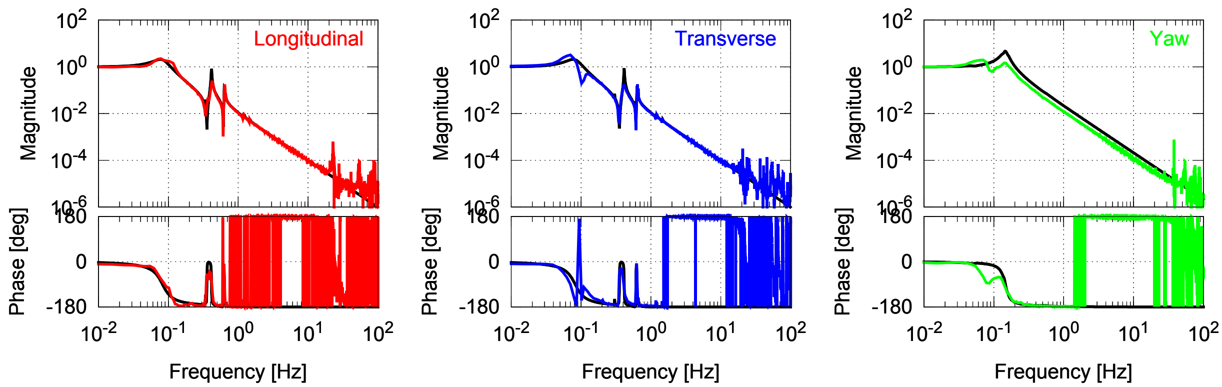

Figure 8.5: Comparison of diagonal transfer functions about F0 (shown in colored lines) and prediction from the rigid-body model simulation (shown in black lines).

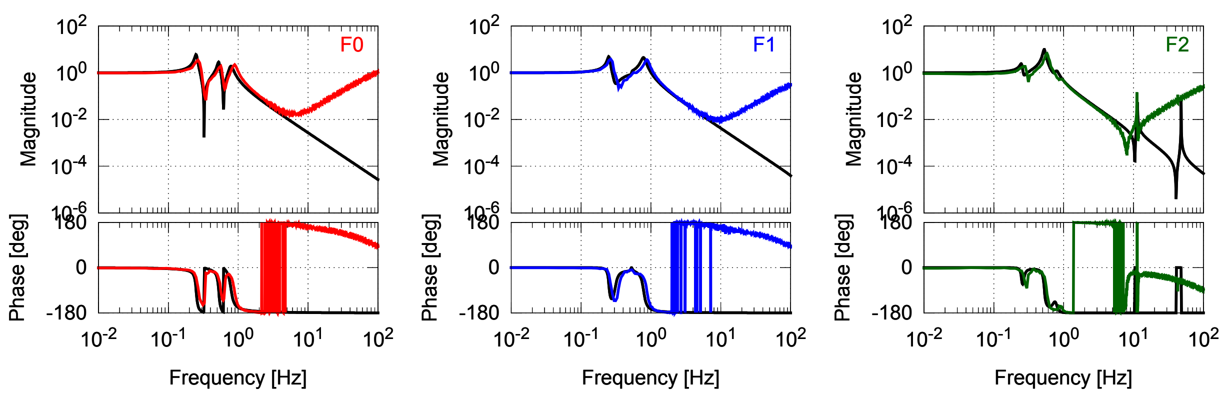

Figure 8.6: Comparison of transfer functions measured by LVDT-actuator units on GAS filters (shown in colored lines) and prediction from the rigid-body model simulation (shown in black lines).

at 20 mHz, amplitudes of the off-diagonal transfer functions are much lower than that of the diagonal one (few %) at low frequencies. On the other hand, the transfer functions at the frequencies higher than resonances show larger coupling (∼10% at 10 Hz).

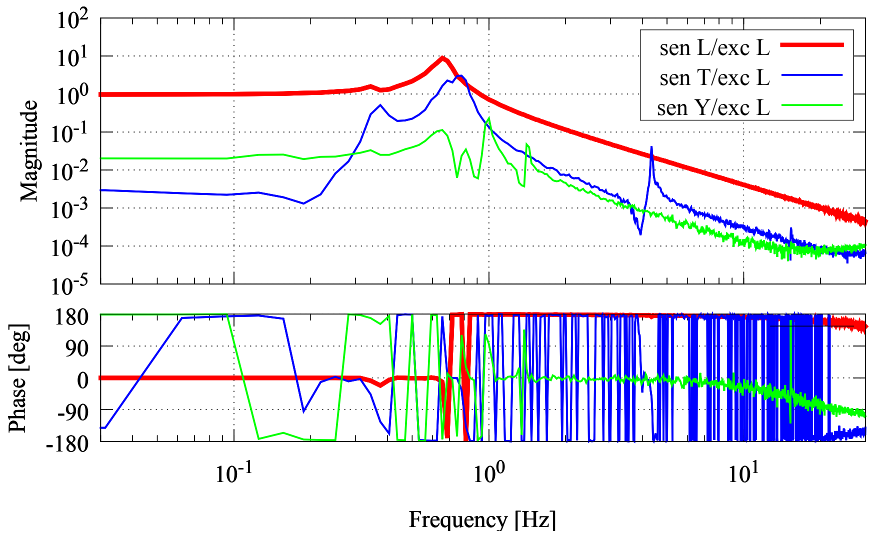

Figure 8.7: Measured transfer functions from the TM-RM longitudinal actuator to the displacements including the coupling with other DoFs.

The following tables show magnitude of coupling coefficients (amplitudes of transfer functions) at a low frequency (10 mHz) and a high frequency (10 Hz). The response about IM and TM actuators shows small coupling to other DoFs at the low frequency owing to the actuator diagonalization. In the meanwhile, the response of IM actuators shows large couplings at the high frequency. Especially couplings from rotational actuators (R, P and Y) to some DoFs are huge. The couplings to the longitudinal motions could be problematic since they can cause control noise coupling to the interferometer signals. The noise couplings to the TM longitudinal motion are discussed later. The couplings of F0 actuators are also huge at the low frequency, while they are not so large as to affect the control stability.

	sensor L		sensor P		sensor Y	
	10 mHz	10 Hz	10 mHz	10 Hz	10 mHz	10 Hz
actuator L	1		0.003	0.075	0.021	0.035
actuator P	0.005	0.099	1		0.001	0.013
actuator Y	0.005	0.007	0.002	0.011	1	

Table 8.1: Coupling conefficeints in the TM stage

	sensor L	sensor T	sensor V	sensor R	sensor P	sensor Y
actuator L	1	0.001	0.002	0.002	0.011	0.001
actuator T	0.000	1	0.000	0.001	0.002	0.010
actuator V	0.003	0.001	1	0.010	0.004	0.002
actuator R	0.001	0.001	0.001	1	0.002	0.002
actuator P	0.005	0.003	0.011	0.023	1	0.010
actuator Y	0.000	0.007	0.004	0.003	0.000	1

Table 8.2: Coupling conefficeints in the IM stage at 10 mHz

	sensor L	sensor T	sensor V	sensor R	sensor P	sensor Y
actuator L	1	0.001	0.007	0.011	0.001	0.027
actuator T	0.006	1	0.006	0.009	0.013	0.015
actuator V	0.027	0.003	1	0.032	0.018	0.011
actuator R	0.165	0.627	0.019	1	0.417	0.030
actuator P	0.267	0.008	0.025	0.017	1	0.023
actuator Y	0.113	0.622	0.035	0.018	0.034	1

Table 8.3: Coupling conefficeints in the IM stage at 10 Hz

	sensor L		sensor T		sensor Y	
	10 mHz	10 Hz	10 mHz	10 Hz	10 mHz	10 Hz
actuator L	1		0.874	0.012	0.389	0.010
actuator T	0.253	0.014	1		0.466	0.016
actuator Y	0.263	0.086	0.739	0.031	1	

Table 8.4: Coupling conefficeints in the F0 stage

8.1.4 Summary of this work

Frequency response of the suspension system is investigated by using implemented sensors and actautors. The measured freqency response shows similar tendency as predicted frequency response in the rigid-body model simulation, which proves that mechanical system is working almost as is designed. The differences between the model and actual system are discussed and we have the following findings:

- Electro-magnetic couplings of sensor signals with actuation signals change the shape of transfer functions in the high frequency regime.
- The resonant frequencies regarding the RM suspension deviate from simulated values, probably due to a floating wire in a bad hunging condition.
- Large couplings in transfer functios about F0 indicate asymmetry of the IP stiffness.
- Actuator diagonalzation works well for IM and TM actuators. However it does not reduce the couplings between different DoFs at high frequencies, which might cause large control noise coupling to the interferometer signals.

8.2 Damping control tests

Here active damping servos are switched on and the decay time reduction of mechanical resonances is performed. The servo filters are designed based on the frequency responses from actuators to sensors mentioned above. Since measured frequency responses deviate from simulated responses due to non-mechanical couplings at higher frequencies, one needs to reduce the control gains at these frequencies with low-pass filters in suitable cut-off frequencies. The decay time of mechanical resonances in the actively controlled system is investigated and compared with that in the passive system.

8.2.1 Servo design

Figure **??** shows a schematic diagram of the control loops implemented for the calm-down phase. Damping control loops are built in the TM, IM and F0 levels using OSEMs or LVDT-actuator units. Resonances about vertical GAS filter modes are damped by an LVDT-actuator unit in the top GAS filter (F0). DC servos are also bulit in the F0 and GAS control loops for suppressing drift of IP and GAS filters. The geophones and optical lever are not used in the calm-down phase. Since the control in the calm-down phase requires robustness rather than calmness, these sensitive sensors with small linear range are not suitable for this use.

Figures 8.9-8.12 show bode plots of designed servo filters. In order to obtain viscous damping forces, displacement signals obtained by OSEMs and LVDTs are converted to velocities with differentiation filters and sent to the actuators with appropriate gains.

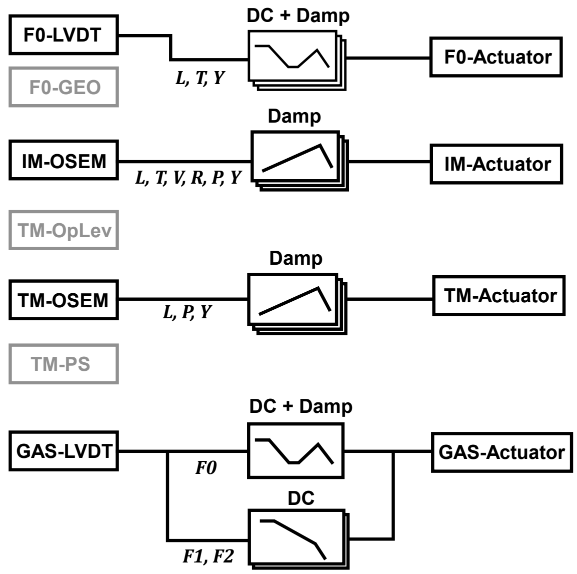

Figure 8.8: Schematic diagram of control loops for the type-B SAS prototype in the calm-down phase.

Thence the feedback filters have gain proportional to f around the frequencies of mechanical resonaces to be damped. The gains of damping controls are tuned to acquire optmial damping strength. A resonant gain introduced around 0.16 Hz to the IM yaw control is for intention of damping the torsion mode of the IM suspension wire efficiently. For the F0 and GAS controls, the control gains are boosted at low frequencies for drift compensation. DC control gains are set 1000 for the F0 control and 300 for the GAS controls with cutoff at 0.1 mHz.

The control gains at high frequencies are suppressed by applying low-pass filters with certain cut-off frequencies. The cut-off frequencies are set lower than the frequencies where the electro-magnetic couplings of sensors and actuators start dominant. The typical frequencies are 50 Hz for OSEMs and 5 Hz for LVDT-actuator units. The cut-off frequencies are set even lower in some DoFs to avoid exciting mechanical resonances around these frequencies.

8.2.2 Decay time measurement

In order to check if the mechanical resonances are properly damped by the active controls, mechanical resonances of the suspension system are surveyed and the decay time constants are measured in the passive system and the actively controlled system. Decay time constants of the mechanical resonances are obtained as follows. Firstly, a mechanical resonance is excited by sending sinusoidal wave with the resonant frequency to an appropriate virtual actuator. Then the excitation is switched off and a decay signal is

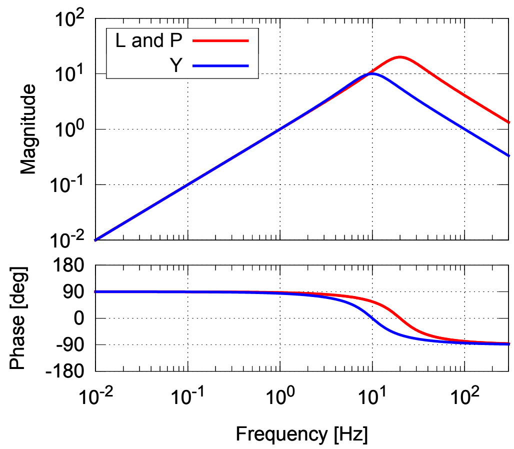

Figure 8.9: TM control servo filters.

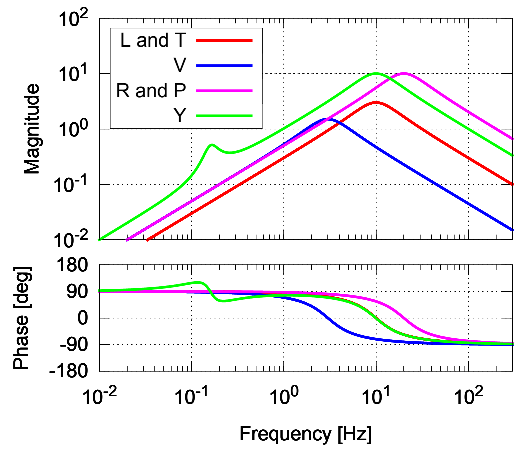

Figure 8.10: IM control servo filters.

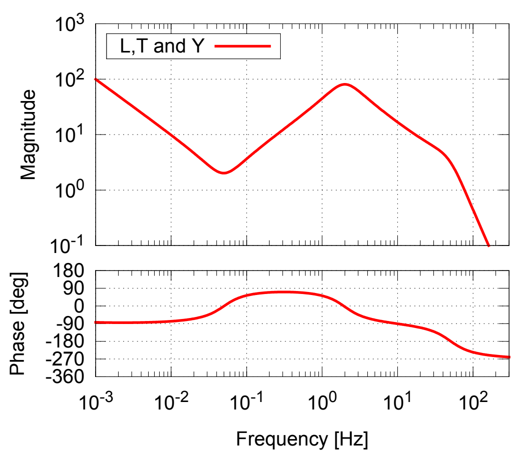

Figure 8.11: F0 control servo filters.

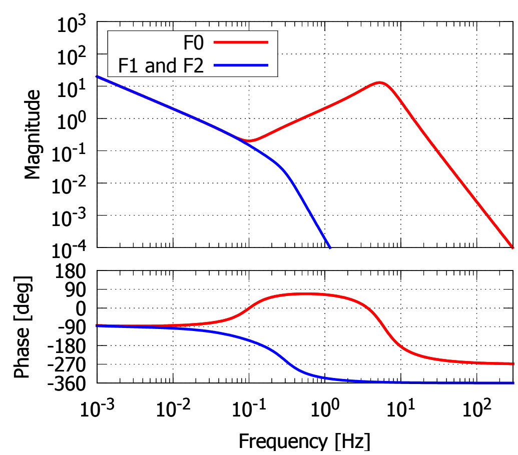

Figure 8.12: GAS control servo filters.

observed by implemented sensors. The decay signal is fit with an exponential decay sine wave:

$$f(t) = A \exp(-t/\tau) \sin(2\pi f_0 t + \varphi) + x_0. \tag{8.1}$$

The time constant τ indicates the $1/e$ decay time of the mechanical resonance. Sometimes it is difficult to excite only one resonant mode and one obtains a superposition of two sine waves. This can happen when there exist mechanical resonaces with close eigen frequencies. In such a case, the decay signals are fit by sum of two decay sine waves.

Figure **??** shows an example of decay signals, regarding the pendulum mode of IM (mode #17). The left graph shows the measured decay signal without damping controls and the right graph shows that with damping controls. The signals are obtained by the readout of longitudinal displacement using IM OSEMs. Fittings are performed using signals of the time between 0 and 15 [sec]. The oscillation decays faster when the damping controls are applied, and the $1/e$ decay time is shorten by a factor more than 10 by the controls.

Note that the measured signal with damping controls deviates from the fitting curve when the oscillation amplitude gets small. The decay time increases when the oscillation amplitude falls below a certain value ($\sim 10\ \mu$m for the mode). This indicates that damping forces are not applied well for small amplitude oscillations. Explanations on this phenomenon are described later.

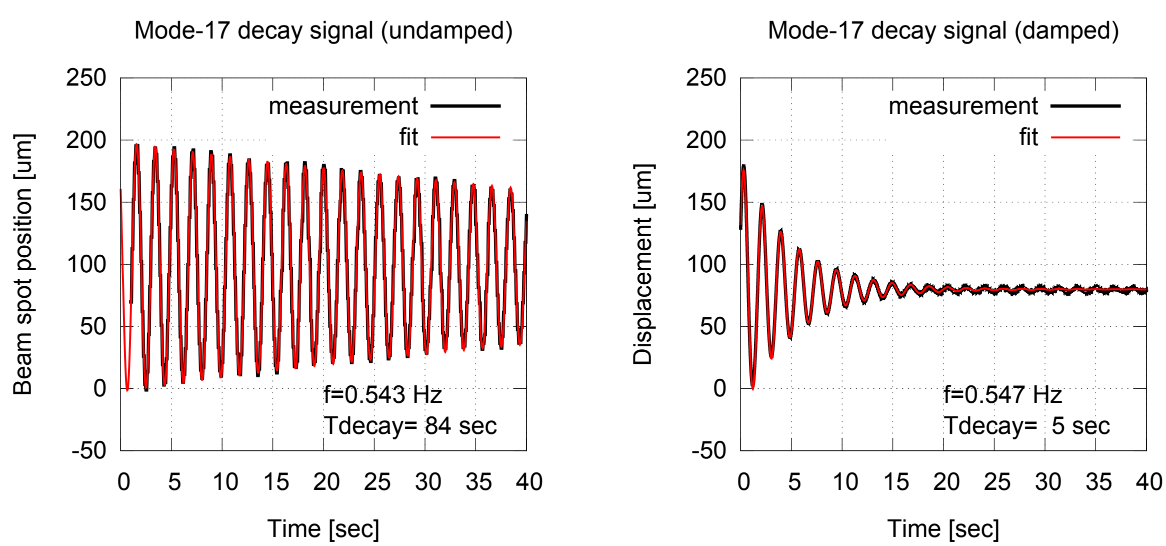

Figure 8.13: Decay signals about resonant mode #17 with and without damping control. The signals are obtained by the longitudinal displacement readout from IM OSEMs.

Table A.1 shows a list of mechanical resonances of the suspension system predicted in a rigid-body model simulation. It only shows the mechanical reosnances with eigen frequencies less than 20 Hz.

No.	Frequency [Hz]	Mode Shape	Note
#1	0.0505	YF1, YF2, YIR, YIM, YRM, YTM	wire torsion
#2	0.0794	LF0, LMD, LF1, LF2, LIR, LIM, LRM, LTM	IP translation
#3	0.0794	TF0, TMD, TF1, TF2, TIR, TIM, TRM, TTM	IP translation
#4	0.1232	-YF0, YIM, YRM, YTM	IP rotation
#5	0.1390	-YF1, YIM, YRM, YTM	wire torsion
#6	0.1616	-YF2, -YIR, YIM, YRM, YTM	wire torsion
#7	0.2494	VF2, VIR, VIM, VRM, VTM	GAS filter
#8	0.3021	RIM, RRM, RTM	IM roll
#9	0.3418	PIM, PRM, PTM	IM pitch
#10	0.4094	TIM, TRM, TTM, RTM	main pendulum
#11	0.4196	LIM, LRM, LTM, PTM	main pendulum
#12	0.5247	-VF1, -VF2, -VIR, VIM, VRM, VTM	GAS filter
#13	0.5468	TMD	MD pendulum
#14	0.5470	LMD	MD pendulum
#15	0.5502	YMD	MD yaw
#16	0.5740	RF2, RIR	F2 roll
#17	0.5787	PF2, PIR	F2 pitch
#18	0.5889	RF1	F1 roll
#19	0.6331	-PF1, LTM, -PTM	main pendulum
#20	0.6485	RF1, TTM, RTM	main pendulum
#21	0.6571	-LRM, LTM, -PTM	TM-RM pendulum
#22	0.6580	TRM, TTM, RTM	TM-RM pendulum
#23	0.6863	PF1	F1 pitch
#24	0.7923	VF1, -VF2, -VIR	GAS filter
#25	0.8162	PTM	TM pitch
#26	1.0009	-YIM, -YRM, YTM	TM yaw
#27	1.0325	YIR	IR yaw
#28	1.1844	TIM, -TTM, -TRM	IM pendulum
#29	1.1851	LIM, -LIM, -LRM	IM pendulum
#30	1.2101	RF2, -TIR, RIR	F2 roll
#31	1.2134	PF2, LIR, PIR	F2 pitch
#32	1.3798	-YIM, YRM, YTM	RM yaw
#33	1.4738	TIR	IR pendulum
#34	1.4759	LIR	IR pendulum
#35	4.8559	-PIM, PRM	RM pitch
#36	11.320	VTM	TM vertical
#37	15.528	RTM	TM roll

Table 8.5: Eigen mode list predicted in a rigid-body model simulation.

Table 8.6 and 8.7 shows measured resonant frequencies and decay time of resonant modes. Figure ?? show plots of the decay time versus resonant freuquencies measured in the prototype. Decay time constants of most mehcanical resonances are suppressed lower than 1 min. with damping controls applied. There is one resonant mode whose decay time constant exceeds 1 min. and the mode is regarding with tranversal motions of TM and RM. The mode shape is shown in figure ??. Since there is no device implemented for sensing or actuating their transversal motions, it is not able to damp this mode efficiently. However, the TM transversal motion do not interfer the interferometer operation unless the amplitude exceeds ∼1 mm, which is the requirement on the beam spot fluctuation on mirrors of the interferometer. Since the amplitude of this oscillation mode does not exceed 1 mm due to mechanical constains between TM and RM, there is no problem of having large decay time about this mode.

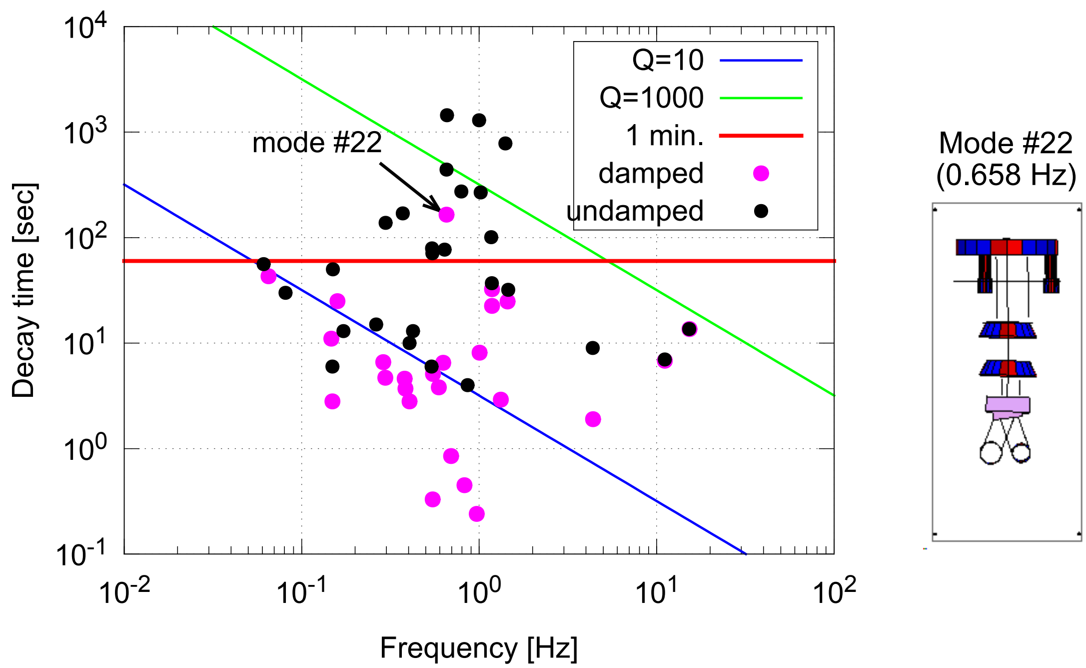

Figure 8.14: Decay time versus resonant frequency plot.

8.2.3 Correction signals

A feedback signal sent to an IM-OSEM actuator during the damping control is shown in figure ??. An impulsive force is applied to the actuator to excite mechanical resonances. The feedback signal decays as the oscillation amplitude decays, and the amplitude goes under 1 digital count at a certain point. The feedback signal is digitized when digital signals are converted analog signals, so the oscillation under 1 digital count is omitted

	Frequency [Hz]					
No.	measured	simulated	difference [%]	τ [sec]	Q factor	exc. point
#1	0.061	0.0505	20.7	56	11	YF0
#2/#3	0.081	0.0794	2.5	30	8	LF0
#4	0.149	0.1232	20.9	6	3	YF0
#5	0.150	0.1390	7.7	50	24	YF0
#6	0.172	0.1616	6.2	13	7	YF0
#7	0.263	0.2494	5.6	15	13	VF0
#8	0.297	0.3021	1.9	138	129	RIM
#9	0.371	0.3418	8.4	170	198	PIM
#10	0.405	0.4094	1.0	10	12	TF0
#11	0.424	0.4196	1.0	13	17	LF0
#12	0.539	0.5247	2.7	6	9	VF0
#13	-	0.5468	-	-	-	-
#14	-	0.5470	-	-	-	-
#15	-	0.5502	-	-	-	-
#16	0.545	0.5740	0.6	71	122	TIM
#17	0.543	0.5787	0.6	79	135	LIM
#18	-	0.5889	-	-	-	-
#19/#20	0.639	0.6331	1.1	77	154	LF0
#21	0.659	0.6571	0.7	1448	2996	LTM
#22	0.655	0.6580	0.4	442	909	TF0
#23	-	0.6863	-	-	-	-
#24	0.861	0.7923	8.7	4	10	VF0
#25	0.793	0.8162	2.9	274	683	PTM
#26	1.000	1.0009	0.1	1295	4069	YTM
#27	1.020	1.0325	1.2	268	857	YIM
#28/#30	1.169	1.2101	3.4	101	371	TIM
#29/#31	1.178	1.2134	2.9	37	135	LIM
#32	1.406	1.3798	1.9	782	3456	YTM
#33/#34	1.456	1.4728	1.0	32	143	TF0
#35	4.361	4.8559	10.2	9	119	PTM
#36	11.11	11.320	1.9	7	237	VIM
#37	15.25	15.528	1.8	5	235	RIM

Table 8.6: Measured resonant frequencies and decay time without control.

No.	Frequency [Hz] damped	undamped	difference [%]	τ [sec]	Q factor	exc. point
#1	0.065	0.061	5.6	43	8.6	YF0
#2/#3	0.149	0.081	45.6	2.8	1.3	LF0
#4/#5	0.147	0.15	1.9	11	5.2	YF0
#6	0.159	0.172	8.4	25	13	YF0
#7	0.288	0.263	8.5	6.6	6.6	VF0
#8	0.296	0.297	0.3	4.7	4.4	RIM
#9	0.380	0.371	0.3	4.6	5.6	PIM
#10	0.384	0.405	5.2	3.7	4.4	TF0
#11	0.405	0.424	4.5	2.8	3.5	LF0
#12	0.592	0.539	8.9	3.8	7.0	VF0
#13	-	-	-	-	-	-
#14	-	-	-	-	-	-
#15	-	-	-	-	-	-
#16	0.547	0.545	0.7	0.33	0.6	TIM
#17	0.549	0.543	0.7	5.1	8.7	LIM
#18	-	-	-	-	-	-
#19/#20	0.627	0.639	1.8	6.5	13.0	LF0
#21	0.694	0.659	5.0	0.85	1.9	LTM
#22	0.655	0.655	0.0	165	339	TF0
#23	-	-	-	-	-	-
#24	-	0.861	-	-	-	-
#25	0.826	0.793	4.0	0.45	1.2	PTM
#26	0.969	1.000	3.2	0.24	0.7	YTM
#27	1.006	1.020	1.4	8.1	26	YIM
#28/#30	1.180	1.176	0.3	32.5	120	TF0
#29/#31	1.180	1.176	0.3	22.5	84	LF0
#32	1.324	1.406	6.2	2.91	12	YTM
#33/#34	1.446	1.445	0.1	24.8	113	TF0
#35	4.383	4.361	0.5	1.9	26	PTM
#36	11.11	11.11	0.0	6.8	237	VIM
#37	15.30	15.25	0.3	13.6	654	RIM

Table 8.7: Measured resonant frequencies and decay time with control.

and not sent to the actuator. This means that the damping control doesn't work under a certain oscillation amplitude. The typical oscillation amplitudes to acquire feedback signals of 1 digital count are $\sim 0.1\ \mu$m for the F0 stage, $\sim 10\ \mu$m for the IM and TM stages.

Figure **??** shows spectra of measured feedback signals when the prototype system is in equillibrium. RMS amplitudes are much lower than 1 digital count and thus feedback signals are not sent to actuators correctly when the system calms down. Because of the digitization problem, RMS of the oscillation amplitude in a calm-down state is not improved by the active controls. In order to have feedback controls even when the system calms down, the actuation efficiency of the coil driver should be reduced.

8.2.4 Summary of this work

8.3 Low-RMS controls

8.3.1 Inverpendulum Controls

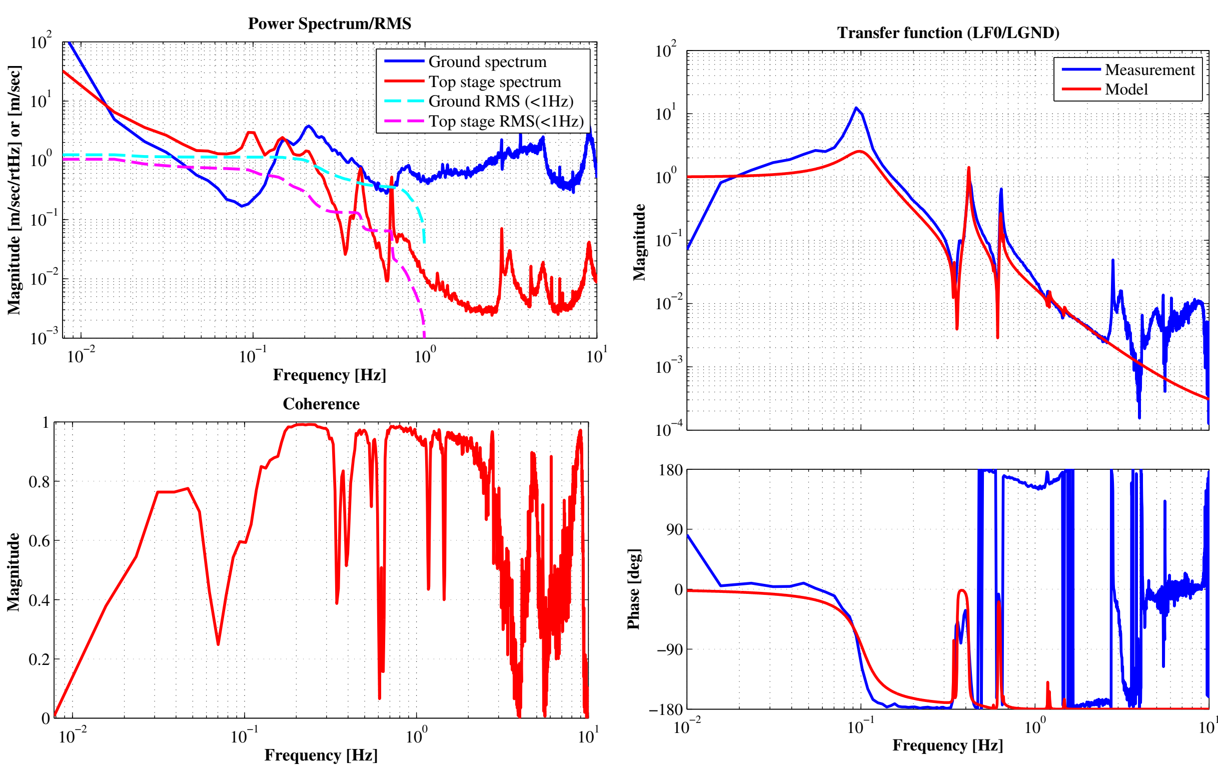

Figure 8.15: IP transfer function measurement without control

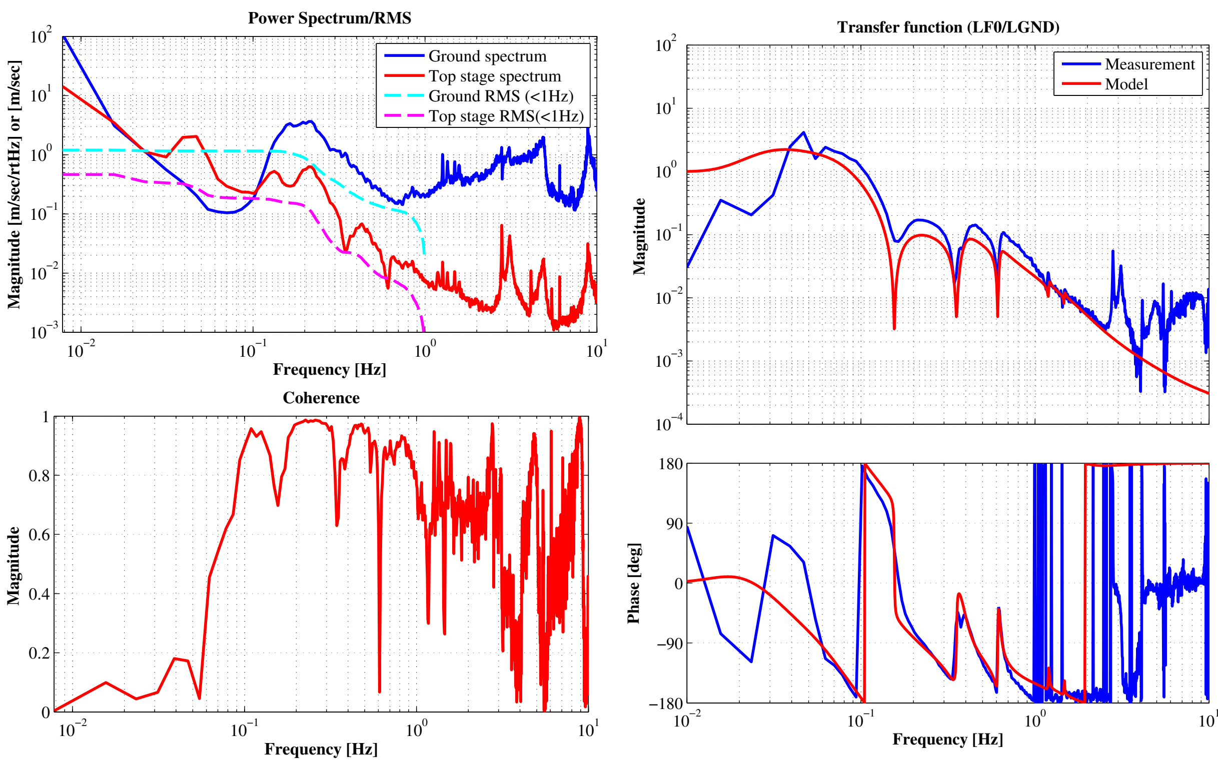

Figure 8.16: IP transfer function measurement with control

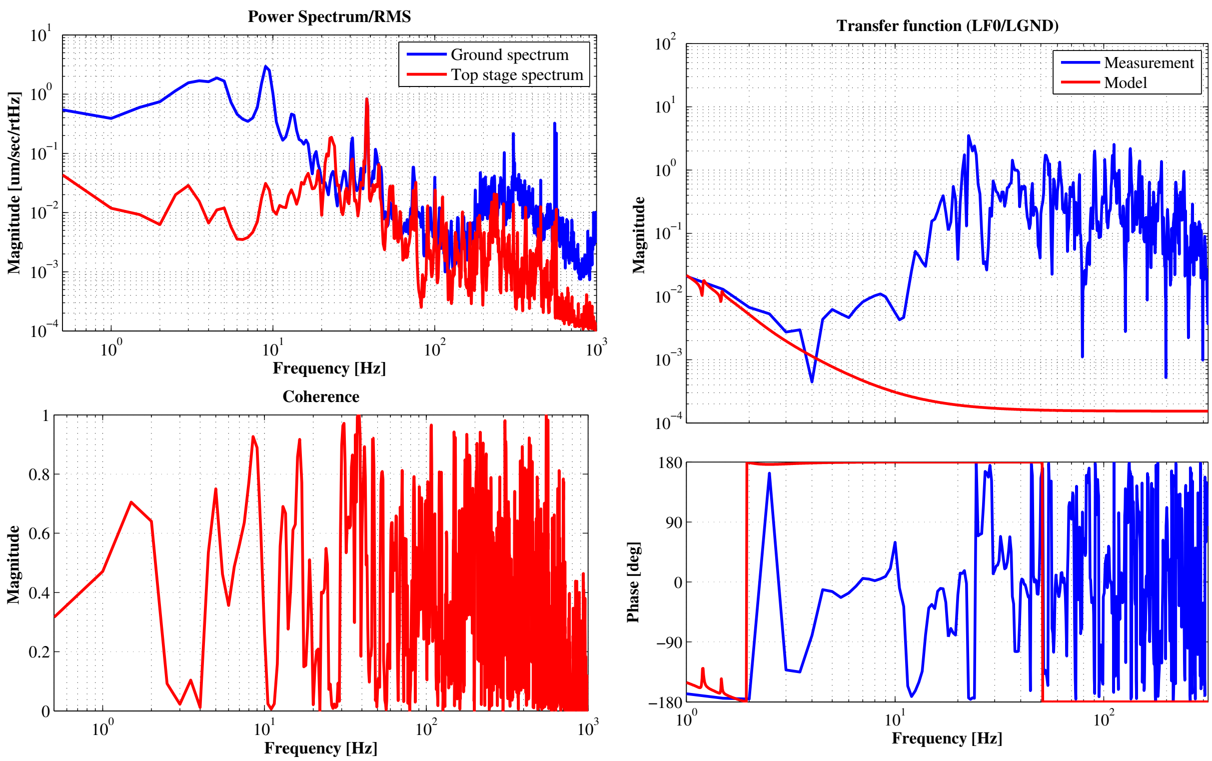

Figure 8.17: IP transfer function measurement high frequency

8.3.2 Vibration transferred to the test mass

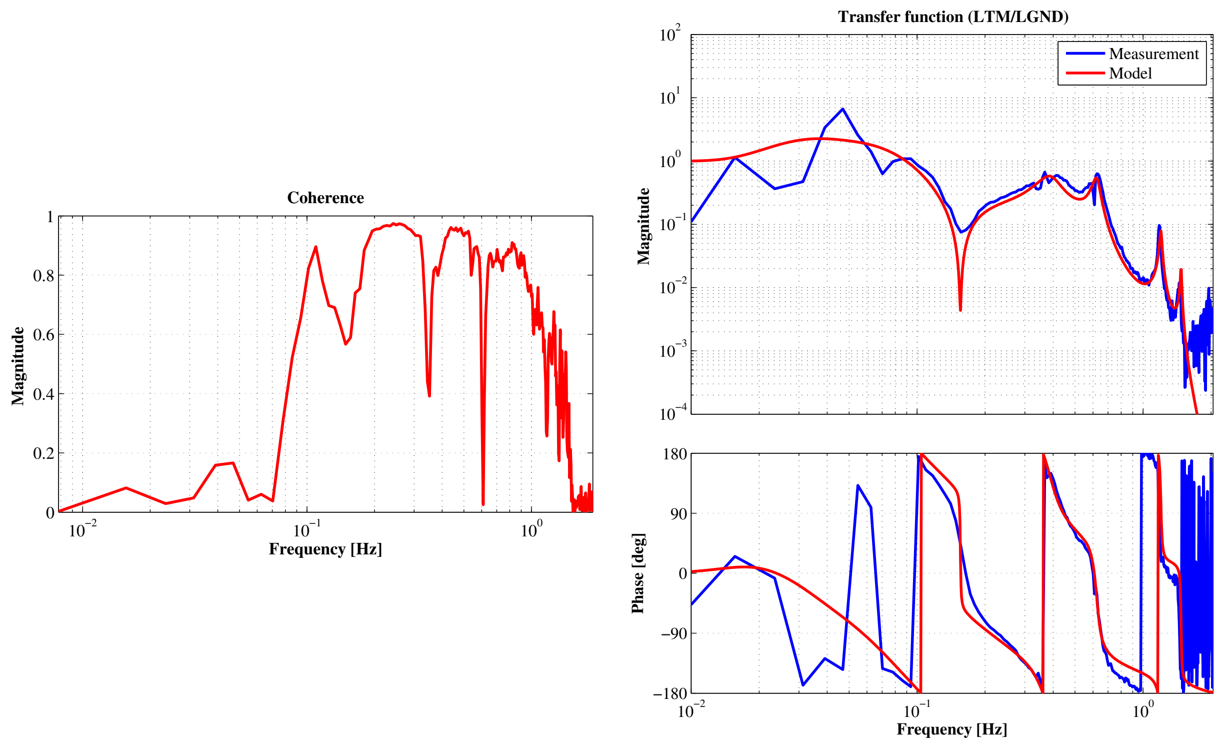

Figure 8.18: Transfer function from ground to TM.

8.4 Control using optical lever

We introduce angular control of the TM using optical lever signals fed back to the actuators on IM.

8.4.1 Transfer functions from actuators to optical lever signals

8.4.2 Control servos

8.4.3 Performance

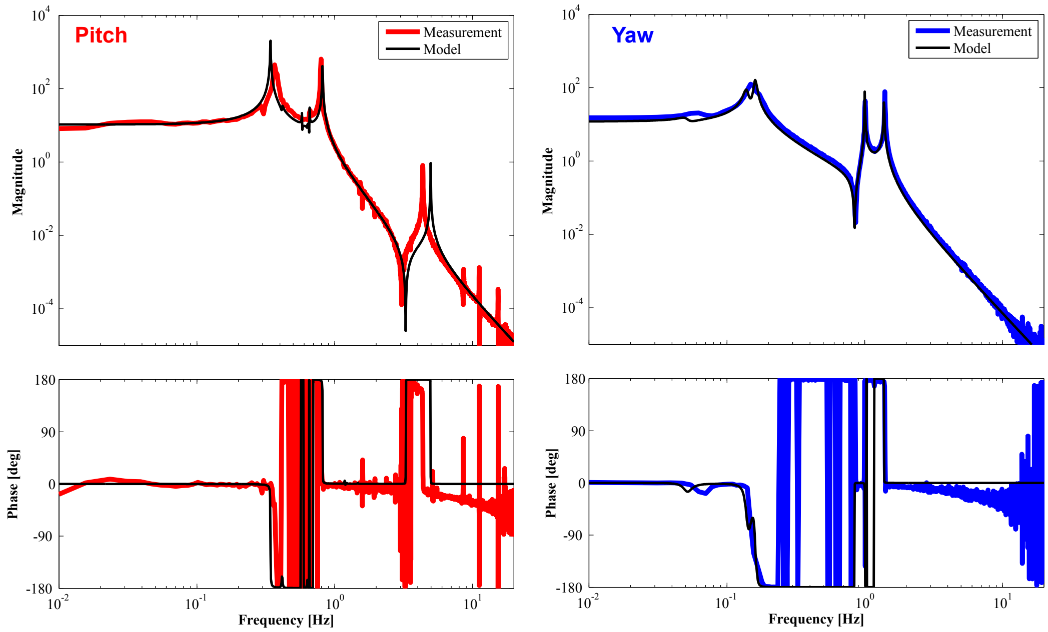

Figure 8.19: Transfer function from actuators to optical levers

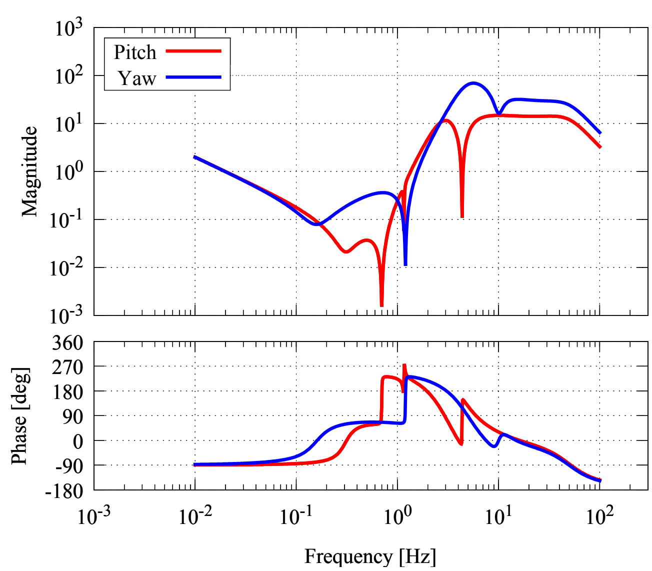

Figure 8.20: Servo filter design.

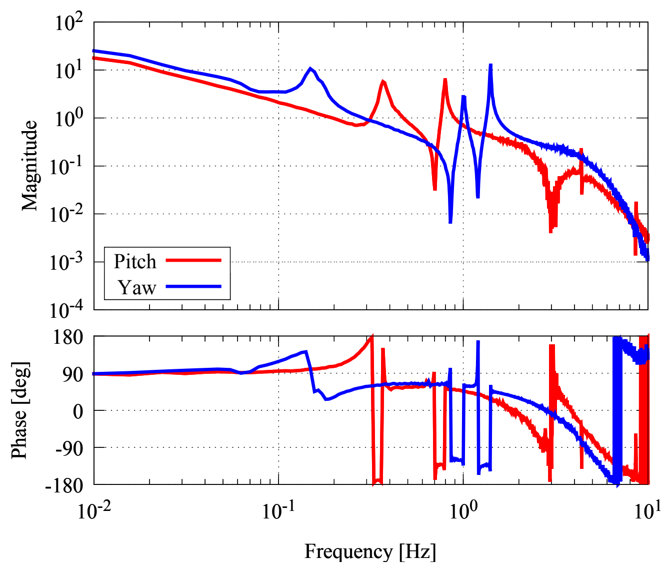

Figure 8.21: Open loop transfer functions.

Chapter 9

Design study on KAGRA type-A SAS

9.1 Theory and background

Summary and futre works

Chapter 10

Rigid-body model of type-B SAS prototype

Appendix A

A.1 Overview

A rigid-body model of the type-B SAS prototype is constructed in order to predict the frequency responses and the eigen modes. Here parameters for the modeling are summarized and predicted eigen modes are illustrated.

A.2 Parameters

A.2.1 Rigid bodies

Title	Symbol	Unit	F0	MD	F1	F2	IR	IM	RM	TM
Mass	M	kg	474	50	50	50	50	50	50	50
Moment of Inertia	I_{Roll}	kgm^2	120	50	50	50	50	50	50	50
	I_{Pitch}		120	50	50	50	50	50	50	50
	I_{Roll}		120	50	50	50	50	50	50	50

Table A.1: Eigen mode list predicted in a rigid-body model simulation.

Bibliography

[1] A. Einstein, *Ann. der Phys.*, **354** (7), 769–822, (1916).

[2] M. Maggiore. "Gravitational Waves: Theory and Experiments". Oxford University Press, (2008).

[3] T. Nakamura, N. Mio, and M. Ohashi. "Detecting gravitational waves". Kyoto University Press, (1998). (in Japanese).

[4] C. Cutler and K. Thorne, *arXiv*, **0204090 [gr-qc]**, (2002).

[5] K. Oohara and T. Nakamura, *Prog. Theor. Phys.*, **82** (3), 535–554, (1989).

[6] C. D. Ott, *Class. Quant. Grav.*, **26**, 063001, (2009).

[7] T. Damour and A. Vilenkin, *Phys. Rev. D*, **71**, 063510, (2005).

[8] The LIGO Scientific Collaboration and The Virgo Collaboration, *Nature*, **460**, 990–994, (2009).

[9] J. Weber, *Phys. Rev. Lett.*, **22**, 1320–1324, (1969).

[10] P. Astone et al., *Phys. Rev. D*, **82**, 022003, (2010).

[11] K. Kawabe, *PhD thesis*, University of Tokyo, (1998).

[12] B. Bochner, *Gen. Relativ. Gravit.*, **35** (6), 1029–1055, (2003).

[13] A. Buonanno and Y. Chen, *Phys. Rev. D*, **64**, 042006, (2001).

[14] M. Ando, *PhD thesis*, University of Tokyo, (1998).

[15] B. J. Meers, *Phys. Rev. D*, **38**, 2317, (1988).

[16] J. Mizuno, *PhD thesis*, Universitat Hannover, (1995).

[17] M. G. Beker, *PhD thesis*, Vrije Universiteit, (2013).

[18] P. R. Saulson, *Phys. Rev. D*, **42** (8), 2437–2445, (1990).

[19] W. J. Startin et al., *Rev. Sci. Instrum.*, **69** (10), 3681–3689, (1998).

[20] A. V. Cumming et al., *Class. Quant. Grav.*, **29**, 035003, (2012).

[21] S. Rowan et al., *Phys. Lett. A*, **265**, 40309, (2000).

[22] T. Tomaru et al., *Phys. Lett. A*, **301**, 215–219, (2002).

[23] H. J. Kimble et al., *Phys. Rev. D*, **65**, 022002, (2001).

[24] K. Arai et al., *Class. Quant. Grav.*, **26**, 204020, (2009).

[25] H. Grote (for the LIGO Scientific Collaboration), *Class. Quant. Grav.*, **27**, 084003, (2010).

[26] D. Sigg (for the LIGO Science Collaboration), *Class. Quant. Grav.*, **25**, 114041, (2008).

[27] T. Accadia et al., *Class. Quant. Grav.*, **28**, 114002, (2011).

[28] S. Fairhurst et al., *Gen. Relativ. Gravit.*, **43**, 387–407, (2011).

[29] K. Kuroda and LCGT collaboration, *Int. J. Mod. Phys. D*, **20** (10), 1755–1770, (2011).

[30] M. Punturo, *Class. Quant. Grav.*, **27**, 194002, (2010).

[31] Y. Aso et al., *Phys. Rev. D*, **88**, 043007, (2013).

[32] K. Somiya, *Class. Quant. Grav.*, **29**, 124007, (2012).

[33] S. Hild, *Class. Quant. Grav.*, **29**, 124006, (2012).

[34] P. Canizares et al., *Phys. Rev. Lett.*, **114**, 071104, (2015).

[35] P. Amaro-Seoane and L. Santamaria, *Astrophys. J.*, **722**, 1197–1206, (2010).

[36] T. Takiwaki and K. Kotake, *Astrophys. J.*, **743** (1), 30, (2011).

[37] K. Kotake et al., *Astrophys. J. Lett.*, **697** (2), 133–136, (2009).

[38] J. Abadie et al., *Astrophys. J.*, **722**, 1504–1513, (2010).

[39] J. Peterson, *Open File Report*, pages 93–322, (1993).

[40] P. Shearer. "Introduction to Seismology Second Edition". Cambridge Univirsity Press, (2009).

[41] "LCGT Design Document Ver. 3.0". (in Japanese, 2009) available from http://gwwiki.icrr.u-tokyo.ac.jp/JGWwiki/LCGT.

[42] H. A. Sodano et al., *J. Vib. Acoust.*, **128**, 294–302, (2006).

[43] T. Nishi, *Master's thesis*, University of Tokyo, (2003). (in Japanese).

[44] F. Matichard et al., *arXiv*, page 1502.06300, (2015).

[45] J. Giaime et al., *Rev. Sci. Instrum.*, **67** (1), 208–214, (1996).

[46] R. Takahashi et al., *Rev. Sci. Instrum.*, **73** (6), 2428–2433, (2002).

[47] G. Ballarding et al., *Rev. Sci. Instrum.*, **72** (9), 3635–3642, (2001).

[48] M. Beccaria et al., *Nucl. Instrum. Methods A*, **394**, 397–408, (1997).

[49] F. Acernese et al., *Astrop. Phys.*, **93**, 182–189, (2010).

[50] A. Takamori, *PhD thesis*, University of Tokyo, (2002).

[51] A. Takamori et al., *Nucl. Instrum. Methods A*, **582**, 683–692, (2007).

[52] G. Losurdo et al., *Rev. Sci. Instrum.*, **70** (5), 2507–2515, (1999).

[53] A. Stochino et al., *Nucl. Instrum. Methods A*, **598**, 737–759, (2009).

[54] G. Cella et al., *Nucl. Instrum. Methods A*, **540**, 502–519, (2005).

[55] R. DeSalvo et al., *Nucl. Instrum. Methods A*, **538**, 526–537, (2005).

[56] R. DeSalvo et al., *Eur. Phys. J. Plus*, **126**, 75, (2011).

[57] A. Stochino et al., *Nucl. Instrum. Methods A*, **580**, 1559–1564, (2007).

[58] The Virgo Collaboration. "Advanced Virgo technical design report". Chapter 12, VIR-0128A-12 URL: https://tds.ego-gw.it/ql/?c=8940, (2012).

[59] M. G. Beker et al., *Physics Procedia*, **37**, 1389–1397, (2012). Proceedings of the 2nd International Conference on Technology and Instrumentation in Particle Physics (TIPP 2011).

[60] M. Lobue et al., *J. Magn. Magn. Mater.*, **290**, 1184–1187, (2005).

[61] Y. Arase et al., *Journal of Physics: Conference Series*, **122**, 012027, (2008).

[62] Y. Aso et al., *Class. Quant. Grav.*, **29**, 124008, (2012).

[63] KAGRA Main Interferometer Working Group, *KAGRA Internal Document*, **JGW-T1200913-v6**, (2014).

[64] K. Agatsuma et al., *Class. Quant. Grav.*, **27**, 084022, (2010).

[65] A. Bertolini et al., *Nucl. Instrum. Methods A*, **556**, 616–623, (2006).

[66] H. Tariq et al., *Nucl. Instrum. Methods A*, **489**, 570–576, (2002).

[67] C. Wange et al., *Nucl. Instrum. Methods A*, **489**, 563–569, (2002).

[68] K. Agatsuma et al., *Journal of Physics: Conference Series*, **122**, 012013, (2008).

[69] G. Losurdo et al., *Rev. Sci. Instrum.*, **72** (9), 3653–3661, (2001).

[70] F. Cordero et al., *J. Alloys Compd.*, **310**, 400–404, (2000).

[71] M. Beccaria et al., *Nucl. Instrum. Methods A*, **404**, 455–469, (1998).

[72] A. Bernardini et al., *Rev. Sci. Instrum.*, **70** (8), 3463–3472, (1999).

[73] A. Takamori et al., *Class. Quant. Grav.*, **19**, 1615–1621, (2002).

[74] S. Aston, *LIGO Internal Document*, **T050111-04-K**, (2009).

[75] *KAGRA Internal Document*, **JGW-T1201255-v1**.